ABSTRACT

ARUNKUMAR, NITHYA. Designer Optical Control of Two-body Interactions in Ultracold Gases. (Under the direction of John Thomas.)

Optical control of interactions in ultracold gases can achieve new quantum phases, model exotic condensed matter systems, and even emulate the physics of black holes. However, optical techniques to control interactions have suffered from atom loss due to spontaneous scattering and are therefore severely restricted in their applicability. This thesis reports on experiments that demonstrate optical control of two-body scattering in ultracold ^{6}Li atoms using a new two-optical field method, where atom loss is suppressed by destructive quantum interference. Interactions are measured by employing radio-frequency spectroscopy. The experiments illustrate that our two-field optical method achieves the same level of tunability as the conventional method of magnetically tuning two-body interactions, potentially creating new fields of research. The two-body scattering length is controlled by tuning the laser frequency by only a few MHz, thereby not altering the intensity-dependent potential experienced by the atoms. Exploiting the tunability of interactions achieved using the two-field optical technique, this thesis also reports on experiments to demonstrate “designer" spatial control of interactions in an ultracold gas. Interaction profiles are imprinted on the atom cloud and controlled by tuning the frequency of the lasers. Furthermore, the two-field method is used as an optical vernier to investigate and study the momentum dependence of narrow Feshbach resonances with high precision. All the experimental data presented in this thesis are in excellent agreement with the theoretical model, which includes the momentum dependence of the two-body interactions and the spatial variation of the atom density.

Designer Optical Control of Two-body Interactions in Ultracold Gases

by
Nithya Arunkumar

A dissertation submitted to the Graduate Faculty of
North Carolina State University
in partial fulfillment of the
requirements for the Degree of
Doctor of Philosophy

Physics

Raleigh, North Carolina

2018

APPROVED BY:

Paul Huffman	Dean Lee
Gavin Conant	John Thomas Chair of Advisory Committee

DEDICATION

To Arun.

BIOGRAPHY

Nithya Arunkumar was born in Chennai, India on July 17, 1984. She received her undergraduate degree in physics from Madras University, India in 2006. She holds a Masters degree in physics from the University of Massachusetts Lowell, specializing in the study of terahertz waveguides for biomedical applications. She started her Ph.D. degree in 2011 under the supervision of Dr. John Thomas. Her Ph.D. research is focused on using quantum optics techniques to create high-resolution spatial control of interactions in ultracold atoms.

ACKNOWLEDGEMENTS

I would like to thank my advisor Dr. John Thomas for all his help and support during my Ph.D. I am very grateful to him for the trust he had in me to do such a complicated experiment. During the last 7 years, he created a laid back work atmosphere that fosters independent creativity.

I would like to express my very great appreciation to James Joseph for teaching me the most basic and fundamental skills in the cold atom experiments when I inherited the lab from Ethan Elliot after his graduation.

I would like to offer my special thanks to Ethan Elliott who rebuilt our lab along with James. When I first started my research, I shadowed him in the lab. I particularly enjoy the conversation I had with Ethan on every possible thing from movies to physics.

I would like to express my sincere gratitude to my husband and my lab partner Arunkumar Jagannathan for spending countless nights and weekends with me in the lab to complete my experiment. With his theoretical acumens and experimental knowledge, he guided me in the right direction every time I encountered an obstacle in my experiment.

I am particularly grateful for the assistance given by Ilya Arakelyan, the most modest person anyone can ever meet. I would also like to extend my thanks to other members of our group, Haibin Wu, Chenglin Cao, Yingyi Zhang, and Jayampathi Kangara Mudiyanselage for the helpful discussions during various stages of my research.

My special thanks to the graduate program coordinator, Rhonda Benett for taking care of all the paperwork needed to do even before asking. Her help and guidance made sure that I can graduate in a timely manner. A special thanks to physics department business officer Rebecca Savage, an absolute sweety and one of the most organized people that I have ever seen.

Finally, I wish to acknowledge the help and support provided by my Master's advisor Dr. Robert Giles and my professors Drs. Albert Altman, Kunnat Sebastian, James Egan, and Jayant Kumar.

TABLE OF CONTENTS

LIST OF TABLES

LIST OF FIGURES

CHAPTER

1

INTRODUCTION

Tunable interactions in ultracold gases have led to important breakthroughs in atomic physics over the past decade, including the realization of strongly interacting Fermi [O'H02; KZ08; Blo08] to the observation of Efimov trimers [Kra06]. Typically, interactions are tuned using a magnetic Feshbach resonance, where an external magnetic field tunes the energy of a colliding atom pair to be degenerate with a molecular bound state. However, magnetic tuning of interactions lacks high-resolution spatial control, due to the size of the magnetic coils used in ultracold experiments. Also, magnetic tuning cannot achieve fast temporal control due to the high-inductance of the coils. Optical control of interactions can achieve high-resolution in both space and time, but generally suffers from atom loss due to spontaneous scattering.

In this dissertation, I report on experiments to control two-body interactions in ultracold ^{6}Li atoms using a two-field optical method, where two optical beams ν_1 and ν_2 (Fig. 1.1a) are employed to control interactions while suppressing atom loss by destructive quantum interference. Further, I demonstrate that the two-field optical method achieves the same tunability of two-body scattering length a_{12} as magnetic tuning, potentially opening a new

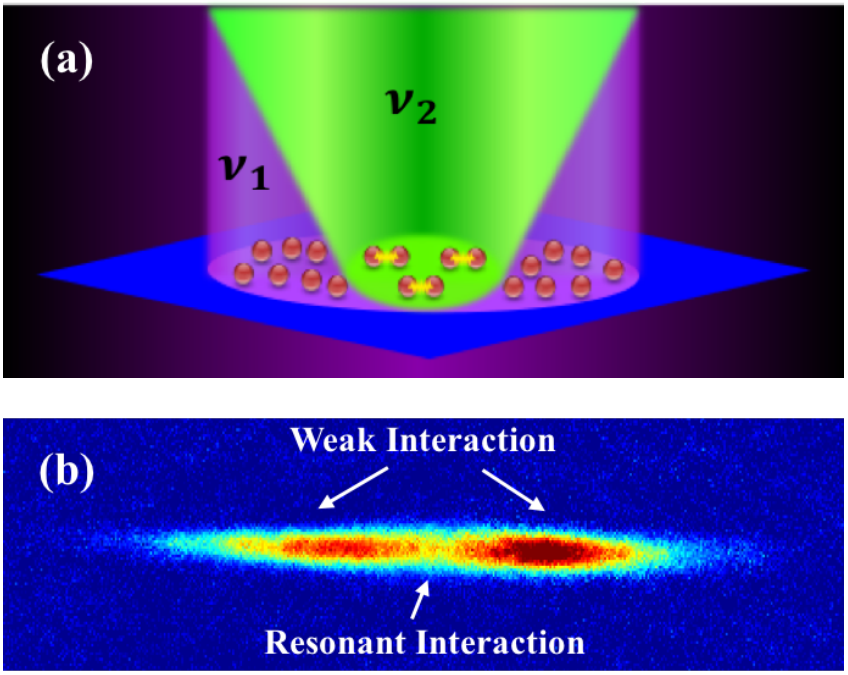

Figure 1.1 (a) The optical field arrangement for creating an interaction “sandwich." Both ν_1 and ν_2 beams illuminate the central region of the atomic cloud. The ν_1 and ν_2 beams make the central region of the atomic cloud resonantly interacting with suppressed spontaneous scattering. The outer regions of the atomic cloud illuminated *only* by the ν_1 beam are weakly interacting. (b) Measured atom cloud image illustrating an “interaction" sandwich. Atom cloud is imaged after transferring atoms from one hyperfine spin state to another, by applying a radio-frequency pulse. Atom transfer is suppressed in regions of resonant interactions-central region of the atomic cloud.

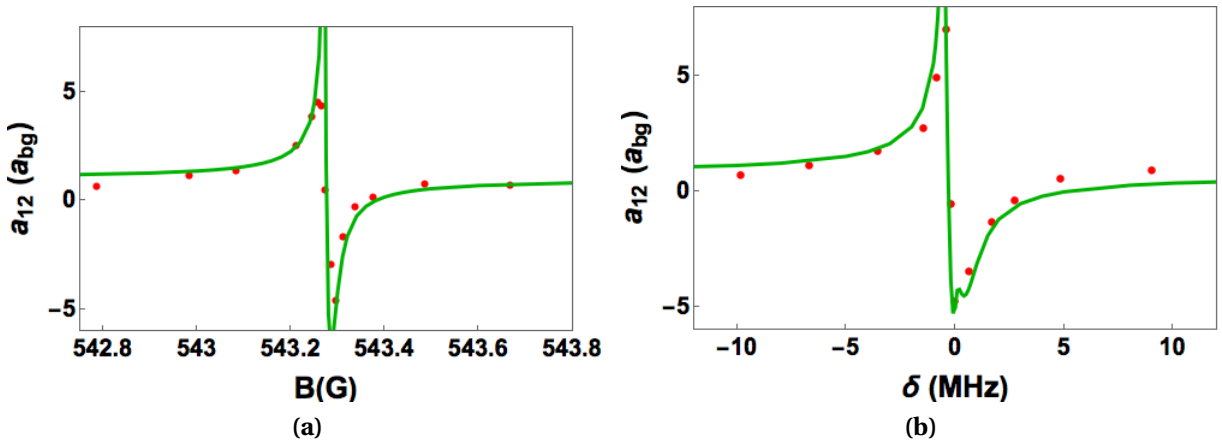

Figure 1.2 Comparison of (a) magnetically controlled and (b) two-field optically controlled scattering length $\bar{a}_{12}$, illustrating that the two-field optical method achieves the same level of tunability in scattering length as magnetic tuning.

field of research, Fig. 1.2. Using this unprecedented level of tunability, I further demonstrate spatial control of interactions in an ultracold gas by creating an interaction sandwich of resonantly and weakly interacting regions in an atomic cloud. Fig. 1.1a shows the optical field arrangement to create spatially varying interactions. Here, the ν_1 beam illuminates the entire atomic cloud and ν_2 beam is confined to the central region of the atomic cloud. The central region of the atomic cloud illuminated by *both* the ν_1 and ν_2 beam are resonantly interacting, while the wings of the atomic cloud illuminated *only* by the ν_1 beam are weakly interacting, as seen from measured atom cloud images in Fig. 1.1b. Also, different interaction profiles can be imprinted on the atomic cloud by changing the frequency of the laser only by a few MHz. This is the first demonstration of “designer" spatial control of interactions in an ultracold gas, which has far-reaching applications such as emulating the physics of super solid [Bau09a]. I will further report on experiments employing the two-field optical method as an optical vernier to probe and study momentum-dependent interactions between atoms with high precision, where the momentum of an incoming colliding atom pair determines the interaction energy of the atoms.

For more than a decade, optically controlling interactions involved photoassociation coupling a pair of unbound free atoms to a bound molecular state, thereby changing the scattering cross-section of the colliding atom pair [The04]. However, this resulted in atom loss due to spontaneous scattering, which reduced the lifetime of atoms to a few

hundred microseconds. Pioneering work in 2009 by Rempe's group at the Max Planck Institute of Quantum Optics used a combination of optical fields and magnetic fields to control collisional interactions [Bau09a]. Here, the magnetic field tunes the energy of the free atom pair near a Feshbach resonance and the optical field tunes the energy of the nearby molecular bound state. When the energy of the free atom pair (magnetic tuning) is degenerate with the energy of the molecular bound state (optical tuning), the scattering cross-section diverges, resulting in strong interactions. Although this technique improved the lifetime of the atoms to 1 ms, there was always a trade-off between achieving longer lifetime and increasing the tunability of interactions. In other words, long lifetimes imply small tuning ranges, which is inadequate for most applications. In 2012, our group proposed new two-field optical methods [WT12a; WT12b], based on quantum interference to suppress atom loss. Here, two optical fields, as opposed to the single optical field [Bau09a], are used to control collisional interactions.

The underlying principle of the two-field method is that there are two pathways coupling an atom in the ground state to an excited state. The two pathways can destructively interfere, leaving the atom in the ground state. Here, the two optical fields will create a "dark" state, where the atoms can reside, without being effectively coupled to the excited state, thereby suppressing atom loss. A related technique was demonstrated by Harris in 1984 at Stanford University and is well known as electromagnetically induced transparency (EIT) [Har97] for suppressed absorption. Our two-field method is a marriage between the single-field method pioneered by Rempe [Bau09a] and the EIT technique developed by Harris [Har97] to optically control collisional interactions in ultracold gases. Hence, the two-field method is also referred to as the closed-channel EIT method.

Optical control of interactions in ultracold gases has wide applications, from creating novel quantum phases to emulating the physics of strongly interacting systems such as the neutron matter. Optical techniques can achieve high-resolution spatial control of interactions in an ultracold gas, which can be utilized to study controllable soliton emission [RV05], exotic quantum phases [Den08], long-living Bloch oscillations of matter waves [Sal08], the physics of Hawking radiation from black holes [Bal08]. Optical control of interactions can also provide fast temporal control, which can be used for rapid modulation of interactions to study "driven" quantum systems such as a "Bosenova" [Cla17] - an exploding fireworks of Bose gas when the interactions are rapidly modulated (ms) resembling the collapse and bounce of a supernova. Fast temporal control is also critical in investigating

non-equilibrium thermodynamics in Fermi gases. Based on the demonstration of a new two-field optical method from our group, it has been predicted that our method can be used for momentum-selective control of interactions, leading to the realization of synthetic Fulde-Ferrel superfluids [He18]. Further, the two-field optical method also can be used to control the effective range with minimum loss, which is critical in emulating the physics of neutron matter.

I will begin this chapter by presenting a brief overview on magnetically tunable interactions in ultracold gases, followed by a historical perspective on the different kinds of optical methods that have been developed to control interactions in ultracold gases.

1.1 Magnetic Feshbach Resonance

Feshbach resonance occurs when the energy of a pair of colliding atoms is degenerate with a bound state in a closed channel. At the Feshbach resonance, the scattering length diverges and the scattering cross-section becomes maximum. This leads to strong interactions between the colliding atoms, which can be exploited to emulate the physics of other strongly interacting systems in the universe such as neutron stars and quark-gluon plasma. Typically, magnetic fields are used to tune the energy of the colliding atom pair relative to the energy of the molecular bound state. This has led to the widely used terminology in the ultracold physics community, magnetic Feshbach resonances (MFR). In this section, I will discuss the importance of magnetic Feshbach resonances in achieving tunable interactions in ultracold gases.

Fig. 1.3 illustrates a magnetic Feshbach resonance. The colliding atoms predominantly reside in the energetically accessible open channel. The molecular bound state $|g_1\rangle$, which is not energetically accessible to the atoms is called the closed channel. In our laboratory, ^{6}Li fermions are used to study ultracold atomic collisions. At ultracold temperatures, the predominant collisions arise from low energy s-wave scattering. A two-component mixture of atoms with different total atomic spins, represented by black arrows on the atoms (red balls) in Fig. 1.3, is needed for an s-wave collision to happen between two ^{6}Li fermionic atoms. Hence, the two lowest hyperfine states $|1\rangle$ and $|2\rangle$ in ^{6}Li are used to study atomic collisions (Refer to Chapter 2 for a detailed treatment of the hyperfine states in ^{6}Li). For the $|1\rangle - |2\rangle$ mixture, the open channel is the spin triplet state $|T, k\rangle$ and the closed channel is the spin singlet state $|g_1\rangle$. Here T represents the total electronic spin of the atom pair and k

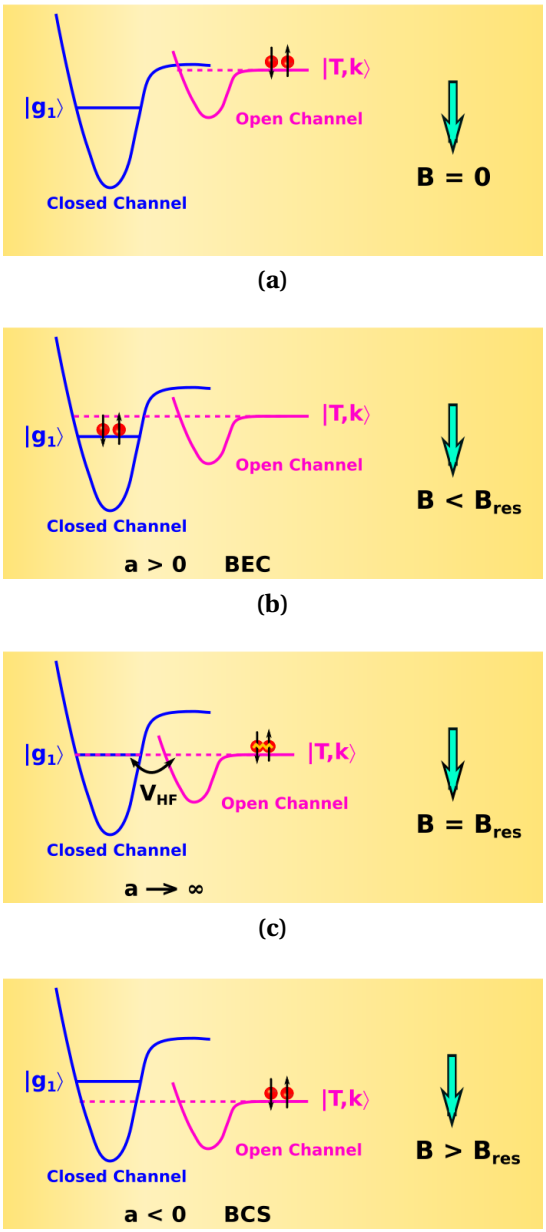

Figure 1.3 Magnetically tuning interactions near a Feshbach resonance. The hyperfine coupling between the triplet continuum $|T,k\rangle$ (open channel) and the singlet bound state $|g_1\rangle$ cause magnetic Feshbach resonance. The open channel $|T,k\rangle$ is magnetically tunable due to its non zero magnetic moment. (a) At B = 0, the triplet continuum $|T,k\rangle$ is higher in energy than the molecular bound state $|g_1\rangle$. (b) At B < B_{res}, the triplet continuum $|T,k\rangle$ is above the molecular bound state $|g_1\rangle$. This is the BEC regime of the resonance. (c) At B = B_{res}, the triplet continuum $|T,k\rangle$ is degenerate with the molecular bound state $|g_1\rangle$ and leads to the Feshbach resonance. (d) At B > B_{res}, the triplet continuum $|T,k\rangle$ is below the molecular bound state $|g_1\rangle$. This is the BCS regime of the resonance.

represents the relative momentum between them. In the open channel triplet continuum $|T,k\rangle$ state, the electronic spin of both the atoms is downward and therefore has a net magnetic moment $-2\mu_B$, where $\mu_B = \hbar \times 1.4$ MHz/G is the Bohr magneton. Hence, in the presence of an external magnetic field B, the triplet continuum $|T,k\rangle$ moves downward and its energy is proportional to $-2\mu_B B$. For the singlet state $|g_1\rangle$, the electronic spins of both the atoms are opposite and have a zero net magnetic moment. Therefore, the pure singlet state $|g_1\rangle$ is not magnetically tunable.

Applying an external magnetic field B_{res}, the energy of the triplet continuum $|T,k\rangle$ is tuned to be degenerate with the singlet molecular bound state $|g_1\rangle$, causing a Feshbach resonance, Fig. 1.3c. Many important works have been done in the ultracold physics community [Zwi05; Sch07; Zwi06; Ste08; Joc03; Reg03] and in our group [O'H02; Kin04; Kin05; Cao11] where the strong interactions created by a magnetic Feshbach resonance was exploited to realize strongly interacting Bose and Fermi gases.

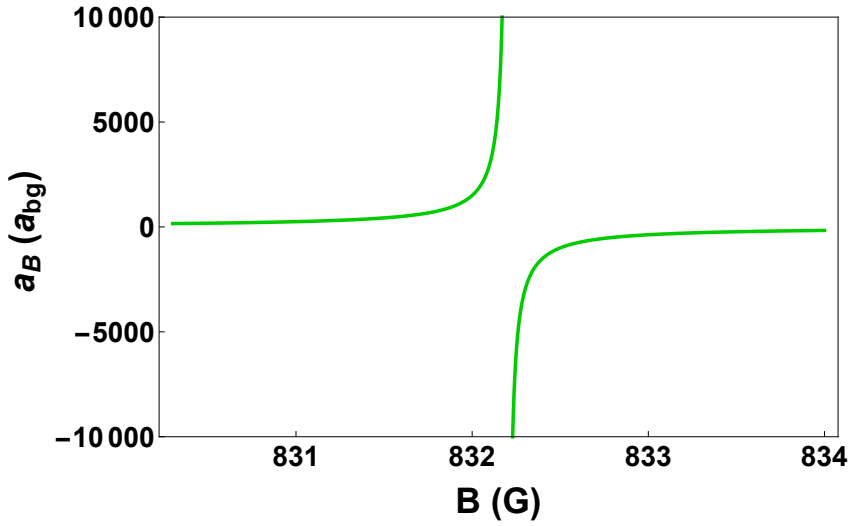

Figure 1.4 Zero energy scattering length a as a function of magnetic field B in units of background scattering length a_{bg} for the broad Feshbach resonance at 832.2 G with width $\Delta B = 300$ G. The background scattering length a_{bg} for the broad Feshbach resonance in ^{6}Li is -1450 a_0.

When the applied external magnetic field $B < B_{res}$, Fig. 1.3c, the energy of the triplet continuum $|T,k\rangle$ is slightly above the energy of the molecular bound state $|g_1\rangle$. Here, the scattering length is positive and the interactions between the atoms are repulsive. This

leads to the formation of weakly-bound molecules, namely, Feshbach molecules. Here, two ^{6}Li fermionic atoms can form a Bosonic ^{6}Li-^{6}Li molecule, which under low enough temperatures can undergo a phase transition to form a Bose-Einstein condensate (BEC). This regime is called the BEC side of the resonance and has been widely utilized to realize ultracold molecules by a number of methods, namely, 1) performing an adiabatic sweep of the magnetic field from above the resonance to below the resonance to create ultracold ^{40}K molecules [Reg03], 2) exploiting three-body recombination on the BEC side of the resonance to realize cold ^{6}Li molecules [Joc03], and 3) modulating the magnetic field slightly above the BEC regime to create ultracold ^{85}Rb molecules [Tho05]. More recently, Feshbach resonances have been exploited to realize extremely stable long-lived ultracold molecules of ^{23}Na^{40}K in their ground state [Wu12].

When the applied external magnetic field $B > B_{res}$, Fig. 1.3d, the energy of the triplet continuum $|T,k\rangle$ is below the energy of the molecular bound state $|g_1\rangle$. Here, the scattering length is negative and the interactions between the atoms are attractive. The behavior of the colliding atoms at low enough temperatures in the presence of a Fermi sea mimics the behavior of Cooper pairs in superconductors. Therefore, BCS (Bardeen-Cooper-Schrieffer) theory is required to explain the physics of atomic collisions and hence this regime is called BCS side of the resonance. The tuning of interactions from the BEC side to the BCS side of the resonance is famously known as the BEC-BCS crossover (Fig. 1.4) and has been critical in many important studies in ultracold atomic physics.

1.2 Limitations of the Magnetic Feshbach Resonance

In the last section, the advantages of magnetic Feshbach resonance (MFR) in achieving tunable interactions in ultracold gases was discussed. Although using external magnetic fields to control interactions has been effective in studying and emulating quantum phenomenon over the last couple of decades, MFR'S suffer from certain shortcomings that severely limits their applicability. One of the main limitations in using external magnetic fields to control interactions is the lack of high-resolution spatial control. This is primarily due to the size of the coil that is employed to generate the magnetic fields. For example, in our laboratory, our electromagnets have a diameter of 6 inches ($152\times10^3\mu$m) which generates a uniform magnetic field on the atoms. However, the atom cloud size is about 140 μm, which is 1000 times smaller than the size of the magnetic coils. Hence, it is impossible

to achieve spatially selective control of interactions within an atom cloud.

Another limitation of using a magnetic field to control interactions is its slow tunability. The coils used to generate magnetic fields have a high inductance, which severely limits the rate of change of current through the coil. For example, the magnetic coils in our laboratory have an inductance of 5 mH, which results in a time constant of 800 ms. In all the experiments reported in this thesis, I wait 800 ms for the magnetic fields to stabilize. In several other groups, single turn coils with low inductance in combination with a primary coil have been used to demonstrate control of interactions in the time scale of 1 ms [Tho05; Xu03; Hu14]. However, in order to study non-equilibrium thermodynamics, the interactions should be controlled in a much faster timescale. For example, the natural time scale in a Fermi gas is the Fermi time, τ_F, which is defined as the time taken by a fermion with velocity v_F to move a Debrogile wavelength λ_F. For a Fermi Energy, $E_F \approx k_B \times 1\mu$K, the Fermi time is in the order of $10\,\mu$s. To study the non-equilibrium thermodynamics of interacting Fermi gases, the interactions need to be controlled on a time scale faster than the Fermi time, such that the dynamics of the system prior to reaching equilibrium can be systematically studied. Hence, experiments involving studies of non-equilibrium thermodynamics are not readily performed using a magnetic Feshbach resonance.

It has been suggested for a long time that high-resolution spatial control and fast temporal control can be achieved by using optical fields to control interactions. More recently, based on the work from our group [Jag16a] on optically manipulating interactions near Feshbach resonances, it was also suggested that momentum-selective control of interactions using optical fields can be used to realize synthetic Fulde-Ferrel superfluids [He18]. In past theoretical work from our group [WT12a; WT12b], it was proposed that optical control of interactions can be further used to control the effective range in an atomic collision, which is critical in the emulation the physics of neutron matter. Therefore, in order to achieve high-resolution spatial and fast temporal control as well as momentum-selective control of interactions and manipulation of effective range, the use of optical fields becomes inevitable.

1.3 Controlling Interactions using Optical Fields

Optical fields can be easily manipulated to achieve high-resolution spatial control and fast temporal control of interactions. The size of an optical beam can be controlled by carefully

designing an optical system with lenses and opto-mechanical devices to make the size of the beam comparable to the size of the atom cloud. Also, technological breakthroughs have led to the development of digitally modulated mirror arrays, where a different spatial pattern of the optical field can be imprinted on the atoms with resolutions better than a couple of microns. Therefore, optical fields can easily be used to achieve high-resolution spatial control of interactions. The optical fields can be switched on or off in tens of nanoseconds by using an optical switch like acousto optical modulator (AOM). The AOM can also frequency or amplitude modulate the optical beams at a frequency limited only by its switching time. Hence optical fields can provide high resolution in both position and time.

Although optical control of interactions has been a primary candidate for overcoming the shortcomings of magnetic Feshbach resonances (discussed in the previous section), there have been only a handful of experiments in this field. Optical control techniques, in general, suffer from spontaneous scattering resulting in atom loss. This happens as atoms in an optical field are coupled to an excited state and decay due to spontaneous emission, resulting in the heating of the atoms, which eventually escape from the trapping potential used to cool them. The problem of overcoming spontaneous scattering and achieving reasonable lifetime for the atoms resulted in limited progress until 2009 [Bau09a], where a combination of optical fields and magnetic fields were used to control interactions. In this section, I will present a general overview of the different types of optical methods, both successful and unsuccessful in controlling interactions with reasonable lifetimes for the atoms, in order to present the reader with a clear picture of the progress made over the years that have made this thesis research a possibility.

1.3.1 Optical Feshbach Resonance (OFR)

The idea of optical Feshbach resonance was proposed theoretically in the late 1990's [BJ97; Fed96]. However, the first experimental demonstration of optical Feshbach resonance was reported only in 2004 in a Bose condensate of ^{87}Rb [The04]. Fig. 1.5 illustrates the concept of optical Feshbach resonance. An optical field couples the incoming unbound atoms in the open channel to a bound state of the excited vibrational level of the same open channel. The transition frequency and the Rabi frequency of the optical beam are ν and Ω respectively.

In contrast to the magnetic Feshbach resonance where the unbound atoms in the open channel are coupled to the bound state of the closed channel, the optical Feshbach resonance couples the unbound atoms to the electronically excited bound state of the same

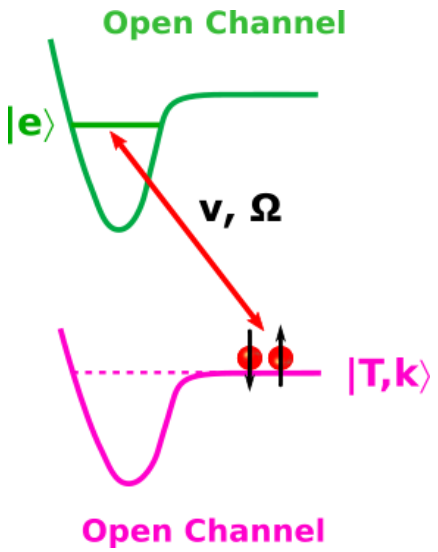

Figure 1.5 Energy level scheme for optical Feshbach Resonance. Colliding atoms reside in the triplet potential. The triplet continuum $|T,k\rangle$ (open channel) is coupled with the triplet excited bound state $|e\rangle$ (open channel) through an optical beam of frequency ν and Rabi frequency Ω.

open channel. This method of optically coupling the colliding atoms to the excited bound state of the open channel is called photoassociation. The optical Feshbach resonance employs photoassociation resonance to tune interactions. M. Theis and coworkers [The04] showed a change in the scattering length from 10 a_0 to 190 a_0, where a_0 is the Bohr radius. This corresponds to approximately $\pm$ 1 a_{bg}, where a_{bg} is the background scattering length and is equal to 100.5 a_0 for ^{87}Rb. In order to be consistent across several different species of ultracold atoms, I will give the scattering length in units of a_{bg}.

Although tuning of scattering length was illustrated using OFR, the major disadvantage of using optical field is the atom loss due to spontaneous scattering. When the unbound atoms are pumped from the ground state to the excited bound state of the open channel, they spontaneously decay to any of the allowed lower lying vibrational states. This leads to atom loss, which is characterized by the two-body loss rate coefficient K_2. The unit of K_2 is cm^3/s. [The04] were able to achieve a K_2 of 10^{-10} cm^3/s. For a BEC with a typical density of 10^{14} cm^{-3}, this K_2 corresponds to a lifetime of 100 μs. The lifetime of 100 μs limits the timescale of the experiments utilizing OFR.

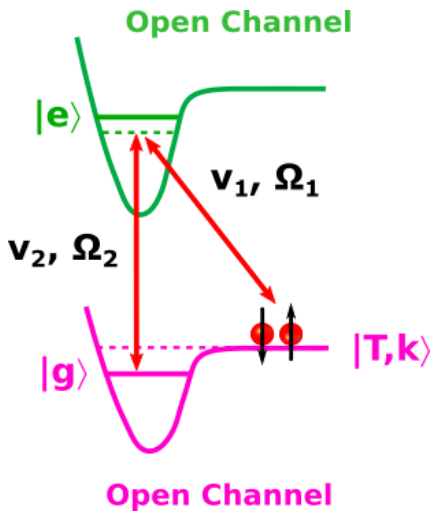

Figure 1.6 Energy level scheme for two-field optical Feshbach Resonance. The triplet continuum $|T,k\rangle$ (open channel) is coupled with the triplet excited bound state $|e\rangle$ (open channel) through an optical beam of frequency ν_1 and Rabi frequency Ω_1. A second optical field with the frequency ν_2 and Rabi frequency Ω_2 couples the vibrational state $|g\rangle$ of the ground open channel to the same excited bound state $|e\rangle$ of the open channel.

1.3.2 Two-field Optical Feshbach Resonance

To further improve the lifetime of OFR experiments, M. Theis and coworkers [Tha05] improvised the OFR scheme by using two optical fields. This two-field technique utilizes the principle of two-photon Raman coupling, Fig. 1.6. In this technique, a second optical field couples the ground molecular vibrational state $|g\rangle$ of the open channel to the excited molecular vibrational state $|e\rangle$ of the open channel. The frequency and the Rabi frequency of the second optical beam are ν_2 and Ω_2, respectively. This method provides additional flexibility in controlling the interactions by offering two additional control parameters, ν_2 and Ω_2. However, this scheme did not improve the overall tunability of interactions or the lifetime of the atoms when compared to single field methods. In their published work, they declared that there are no additional advantages of using two optical fields as opposed to a single optical field, which is not particularly the case as we will see later in this chapter.

1.3.3 Optical Control of Magnetic Feshbach Resonance

A major breakthrough in the optical control field occurred when Bauer and coworkers illustrated tuning of scattering length by manipulating the ground state of the closed

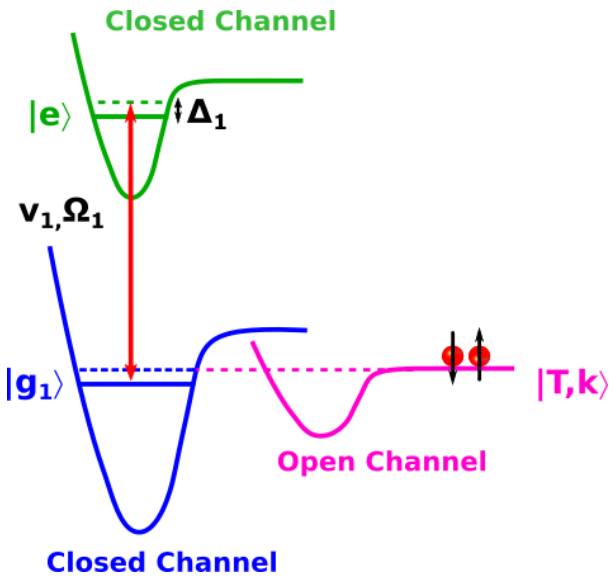

Figure 1.7 Energy level scheme for the optical control of magnetic Feshbach Resonance. The incoming atoms are in the triplet continuum $|T,k\rangle$ (open channel). The ground state $|g_1\rangle$ and the excited state $|e\rangle$ are the bound vibrational levels of the singlet potential (closed channel). The singlet ground state $|g_1\rangle$ is coupled to the singlet excited state $|e\rangle$ through an optical beam of frequency ν_1 and Rabi frequency Ω_1.

channel near a Feshbach resonance in ^{87}Rb [Bau09a]. Unlike the open channel technique (optical Feshbach resonance) [The04; Tha05], this technique can only be realized near a magnetic Feshbach resonance. The fundamental idea is to use a combination of both optical and magnetic fields to control interactions. The external magnetic field acts as a coarse control parameter to tune the open channel near the closed channel and an optical field acts as a fine control parameter to tune the interactions. Hence this technique is denoted as the optical control of a magnetic Feshbach resonance. In many papers, optical control of a magnetic Feshbach resonance is sometimes loosely referred to as optical Feshbach resonance, which is incorrect. As we will see in this section, the two techniques differ considerably in the way they tune the interactions and should not be confused with one another.

Fig. 1.7 shows the energy level scheme for the optical control of magnetic Feshbach resonance technique using single optical field [Bau09a]. In addition to the triplet continuum $|T,k\rangle$ and the singlet bound state $|g_1\rangle$, this technique also utilizes the excited bound vibrational level $|e\rangle$ of the closed channel (singlet state). An optical beam ν_1, with Rabi frequency Ω_1 and detuning Δ_1, couples the singlet ground state $|g_1\rangle$ to the singlet excited

state $|e\rangle$. Due to AC Stark effect, the optical beam ν_1 shifts the ground state $|g_1\rangle$ to $|g_1^{'}\rangle$. The shift in the ground state $|g_1\rangle$ is proportional to $\Omega_1^2/4\Delta_1$.

In this technique, the triplet continuum $|T,k\rangle$ is tuned magnetically and brought near but not degenerate with the singlet ground state $|g_1\rangle$. Then, by manipulating the Rabi frequency Ω_1 or the frequency ν_1, the singlet ground state $|g_1\rangle$ can be made degenerate with the triplet continuum $|T,k\rangle$, thereby achieving strong interactions. Using this technique, Bauer and coworkers [Bau09a] were able to demonstrate an order of magnitude improvement in the lifetime of atoms for the same amount of tunability in scattering length as the optical Feshbach resonance technique [The04]. This increase in the lifetime of atoms was possible because the optical field manipulates the closed channel (singlet ground state), whereas the atoms reside in the open channel (triplet continuum) which is far detuned. Bauer and coworkers [Bau09b] further achieved an order of magnitude improvement in the lifetime of the atoms by using large detuning Δ_1. Fu and coworkers [Fu13] reproduced the same experiment in ^{40}K and demonstrated the tunability of scattering length.

Even though this technique controls the two-body scattering length near a Feshbach resonance, the lifetime of the atoms is limited by spontaneous scattering. Since the two-body loss rate is proportional to $\Omega_1^2/4\Delta_1^2$, they use large detuning Δ_1 to achieve an increase in the lifetime of atoms. As the light shift of the ground state $|g_1\rangle$ is proportional to $\Omega_1^2/4\Delta_1$, using large detuning Δ_1 limits the tunability in scattering length. Also in the large detuning regime, tuning scattering length by tuning the frequency ν_1 produces a negligible effect. Hence, this method requires to tune the Rabi frequency Ω_1. Since the optical beam creates an optical potential for the atoms in addition to the trap potential, changing the Rabi frequency Ω_1 modifies the net trapping potential, which can create undesired effects on the atoms.

1.3.4 Optical Control of Magnetic Feshbach Resonance using a “Magic" Wavelength

To minimize the effect of trapping potential due to the optical beam ν_1, Clark and coworkers [Cla15] tuned the optical beam ν_1 between the D_1 and D_2 atomic transition lines of the cesium atoms. When the optical beam ν_1 is tuned between D_1 and D_2 lines, the atomic polarizability due to D_1 and D_2 transitions cancel each other, thereby creating a negligible trapping effect on the atoms. This wavelength is called as magic wavelength. Clark and coworkers used the same technique as Bauer and coworkers [Bau09a] with a fixed detuning

and achieved a tunability of only 0.2 a_{bg} in scattering length with a lifetime of 0.63 s.

However, this technique has some fundamental limitations in its scope and applicability. In the case of Cs atoms used by Clark and coworkers, the D_1 and D_2 transition lines are separated by 16 THz. But for the atoms like ^{6}Li, the D_1 and D_2 transition lines are separated by 10 GHz. The optical beam tuned between D_1 and D_2 transition lines in ^{6}Li, cause huge atom loss due to spontaneous scattering. Hence this technique of tuning interaction with a magic wavelength cannot be adapted to other species like ^{6}Li and are therefore not universally applicable.

Using this technique, Clark and coworkers also demonstrated temporal control of interactions in the atomic cloud by modulating the intensity of the optical field. By creating intensity variation of the optical beam within an atom cloud, they also demonstrated the spatial variation of interactions in an atomic cloud. Clark and coworkers claim an observation of soliton "like" behavior in the atomic cloud and the collapse of a Bose-Einstein condensate when local interactions are tuned from attractive to repulsive by changing the magnetic field. However, there was no theoretical treatment to support their claim and it was further clouded by the fact that the observed signature of soliton "like" behavior is very similar to just atoms loss due to optical field.

In addition, they parametrized their tunability in terms of absolute value of the scattering length. In the first important work on optical control of interactions published by Rempe's group in 2009 [Bau09a] and in all previously published work from our group [WT12a; WT12b], tunability of scattering length was parametrized in terms of a_{bg} and I will use the same methodology in this thesis.

1.4 Two-field Optical Control of Magnetic Feshbach Resonance

The major disadvantages of single field optical control of magnetic Feshbach resonance are the limited tunability of the scattering length and the short lifetime of atoms. To overcome these problems, our group proposed a two-field optical technique [WT12a; WT12b] using electromagnetically induced transparency (EIT) to control interactions near a magnetic Feshbach resonance, Fig. 1.8. EIT [Har97] was pioneered by Harris in the mid-eighties at Stanford University, where he demonstrated two-optical fields coupled in a three-level system can be used to achieve either constructive or destructive quantum interference

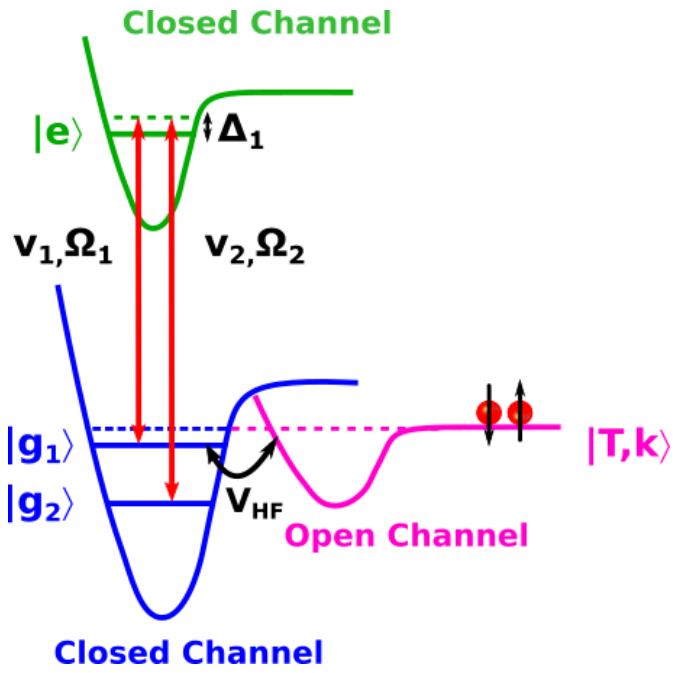

Figure 1.8 Energy level scheme for the two-field optical control of magnetic Feshbach Resonance. The incoming atoms are in the triplet continuum $|T,k\rangle$ (open channel). The ground states $|g_1\rangle$, $|g_2\rangle$ and the excited state $|e\rangle$ are the bound vibrational levels of the singlet potential (closed channel). The singlet ground state $|g_1\rangle$ is coupled to the singlet excited state $|e\rangle$ through an optical beam of frequency ν_1 and Rabi frequency Ω_1. A second optical field with the frequency ν_1 and the Rabi frequency Ω_2 couples the singlet ground state $|g_2\rangle$ to the same excited state $|e\rangle$.

between the transition pathways. In the case of destructive quantum interference, EIT can achieve loss suppression in the absorption spectra of the atoms by creating a transparency window, which can be used to suppress atom loss [Fle05; Har97], realize slow-light [Hau99] etc., In the case of constructive interference, EIT enhances the transition probability, which can be exploited to realize inversionless lasers [Har97]. The basic idea of the two-field control of magnetic Feshbach resonance is to use EIT in the closed-channel to suppress atom loss and therefore the two-field method of controlling MFR is also referred to as closed-channel EIT [Jag16a].

In the two-field method, Fig. 1.8, in addition to the ground state $|g_1\rangle$ and the excited state $|e\rangle$, the two optical field technique requires a lower lying vibrational level $|g_2\rangle$ of the singlet ground potential. The optical beam ν_1 (Rabi frequency Ω_1) couples the ground state $|g_1\rangle$ to the excited state $|e\rangle$ and the optical beam ν_2 (Rabi frequency Ω_2) couples the ground state $|g_2\rangle$ to the excited state $|e\rangle$. The optical beams ν_1 and ν_2 shift the ground state $|g_1\rangle$ and

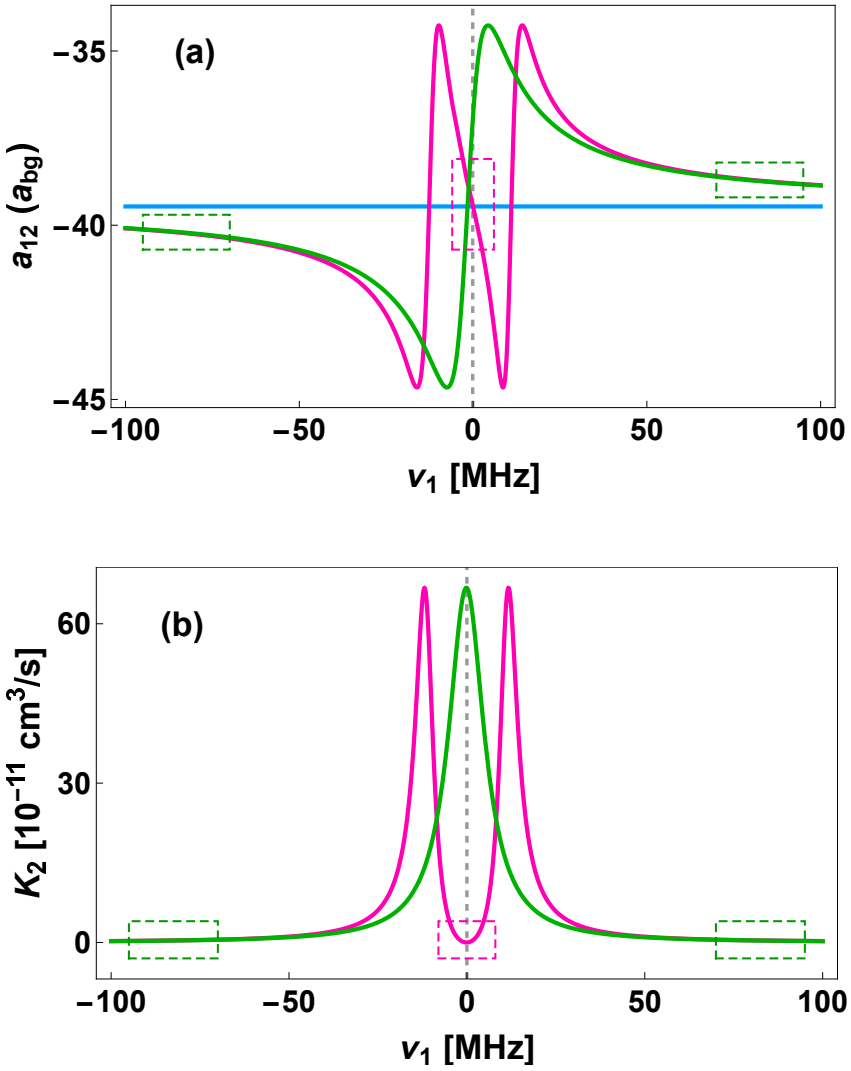

Figure 1.9 Why two-field method is better than single-field methods for optical control of a magnetic Feshbach resonance - A simple illustration. (a) Zero energy scattering length a_{12} and (b) two-body loss rate coefficient K_2 as function of laser frequency ν_1 for single-field (green) and two-field (magenta) optical control of magnetic Feshbach resonance. The blue line in (a) is the zero energy scattering length a_{12} in the absence of the optical fields. The low loss regions for single-field and two-field methods are indicated by the green and magenta boxes, respectively. The parameters used are T = 5 μK, B = 840 G, $\Omega_1 = 1\gamma_e$, and $\Omega_2 = 2\gamma_e$.

manipulate the scattering interactions of the atoms. In addition, the presence of ν_1 and ν_2 beams creates two different pathways for the atoms to reach the excited state resulting in a destructive quantum interference. This results in suppression of atom loss and the creation of a transparency window on the absorption spectra. Minimum loss occurs when the frequency difference between the ν_1 and ν_2 beam equals the energy difference (in frequency units) between the states $|g_1\rangle$ and $|g_2\rangle$ (see Chapter 2 for a detailed description).

The advantages of the two-field method over single field methods can be quantitatively explained in a simple way using Fig. 1.9. Here I compare the two-body loss rate constant K_2 Fig. 1.9b and scattering length tunability Fig. 1.9a as a function of frequency ν_1 for both two-field method (shown in magenta) and the single-field method (shown in green). The blue line in Fig. 1.9a is the zero energy scattering length a_{12} in the absence of the optical fields. The parameters used to generate Fig. 1.9 are T = 5 μK, B = 840 G, $\Omega_1 = 1\gamma_e$, and $\Omega_2 = 2\gamma_e$. In the K_2 plot, for the single-field method (shown in green) minimum loss occurs for large detunings (Fig. 1.9b-green dotted box). Looking at the same region of detuning in the scattering length plot a (Fig. 1.9a-green dotted box), we find that the tunability in scattering length is limited. However, for the two-field method (shown in magenta), minimum loss occurs when the detuning in zero (Fig. 1.9b-magenta dotted box). Looking at the zero detuning regime in the scattering length plot (Fig. 1.9a-magenta dotted box), we can see that the change in scattering length is maximum. Therefore, we can clearly see that the two-field method creates a minimum loss regime, around which it offers maximum tunability in scattering length. Also, from Fig. 1.9, we see that the tunability can be easily achieved with MHz changes in frequency for the two-field method rather than several hundreds of MHz frequency change that are required in the case of single-field methods.

Fig. 1.10a and Fig. 1.10b illustrates the ratio K_2/a for both single-field and two-field methods, respectively. For the single-field method Fig. 1.10a, a tunability of $\Delta a = 5\, a_{bg}$ ($A \rightarrow B$ or $A' \rightarrow B'$) results in a two-body loss rate constant of $K_2 = 27 \times 10^{-11}\text{cm}^3/\text{s}$. Also to tune the scattering length $A \rightarrow B$ or $A' \rightarrow B'$, the frequency ν_1 has to be changed from -100 MHz to -7.5 MHz or from +100 MHz to +3.5 MHz, respectively. Note that the scattering length cannot be tuned from A (-100 MHz) $\rightarrow A'$(+100 MHz) as the gap between A and A' involves maximum loss. For the two-field method Fig. 1.10b, for the same level of tunability of $\Delta a = 5\, a_{bg}$ ($C \rightarrow D$) results in a two-body loss rate constant of only $K_2 = 3.6 \times 10^{-11}\text{cm}^3/\text{s}$, which is 7 times smaller than the single-field method. To modify the scattering length from $C \rightarrow D$, the frequency ν_1 has to be changed only from -4.5 MHz to +4.5 MHz. Therefore,

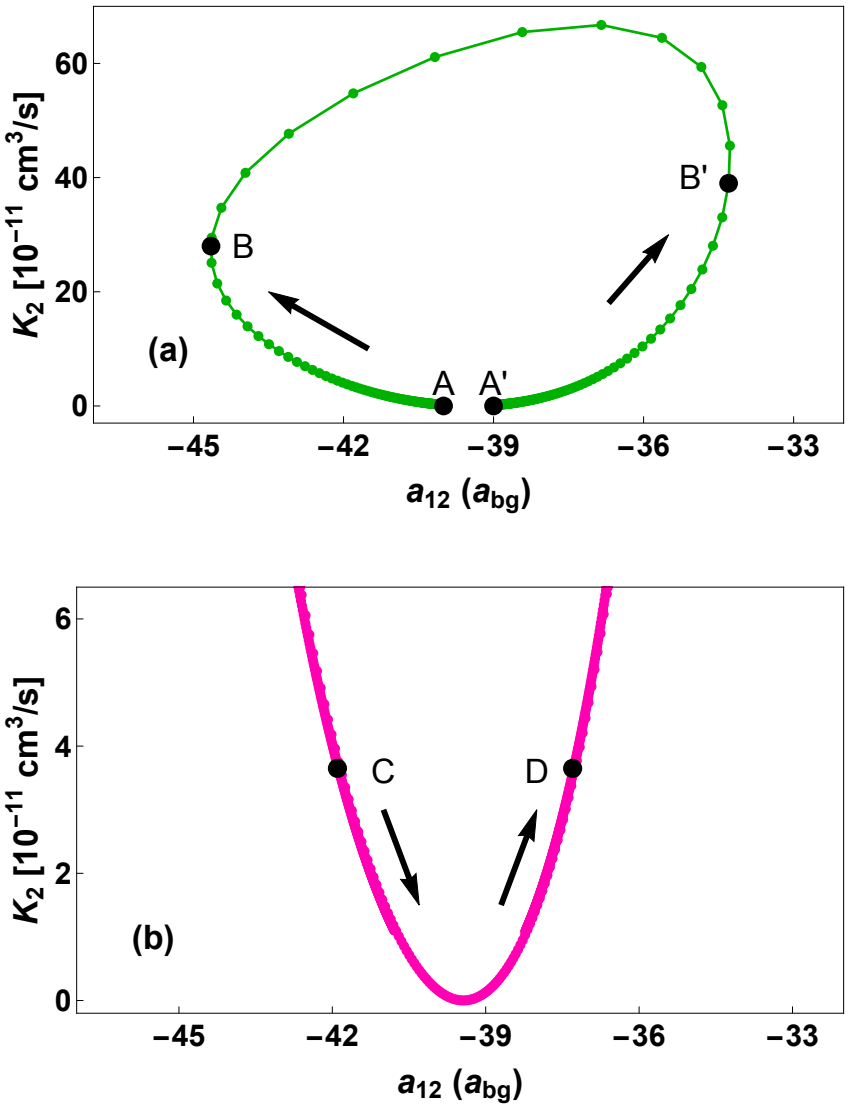

Figure 1.10 Quantitative illustration of the superiority of two-field method over single-field methods for optically controlling a magnetic Feshbach resonance. Two-body loss rate constant K_2 Versus zero energy scattering length a_{12} for (a) single-field and (b) two-field optical control of magnetic Feshbach resonance, using the same experimental parameters as in Fig. 1.9. For the single-field method, a tunability of $\Delta a = 5\,a_{bg}$ ($A \rightarrow B$ or $A' \rightarrow B'$) results in a two-body loss rate constant of $K_2 = 27 \times 10^{-11}\text{cm}^3/\text{s}$. Note that the scattering length cannot be tuned from A (-100 MHz) $\rightarrow A'$(+100 MHz) as the gap between A and A' involves maximum loss. For the two-field method, for the same level of tunability of $\Delta a = 5\,a_{bg}$ ($C \rightarrow D$) results in a two-body loss rate constant of only $K_2 = 3.6 \times 10^{-11}\text{cm}^3/\text{s}$, which is 7 times smaller than the single-field method.

from the illustration in Fig. 1.10, it is clear that the two-field closed channel EIT method is far superior than the single-field methods for optically controlling magnetic Feshbach resonances.

1.5 Significance of My Thesis Work

In my Ph.D. research, I used the closed-channel EIT method described in the previous section to demonstrate optical control of interactions and designer spatial control of interactions in an ultracold gas of ^{6}Li atoms. The tunability of interactions was demonstrated by employing radio-frequency (RF) spectroscopy to measure mean-field induced spectral shifts, from which the two-body scattering length was determined. Further, it was demonstrated that our method achieves the same level of tunability as magnetically tuning the interactions. This is the first demonstration where an optical technique has achieved the same level of tunability as a magnetic control.

Spatial control of interactions was demonstrated by creating an interaction “sandwich" of resonantly and weakly interaction regions within an atomic cloud. Further, by making small frequency changes of the ν_2 beam, different interaction profiles were imprinted on the atomic cloud. This work presents the first all-optical manipulation of spatial interaction profiles in an ultracold gas. I will briefly summarize my role in achieving the above-mentioned results.

During my research, I was involved in building the entire optical system (Section 3.2) for generating the ν_1 and ν_2 optical beams in the closed-channel EIT scheme (Fig. 1.8). The optical system comprises three different lasers, namely, the reference laser, the ν_1 laser, the ν_2 laser, and in addition, a Fabry-Perot cavity, an iodine saturation absorption spectroscopy setup, and a wide range of electronics and servo systems. To generate the ν_1 and ν_2 optical beams with a frequency stability of better than 30 kHz (1 part in a billion), three different locking schemes were implemented separately and were combined to work in unison.

Previous experiments from our group used an optical system where primary importance was given to the transition that involves the ν_1 beam i.e., the $|g_1\rangle - |e\rangle$ transition. For my experiments, the transition employing ν_2 beam i.e., $|g_2\rangle - |e\rangle$ transition had to be made much stronger. This involves hunting for new transition frequencies by performing two-photon laser spectroscopy. Due to the complicated nature of the laser locking scheme and the newly found transition frequencies, which were several GHz away from the old

transition frequencies, the entire setup was modified to accommodate the requirements of the new experiments.

Investigating two-body interactions near the narrow Feshbach resonance with a width of only 100 mG posed several challenges. Prior to my thesis research, the stability of our magnetic field was approximate ± 30 mG (1 minute) with drifts approximately ± 100 mG over 60 minutes. This made it impossible to pursue experiments near the narrow Feshbach resonance. The source of instability was the noise present in the current supply that powers the magnets. Hence, we bought a new power supply from Danfysik, which has a DC stability of better than 1 mG over 60 minutes. However, due to poor engineering choices from the manufacturer, the newly bought supply had a 60 Hz AC noise of approximately 100 mG.

As part of my Ph.D. research, I was built a servo system (Section 3.5) that reduced the AC ripple to less than 10 mG. The stability of the magnetic field was carefully measured and verified by performing radio-frequency (RF) spectroscopy. Also, after corresponding with the engineers at Danfysik about the noise issue over a period of at least 2 years, which involved sending them several measurements involving the current supply, I finally made them fix the engineering flaw in the current supply. This project of stabilizing the magnet system constituted a significant effort of my research and was critical in performing not only the optical control experiments, but new experiments in our group, such as the measurement of the zero-crossings in the scattering length which also requires exceptional magnetic field stability.

In order to demonstrate optical control of interactions, it is necessary to establish a method to measure the interactions. The interactions are measured in terms of the mean-field induced frequency shifts arising from the two-body scattering length a_{12}. In the case of Bose gases, a_{12} can be measured by just taking the image of the atom cloud. However, since I work with Fermi gases, measuring interactions was not that simple since the Fermi energy dominates. One of the ways to measure interactions in Fermi gases is to perform RF spectroscopy. Since optical control techniques generally induce atom loss, RF spectroscopy should be done on a timescale of a few ms. However, the RF system in our lab, which includes the RF antenna, the RF source, and the RF amplifier was extremely inefficient. Therefore, an RF pulse for a duration of at least 100 ms was required to perform spectroscopy.

As part of my research, I investigated the inefficiencies of our RF system and modified it for the needs of my experiment. First, the amplifier was upgraded from 3 W to 100 W. However, I did not see a corresponding improvement in the RF power transferred to the

atoms. On further investigation, it became clear that the issue was due to the RF antenna in the system that was built with poor impedance matching properties. Although the best solution would have been to replace the antenna present inside the vacuum chamber, due to the complications involved it breaking the vacuum, I was advised to work externally to fix this issue. A considerable amount of time during my research was spent on matching the impedance between the amplifier and the antenna by building impedance matching networks and choosing transmission lines of appropriate length. Finally, I was able to perform RF experiments (shown in Chapter 4 and Chapter 5) at 1.2 ms, which was a factor of 100 improvement over our older RF system.

1.6 Dissertation Organization

I will conclude this chapter by briefly summarizing the content in the forthcoming chapters. In this thesis, I will present both the experimental results for optical control of two-body scattering and a complete theoretical treatment to illustrate the excellent agreement of the data with theory.

In Chapter 2, I will introduce the continuum-dressed state theoretical model for two-field optical control of scattering interactions in ultracold gases. I use the continuum-dressed state model predictions in Chapter 2 to compare the experimental data presented in later chapters. The continuum-dressed state model provides a complete treatment of two-body scattering by considering the momentum dependence in interactions, which is neglected by prior theoretical models [Bau09a; WT12a; WT12b]. Using the continuum-dressed state model, I will derive the momentum-dependent total phase shift for two-body scattering interactions. The total phase shift includes both the magnetically induced scattering phase shift and the optically induced scattering phase shift. From the total phase shift, I will derive the two-body loss rate constant K_2, and momentum-dependent s-wave scattering length a_{12}.

In Chapter 3, I will discuss the experimental apparatus and the methods used to produce and image ultracold Fermi gas of ^{6}Li atoms. I will also present the design and implementation of the optical system used to demonstrate control of interactions in an ultracold gas of ^{6}Li atoms.

In Chapter 4, I will present results from my experiment that demonstrates control of scattering interactions near a Feshbach resonance using the two-field optical method. I

will show the experimental results demonstrating that the two-body scattering length can be tuned by changing the magnetic field and two optical fields. In addition, I will also show the results of the spatial control of interactions experiment, where the scattering length is made to vary as a function of the axial position of the atomic cloud. The experimental results are further compared to the theoretical prediction from the continuum-dressed state model discussed in Chapter 2.

In Chapter 5, I will present an experimental study of optically-induced loss to precisely probe the momentum-dependent interactions near a Feshbach resonance. I will demonstrate that the two-field method can be used as an effective tool to probe and investigate the momentum-dependent two-body interactions in an ultracold gas.

In Chapter 6, I will summarize the thesis and briefly present an overview of some future experiments that can be done using the two-field optical method.

CHAPTER

2

THEORY: OPTICAL CONTROL OF SCATTERING INTERACTIONS IN ULTRACOLD GASES

In this chapter, I will discuss the theory of optical control of interactions in ultracold gases. A detailed treatment of the theory of magnetic Feshbach resonances and optical control of a magnetic Feshbach resonance has been reported in a previous thesis from our group [Jag16b]. This involves the derivation of the optically induced phase shift and of the momentum averaged two-body loss rate constant K_2 using a continuum-dressed state model. I will briefly summarize the main elements of the Feshbach theory and outline the results of the continuum-dressed state model. In this chapter, I will use the continuum-dressed state model to present a detailed treatment of optical control of interactions where the molecular bound state (closed channel) is optically tuned relative to the triplet continuum (open channel) by changing the frequency of applied optical fields.

I will begin by introducing the properties and the relevant atomic states of ^{6}Li. In Sec-

tion 2.2, I will discuss the Feshbach resonances in ^{6}Li. In Section 2.2, I will discuss the Feshbach resonances in ^{6}Li. The energy level scheme for the optical control of the magnetic Feshbach resonance is presented in Section 2.3.1. In Section 2.3.2, I will review the continuum-dressed state model and outline the results of the model, which involves the evaluation of the optically induced phase shift and the momentum-averaged two-body loss rate constant K_2. In Section 2.4, I will use the continuum-dressed model to evaluate the tuning of the molecular bound state from the optically induced phase shift. I will conclude this chapter by presenting the predictions of the continuum-dressed state model that illustrates the versatility of our two-field method in creating designer spatial control of interactions in ultracold gases.

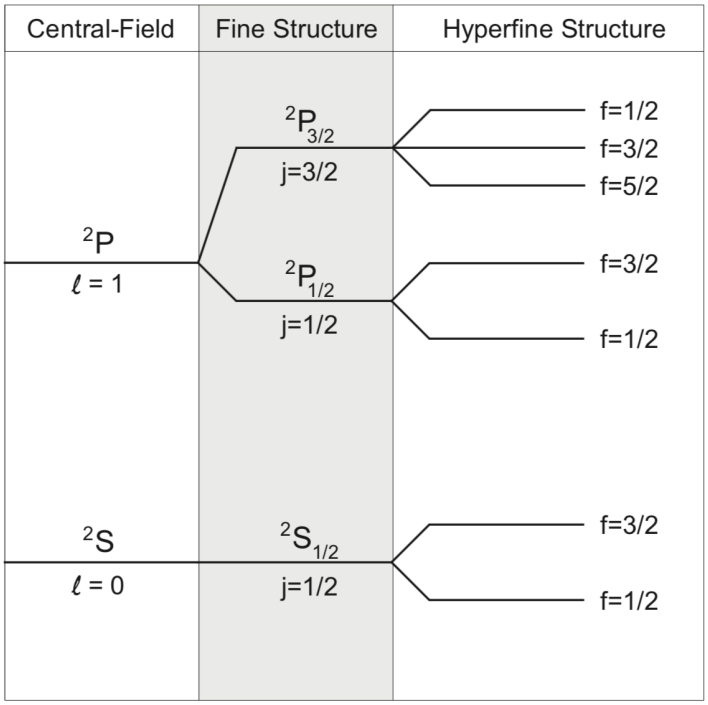

Figure 2.1 Ground (lower) and first excited (upper) states of ^{6}Li in the total orbital angular momentum **L**, total electronic angular momentum $\mathbf{J} = \mathbf{L} + \mathbf{S}$, and total angular momentum $\mathbf{F} = \mathbf{J} + \mathbf{I}$ bases, where **I** is the nuclear spin. Illustration taken from Ref [Geh03].

2.1 Properties of ^{6}Li

^{6}Li has 3 protons, 3 neutrons, and 3 electrons. Since it has a single unpaired valence electron and a nuclear spin of I = 1, ^{6}Li is a fermion. The electronic ground state of ^{6}Li has a total electronic spin angular momentum of $S = 1/2$ and total electronic orbital momentum of $L = 0$. The total angular momentum quantum number F depends on nuclear, orbital and electron spins. Hence, the total angular momentum F takes the values, $F = 1/2$ and $F = 3/2$. The ground and excited states of ^{6}Li are schematically indicated Fig. 2.1. The effect of the spin-orbit interaction is shown in the middle column. The effect of electron-nucleus interaction is shown in the right column. In this section, I will focus only on the ground state of the ^{6}Li atom.

In the absence of an external magnetic field, the $F = 1/2$ state is two-fold degenerate corresponding to $m_f = \pm 1/2$ and the $F = 3/2$ state is four-fold degenerate corresponding to $m_f = \pm 3/2, \pm 1/2$. The application of a bias magnetic field breaks this degeneracy and gives rise to six hyperfine states, conventionally labeled as $|1\rangle, |2\rangle, |3\rangle, |4\rangle, |5\rangle$, and $|6\rangle$ in the order of increasing energy.

The interaction Hamiltonian of this system is

$$H_{int} = \frac{a_{hf}}{\hbar^2}\mathbf{S}\cdot\mathbf{I} - \frac{\mu_B}{\hbar}(g_J\mathbf{S} + g_I\mathbf{I})\cdot\mathbf{B}, \tag{2.1}$$

where $a_{hf}/h = 152.137$ MHz is the magnetic dipole constant and g_J = - 2.002 is the total electronic g-factor for the ^{6}Li ground state, $g_I = 0.000448$ is the total nuclear g-factor, μ_B is the Bohr magneton, and B is the external magnetic field. By solving the energy eigenvalue problem of Eq. 2.1, the six energy eigenvalue of the hyperfine states are plotted in Fig. 2.2. To get a thorough understanding of the electronic structure of ^{6}Li, the readers are encouraged to refer to older thesis [Geh03; Kin06; Ell14] from our group.

In our laboratory, most of the experiments are done using a 50-50 mixture of the two lowest hyperfine states of ^{6}Li, namely, states $|1\rangle$ and $|2\rangle$. In the $|m_s\ m_I\rangle$ basis, where m_s is the electronic spin projection quantum number and m_I is the nuclear spin projection quantum number, the two lowest hyperfine states are,

$$|1\rangle = \sin\Theta_+|1/2\ \ 0\rangle + \cos\Theta_+|-1/2\ \ 1\rangle \tag{2.2}$$

$$|2\rangle = \sin\Theta_-|1/2\ \ -1\rangle + \cos\Theta_-|-1/2\ \ 0\rangle. \tag{2.3}$$

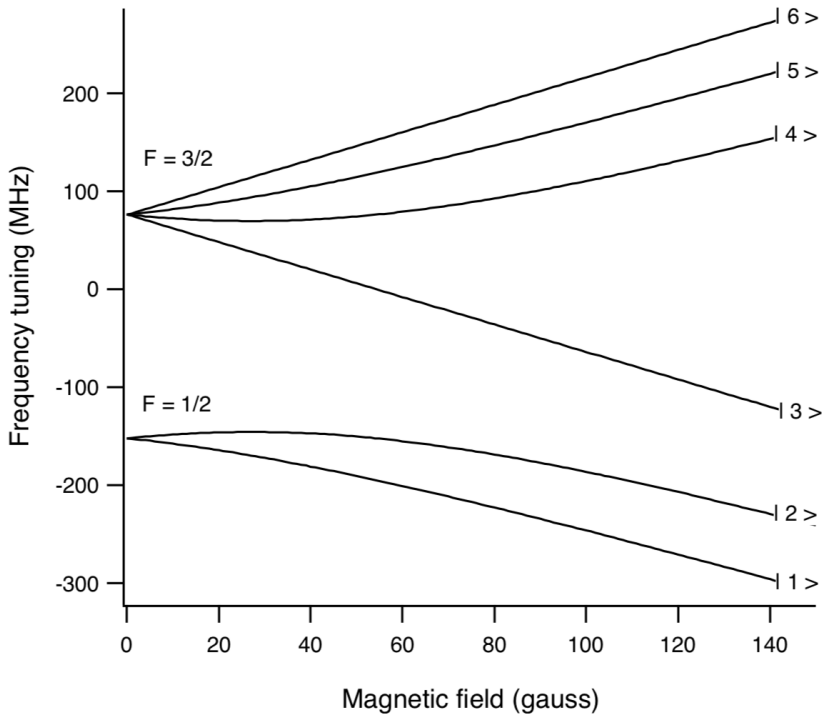

Figure 2.2 The hyperfine energy eigenvalues of the ^{6}Li ground state as a function of magnetic field. At nonzero magnetic field, there are six energy levels. The six eigenstates are labeled in order of increasing energy as $|1\rangle, |2\rangle, |3\rangle, |4\rangle, |5\rangle$, and $|6\rangle$. The total angular momentum quantum number (F = 1/2 and F = 3/2) for each of the states at zero magnetic field is labeled on the left. Illustration taken from Ref [Kin06]

The coefficients in Eq. 2.2 and Eq. 2.3 are magnetic field dependent and is given by,

$$\sin\Theta_{\pm} = \frac{1}{\sqrt{1+(Z^{\pm}+R^{\pm})^2/2}} \tag{2.4}$$

$$\cos\Theta_{\pm} = \sqrt{1-\sin^2\Theta_{\pm}} \tag{2.5}$$

$$Z^{\pm} = \frac{\mu_B B}{a_{hf}}(g_J - g_I) \pm \frac{1}{2} \tag{2.6}$$

$$R^{\pm} = \sqrt{(Z^{\pm})^2+2} \tag{2.7}$$

From Eq. 2.4 and Eq. 2.5, it is evident that at high magnetic fields, $\sin\Theta_{\pm} \rightarrow 0$ and

$\cos\Theta_{\pm} \rightarrow 1$. Hence, the atoms are predominantly in the spin triplet state at high magnetic fields.

2.2 Feshbach Resonances in ^{6}Li

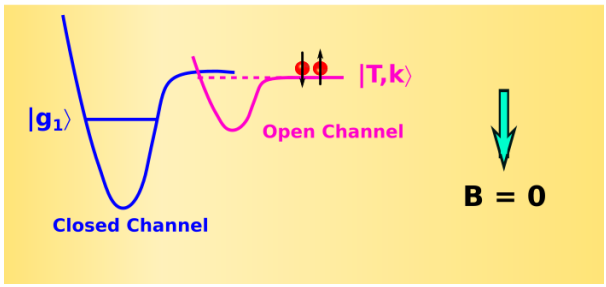

(a)

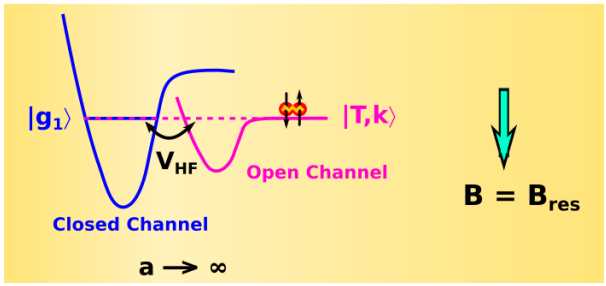

(b)

Figure 2.3 Magnetic Feshbach resonance arises due to the hyperfine coupling between the scattering continuum $|T,k\rangle$ (open channel) and the molecular bound state $|g_1\rangle$. The open channel $|T,k\rangle$ is magnetically tunable. (a) At B = 0, the triplet continuum $|T,k\rangle$ is higher in energy than the molecular bound state $|g_1\rangle$. (b) At B = B_{res}, the triplet continuum $|T,k\rangle$ is degenerate with the molecular bound state $|g_1\rangle$.

Fig. 2.3 illustrates the magnetic Feshbach resonance. The colliding atoms reside in the energetically open channel. In the Fig. 2.3, the combined energy of the colliding particles is represented by the magenta dotted line. The atoms have sufficient energy to interact via the open triplet channel $|T,k\rangle$ represented by the magenta curve, but do not have sufficient energy to interact via the singlet potential represented by the blue curve. Hence the blue curve is an energetically forbidden, closed collision channel. However, the scattering

process in the open channel can be greatly enhanced when the incoming open channel $|T,k\rangle$ is magnetically tuned to be degenerate with the bound state $|g_1\rangle$ of the closed channel. This method of inducing a collisional resonance by tuning the magnetic field is called a magnetic Feshbach resonance. In the case of ^{6}Li, the open channel is the spin triplet state. Also, the open channel is a scattering state with a continuum of states with momentum k. Hence, the open channel is labeled as $|T,k\rangle$. The resonant closed channel state is the highest lying vibrational state $|\nu=38\rangle$ of the singlet potential and it is labeled as $|g_1\rangle$.

Near a Feshbach resonance, the general form for the zero energy s-wave scattering length as a function of magnetic field B is given by [Chi10]

$$a = a_{bg} - |a_{bg}| \frac{\Delta B}{B - B_{res}}, \tag{2.8}$$

where a_{bg} is the background scattering length, ΔB is the width of the resonance, B_{res} is the resonance magnetic field, and B is the magnetic field. Eq. 2.8, shows that when $B = B_{res}$, the scattering length a diverges.

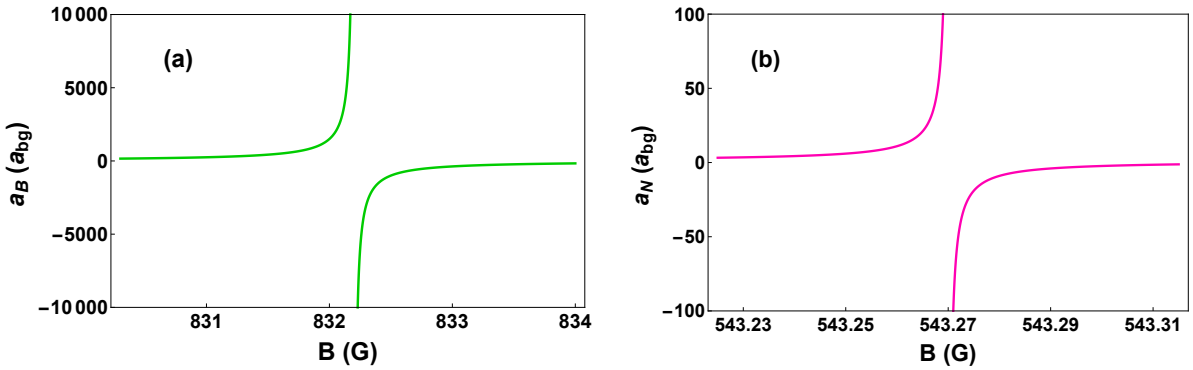

Figure 2.4 Zero energy scattering length a as a function of magnetic field B in units of background scattering length a_{bg} for (a) the broad Feshbach resonance at 832.2 G with width $\Delta B = 300$ G and (b) the narrow Feshbach resonance at 543.2 G with width $\Delta B = 0.1G$. The background scattering length a_{bg} for the broad and narrow Feshbach resonance in ^{6}Li is -1450 a_0 and 62 a_0, respectively.

The lowest two hyperfine states $|1\rangle$ and $|2\rangle$ in ^{6}Li have a broad Feshbach resonance at 832.2 G [ZÏ3] with width $\Delta B = 300$ G [Bar05] and a narrow Feshbach resonance at 543.2 G with width $\Delta B = 0.1$ G [Haz12]. The background scattering lengths a_{bg} in Eq. 2.8 for

the broad and narrow Feshbach resonances are $-1450\,a_0$ and $62\,a_0$, respectively, where a_0 is the Bohr radius. Fig. 2.4a and Fig. 2.4b shows the plot of zero momentum ($k = 0$) scattering length for broad and narrow Feshbach resonance as a function of the magnetic field, respectively. Next I will introduce the triplet and singlet states responsible for the broad and the narrow Feshbach resonance in ^{6}Li.

2.2.1 Feshbach States in ^{6}Li

For s-wave collisions of atoms in a $|1\rangle - |2\rangle$ mixture, the total magnetic quantum number $M = 0$ is conserved in a bias magnetic field B_z. In the $|S, m_s; I, m_I\rangle$ basis, there are five states for $M = 0$. Here S is the total electronic spin quantum number and I is the total nuclear spin quantum number of the two-atom system. There are two singlet states with total $M = 0$, $|0,0;0,0\rangle$ and $|0,0;2,0\rangle$ which differ in the total nuclear spin I = 0, 2. The singlet states are degenerate in the absence of hyperfine interactions. There are also three triplet states with total $M = 0$, $|1,-1;1,1\rangle$, $|1,0;1,0\rangle$, and $|1,1;1,-1\rangle$.

The triplet state $|1,1;1,-1\rangle$ tunes upward with magnetic field ($m_s = +1$) and the triplet state $|1,0;1,0\rangle$ does not tune with the magnetic field ($m_s = 0$). The only triplet state that tunes downward with increasing magnetic field is $|1,-1;1,1\rangle$ ($m_s = -1$). A magnetic Feshbach resonance occurs when the bias magnetic field tunes the total energy of a colliding atom pair in the open triplet channel *downward* into resonance with a bound molecular state in the energetically closed singlet channel. Hence,

$$|T\rangle = |1,-1;1,1\rangle \tag{2.9}$$

is the triplet state $|T\rangle$ responsible for the Feshbach resonance in ^{6}Li with the Zeeman-hyperfine energy

$$E_T = -\frac{a_{HF}}{2} - 2\mu_B B \tag{2.10}$$

where $a_{HF} = h \times 152.1$ MHz is the hyperfine coupling constant, $\mu_B = 1.4$ MHz/G is the Bohr magnetron, and B is the magnetic field. The superposition of two singlet states,

$$|g_1^n\rangle = \frac{1}{3}|0,0;0,0\rangle + \frac{2\sqrt{2}}{3}|0,0;2,0\rangle \tag{2.11}$$

is responsible for the narrow Feshbach resonance at 543.2 G [WT12a; WT12b]. The state

$|g_1^n\rangle$ does not have first order hyperfine coupling with the triplet state $|1,-1;1,1\rangle$ but has a second order coupling to $|1,-1;1,1\rangle$ through the triplet state $|1,0;1,0\rangle$. The broad Feshbach resonance at 832.2 G is due to the singlet state $|g_1^b\rangle$ that is orthogonal to $|g_1^n\rangle$ and is given by

$$|g_1^b\rangle = \frac{2\sqrt{2}}{3}|0,0;0,0\rangle - \frac{1}{3}|0,0;2,0\rangle. \tag{2.12}$$

The singlet-triplet hyperfine coupling for the broad Feshbach resonance is $V_{HF}/\hbar = 131.6$ MHz. For the narrow Feshbach resonance, the singlet-triplet states have a weak second-order hyperfine coupling of only $V_{HF}/\hbar = 5.9$ MHz arising from the $|1,0;1,0\rangle$ triplet state. With this section, I will conclude the treatment of magnetic Feshbach resonances and move forward in describing the theory of optically controlling interactions in ultracold gases.

2.3 Theory of Optically Controlling Interactions near a Magnetic Feshbach Resonance (MFR)

I will begin this section by introducing the basic level scheme for two-field optical control of interactions in ^{6}Li. I will then proceed to describe the continuum-dressed state model reported in Ref [Jag16a] and outline the relevant results such as the evaluation of the optically induced phase shift and the momentum-averaged two-body loss rate constant K_2.

2.3.1 Energy Level Scheme for Two-field Optical Control of MFR in ^{6}Li

The energy level scheme for the two-field optical control of magnetic Feshbach resonance is shown in Fig. 2.5 [Jag16a]. The unbound incoming atoms are in the triplet $|T,k\rangle$ state of the ground triplet potential $^3\Sigma_u^+$. In a magnetic field B, the triplet continuum $|T,k\rangle$ tunes downward and the tuning rate is proportional to $2\mu_B B$, where μ_B is the Bohr magneton, $\mu_B/h \simeq h \times 1.4$ MHz/G. The hyperfine coupling V_{HF} between $|T,k\rangle$ and $|g_1\rangle$ produces a Feshbach resonance.

To optically control the magnetic Feshbach resonance, two optical fields are used. The optical field with Rabi frequency Ω_1 and frequency ν_1 couples the ground vibrational state $|g_1\rangle$ of the singlet potential $^1\Sigma_g^+$ to the excited vibrational state $|e\rangle$ of the singlet potential $^1\Sigma_u^+$. A second optical field with Rabi frequency Ω_2 and frequency ν_2 couples another ground vibrational state $|g_2\rangle$ of the same singlet potential $^1\Sigma_g^+$ to the excited vibrational state $|e\rangle$.

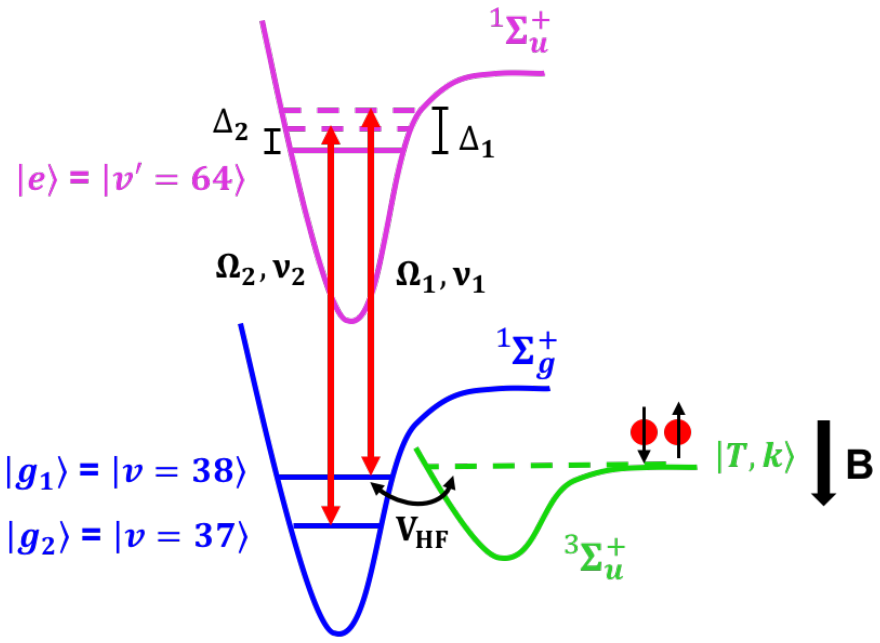

Figure 2.5 Basic level scheme for controlling interactions in ^{6}Li. Optical fields ν_1 (with Rabi frequency Ω_1 and detuning Δ_1) and ν_2 (with Rabi frequency Ω_2 and and detuning Δ_2) couple the ground molecular states $|g_1\rangle$ and $|g_2\rangle$ to the excited molecular state $|e\rangle$ of the singlet potential. The atoms are predominantly in the triplet state $|T,k\rangle$ which has an hyperfine coupling V_{HF} to state $|g_1\rangle$ causing the Feshbach resonance. The triplet state moves downward with increasing magnetic field B. For the optical control experiments in ^{6}Li, $|g_1\rangle = |v = 38\rangle$, $|g_2\rangle = |v = 37\rangle$, and $|e\rangle = |v' = 64\rangle$.

Application of ν_1 beam creates a light shift of state $|g_1\rangle$ due to AC stark effect. When the shifted $|g_1\rangle$ state is degenerate with the triplet continuum $|T,k\rangle$, it leads to atom loss. Atom loss occurs due to photoassociation of atoms from the triplet continuum $|T,k\rangle$ to the excited singlet state $|e\rangle$ due to the hyperfine coupling of $|T,k\rangle$ to state $|g_1\rangle$. Note that in the absence of a Feshbach resonance, an optical transition from the incoming spin triplet state $|T,k\rangle$ to the excited spin singlet vibrational state $|e\rangle$ is strictly forbidden. Therefore, far from the Feshbach resonance, there is no atom loss. The ν_2 beam suppresses atom loss through destructive quantum interference. For our experiments with ^{6}Li, $|g_1\rangle$ and $|g_2\rangle$ are the $v = 38$ and $v = 37$ ground vibrational states and $|e\rangle$ is the $v' = 64$ excited vibrational state, which decays at a rate $\gamma_e = 2\pi \times 11.8$ MHz.

2.3.2 Continuum-dressed State Model for Two-field Optical Control of MFR

The continuum-dressed state model is explained in detail in the previous thesis [Jag16b]. In this section, I will briefly summarize the relevant results of this model. Fig. 2.6a and Fig. 2.6b shows the level scheme for bare state and continuum-dressed-state treatment of the Feshbach problem, respectively.

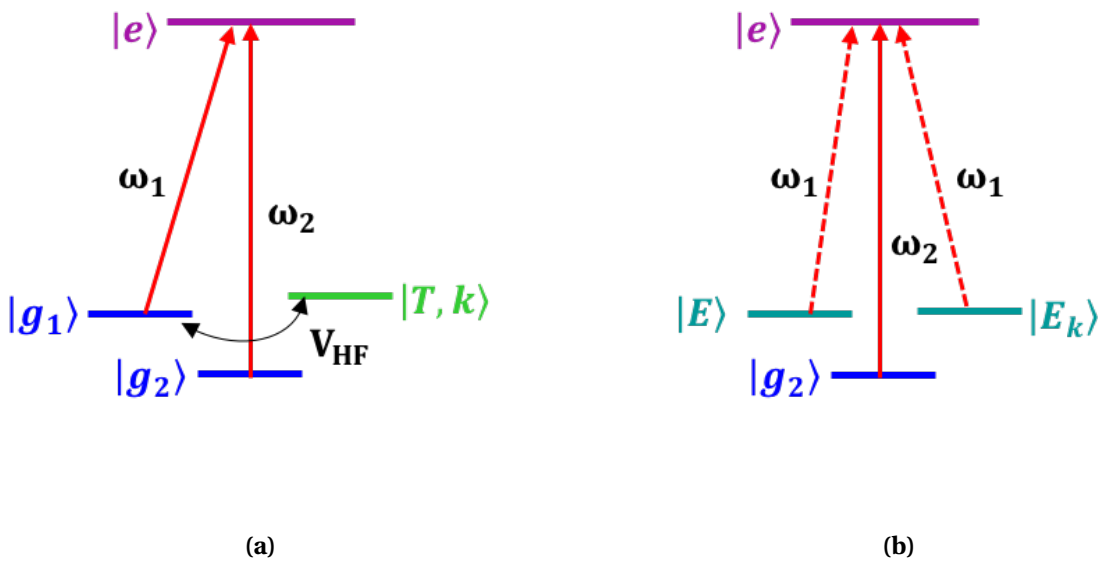

Figure 2.6 Energy level schemes in (a) “bare-state" and (b) “continuum-dressed-state" basis. $|T,k\rangle$ is a bare continuum state in the triplet (open) channel. $|g_1\rangle$, $|g_2\rangle$, and $|e\rangle$ are the bare molecular states in the singlet (closed) channel. The hyperfine interaction V_{HF} between the bare molecular state $|g_1\rangle$ and the continuum states $|T,k\rangle$, creates the dressed bound state $|E\rangle$ and the dressed scattering state $|E_k\rangle$. Illustration taken from Ref [Jag16a]

In the bare state description Fig. 2.6a, the bare states $|g_1\rangle$ and $|T,k\rangle$ have a hyperfine coupling V_{HF} and the states $|g_1\rangle$, $|g_2\rangle$ are optically coupled to state $|e\rangle$. In the continuum-dressed state model, the hyperfine coupling between the states $|g_1\rangle$ and $|T,k\rangle$ is treated first. This results in the dressing of the bound state $|g_1\rangle$ by the triplet continuum $|T,k\rangle$, leading to two dressed states, the dressed bound state $|E\rangle$ and the dressed-continuum state $|E_k\rangle$

which are superposition of the states $|g_1\rangle$ and $|T,k\rangle$. Both the dressed bound state $|E\rangle$ and the dressed-continuum state $|E_k\rangle$ contain singlet $|g_1\rangle$ contributions. Hence the optical field with frequency ν_1 couples the dressed-bound state $|E\rangle$ and the dressed-continuum state $|E_k\rangle$ to the singlet excited state $|e\rangle$, Fig. 2.6b.

I will begin by summarizing the derivation of the optically induced phase shift using the continuum-dressed state model. The unperturbed Hamiltonian of the four-level system without the optical beams in the continuum-dressed state basis can be written as,

$$H_0 = E|E\rangle\langle E| + E_{g_2}|g_2\rangle\langle g_2| + E_e|e\rangle\langle e| + \sum_{all\,k'} E_{k'}|E_{k'}\rangle\langle E_{k'}|, \tag{2.13}$$

where $|E_{k'}\rangle$ is an atom pair dressed continuum scattering state, $|E\rangle$ is the dressed bound state due to the coupling of the bare bound singlet Feshbach state $|g_1\rangle$ with the bare triplet continuum scattering states $|T,k'\rangle$, $|g_2\rangle$ is a lower lying bound singlet state that has no coupling to $|T,k'\rangle$, and $|e\rangle$ is the singlet excited state.

The optical fields are treated as the perturbation. The interaction Hamiltonian in the rotating wave approximation is

$$H'_{opt} = -\frac{\hbar\Omega_1}{2}\, e^{-i\omega_1 t}|e\rangle\langle g_1| - \frac{\hbar\Omega_2}{2}\, e^{-i\omega_2 t}|e\rangle\langle g_2| + h.c., \tag{2.14}$$

where Ω_1 and ω_1 are the Rabi and angular frequencies of the optical field that couples $|g_1\rangle$ to $|e\rangle$, and Ω_2 and ω_2 are the Rabi and angular frequencies of the optical field that couples $|g_2\rangle$ to $|e\rangle$, respectively.

When $H'_{opt} = 0$, $|E_k\rangle$ is the *input* scattering Feshbach resonance state. When $H'_{opt} \neq 0$, the time-dependent scattering state is given by,

$$|\psi_{E_k}(t)\rangle = c_E(t)|E\rangle + c_2(t)|g_2\rangle + c_e(t)|e\rangle + c(k,t)|E_k\rangle + \sum_{k'\neq k} c(k',t)|E_{k'}\rangle, \tag{2.15}$$

where $c(k,t)$ is the amplitude for the input Feshbach resonance scattering state $|E_k\rangle$. $|\psi_{E_k}(t)\rangle$ satisfies the time-dependent Schrödinger equation,

$$(H_o + H'_{opt})|\psi_{E_k}(t)\rangle = i\hbar\,\partial_t|\psi_{E_k}(t)\rangle. \tag{2.16}$$

Solving for the coefficients in Eq. 2.15, by taking the projections with $|E\rangle$, $|g_2\rangle$, $|E_{k'}\rangle$, and $|e\rangle$ on Eq. 2.16 gives,

$$
\begin{aligned}
i\hbar\,\dot{c}_E &= \langle E|(H_o+H'_{opt})|\psi_{E_k}(t)\rangle = E\,c_E+\langle E|H'_{opt}|\psi_{E_k}(t)\rangle,\\
i\hbar\,\dot{c}_E &= E\,c_E-\frac{\hbar\Omega_1^*}{2}\,e^{i\omega_1 t}\langle E|g_1\rangle\,c_e. &(2.17)\\
i\hbar\,\dot{c}_2 &= E_{g_2}\,c_2-\frac{\hbar\Omega_2^*}{2}\,e^{i\omega_2 t}\langle E|g_1\rangle\,c_e, &(2.18)\\
i\hbar\,\dot{c}(k') &= E_{k'}\,c(k')-\frac{\hbar\Omega_1^*}{2}\,e^{i\omega_1 t}\langle E_{k'}|g_1\rangle\,c_e, &(2.19)\\
i\hbar\,\dot{c}_e &= E_e\,c_e-\frac{\hbar\Omega_1}{2}\,e^{-i\omega_1 t}\left[\langle g_1|E\rangle\,c_E+\sum_{\text{all }k'}\langle g_1|E_{k'}\rangle c(k')\right]\\
&- \frac{\hbar\Omega_2}{2}\,e^{-i\omega_2 t}\,c_2-i\frac{\hbar\gamma_e}{2}\,c_e. &(2.20)
\end{aligned}
$$

In Eq. 2.20 to account for the radiative decay of the excited state to the ground vibrational manifold, a decay term $-\gamma_e\,c_e/2$ is added. To eliminate the time-dependent phase factors from Eq. 2.17 to Eq. 2.20, taking the input state to be $|E_k\rangle$ and for all k' yields,

$$
\begin{aligned}
c(k',t) &= b(k')\,e^{(-iE_k t/\hbar)}\\
c_e &= b_e\,e^{[-i(\omega_1+E_k/\hbar)t]}\\
c_E &= b_E\,e^{(-iE_k t/\hbar)}\\
c_2 &= b_2\,e^{[i(\omega_2-\omega_1-E_k/\hbar)t]}. &(2.21)
\end{aligned}
$$

Substituting Eq. 2.21 in Eq. 2.17 - Eq. 2.20 gives,

$$
\begin{aligned}
i\hbar\,\dot{b}(k') &= (E_{k'}-E_k)\,b(k')-\frac{\hbar\Omega_1^*}{2}\,\langle E_{k'}|g_1\rangle\,b_e. &(2.22)\\
i\hbar\,\dot{b}_e &= (E_e-E_k-\hbar\omega_1)\,b_e-i\frac{\hbar\gamma_e}{2}\,b_e-\frac{\hbar\Omega_2}{2}b_2\\
&- \frac{\hbar\Omega_1}{2}\left[\langle g_1|E\rangle\,b_E+\sum_{\text{all }k'}\langle g_1|E_{k'}\rangle b(k')\right]. &(2.23)\\
i\hbar\,\dot{b}_E &= (E-E_k)\,b_E-\frac{\hbar\Omega_1^*}{2}\,\langle E|g_1\rangle\,b_e &(2.24)\\
i\hbar\,\dot{b}_2 &= [E_{g_2}-E_k-\hbar(\omega_1-\omega_2)]\,b_2-\frac{\hbar\Omega_2^*}{2}\,b_e &(2.25)
\end{aligned}
$$

Assuming that the Rabi frequencies are not large compared to the optical detunings and the excited state decay rate is negligible, the excited state is adiabatically eliminated by using $\dot{b}_e = 0$ in Eq. 2.23. Solving for b_e, b_E, b_2 in terms of input state amplitude $b(k)$ yields

$$b_e = \frac{\hbar\Omega_1}{2}\frac{\langle g_1|E_k\rangle|}{D(E,E_k)}\,b(k), \tag{2.26}$$

$$b_E = \left|\frac{\hbar\Omega_1}{2}\right|^2 \frac{\langle E|g_1\rangle\langle g_1|E_k\rangle}{(E-E_k)D(E,E_k)}\,b(k), \tag{2.27}$$

$$b\,(k'\neq k) = \left|\frac{\hbar\Omega_1}{2}\right|^2 \frac{\langle E_{k'}|g_1\rangle\langle g_1|E_k\rangle}{(E_{k'}-E_k)D(E,E_k)}\,b(k), \tag{2.28}$$

$$\dot{b}(k) = \frac{i\hbar\,|\Omega_1|^2}{4}\frac{|\langle g_1|E_k\rangle|^2}{D(E,E_k)}\,b(k), \tag{2.29}$$

where the energy denominator $D(E,E_k)$ is given by

$$\begin{aligned} D(E,E_k) &= E_e - E_k - \hbar\omega_1 - i\hbar\frac{\gamma_e}{2} - \left|\frac{\hbar\Omega_1}{2}\right|^2\left\{\frac{|\langle g_1|E\rangle|^2}{E-E_k} + \sum_{k'\neq k}\frac{|\langle g_1|E_{k'}\rangle|^2}{E_{k'}-E_k}\right\} \\ &- \left|\frac{\hbar\Omega_2}{2}\right|^2\frac{1}{E_{g_2}-E_k-\hbar(\omega_1-\omega_2)}. \end{aligned} \tag{2.30}$$

Note that the energy denominator $D(E,E_k)$ has the overlap integral $\langle g_1|E\rangle$ of the bound state $|g_1\rangle$ with the dressed bound state $|E\rangle$ and the overlap integral $\langle g_1|E_k\rangle$ of the bound state $|g_1\rangle$ with the dressed continuum state $|E_k\rangle$. Although $D(E,E_k)$ in Eq. 2.30 looks overly complicated, it can be simplified by making the proper substitutions.

The first stage of simplifying $D(E,E_k)$ in Eq. 2.30 involves defining the appropriate detunings and replacing the energy terms in $D(E,E_k)$ in terms of optical detunings. For the level scheme shown in Fig. 2.6b, the single photon detuning $\Delta_e(k)$ for the $|T\rangle - |e\rangle$ transition is defined to be,

$$\Delta_e(k) \equiv \omega_1 - \frac{E_e - E_k}{\hbar}, \tag{2.31}$$

and the two-photon detuning for the $|g_2\rangle - |T\rangle - |e\rangle$ transition as

$$\delta(k) \equiv \omega_2 - \omega_1 - \frac{E_k - E_{g_2}}{\hbar}, \tag{2.32}$$

where the energy E_k and E_T is given by

$$E_k = E_T + \frac{\hbar^2 k^2}{m} \qquad \text{and} \qquad E_T = -\frac{a_{HF}}{2} - 2\mu_B B. \tag{2.33}$$

Redefining Eq. 2.30 in terms of $\Delta_e(k)$ and $\delta(k)$ in Eq. 2.31 and Eq. 2.32 gives

$$\frac{D(E, E_k)}{\hbar} = -\Delta_e(k) - \frac{\Omega_2^2}{4\,\delta(k)} - \frac{\Omega_1^2}{4}\,\frac{\hbar}{2\,\mu_B\,\Delta B}\,(\tilde{I}_{E_k} - \tilde{I}_E) - i\,\frac{\gamma_e}{2}, \tag{2.34}$$

where the overlap integrals $\tilde{I}_E$ and $\tilde{I}_{E_k}$ is written as

$$\tilde{I}_E \equiv 2\,\mu_B\,\Delta B\,\frac{|\langle g_1|E\rangle|^2}{E_k - E}, \tag{2.35}$$

$$\tilde{I}_{E_k} \equiv 2\,\mu_B\,\Delta B \sum_{k' \neq k} \frac{|\langle g_1|E_{k'}\rangle|^2}{E_{k'} - E_k}. \tag{2.36}$$

The second stage of simplifying the energy denominator involves the evaluation of the term $\tilde{I}_{E_k} - \tilde{I}_E$ using the complete form of the states $|E\rangle$ and $|E_{k'}\rangle$. However, this term has to be evaluated separately for the broad and the narrow Feshbach resonance. For the broad Feshbach resonance, this term yields [Jag16b]

$$S_B(\tilde{\Delta}_0, x) \equiv \tilde{I}_{E_k} - \tilde{I}_E = \frac{\tilde{\Delta}_0 + (1 + \tilde{\Delta}_0)x^2}{\tilde{\Delta}_0^2 + (1 + \tilde{\Delta}_0)^2 x^2} \tag{2.37}$$

and for the narrow Feshbach resonance,

$$S_N(\tilde{\Delta}_0, x) \equiv \tilde{I}_{E_k} - \tilde{I}_E = \frac{1}{\tilde{\Delta}_0 - \epsilon\, x^2} \tag{2.38}$$

where, $\tilde{\Delta}_0 = (B - B_{res})/\Delta B$. Using Eq. 2.37 and Eq. 2.38 in Eq. 2.34, the final simplified expressions of the energy denominator are obtained. For the broad Feshbach resonance,

$$\frac{D_B(E,E_k)}{\hbar} = -\Delta_e(k) - \frac{\Omega_2^2}{4\,\delta(k)} - \frac{\Omega_1^2}{4}\,\frac{\hbar}{2\,\mu_B\,\Delta B}\left(\frac{\tilde{\Delta}_0 + (1+\tilde{\Delta}_0)x^2}{\tilde{\Delta}_0^2 + (1+\tilde{\Delta}_0)^2 x^2}\right) - i\,\frac{\gamma_e}{2}, \tag{2.39}$$

and for the narrow Feshbach resonance,

$$\frac{D_N(E,E_k)}{\hbar} = -\Delta_e(k) - \frac{\Omega_2^2}{4\,\delta(k)} - \frac{\Omega_1^2}{4}\,\frac{\hbar}{2\,\mu_B\,\Delta B}\left(\frac{1}{\tilde{\Delta}_0 - \epsilon\,x^2}\right) - i\,\frac{\gamma_e}{2}. \tag{2.40}$$

For convenience, I will further define the single (Eq. 2.31)and two-photon (Eq. 2.32) detunings in terms of laser detuning Δ_1 for the $|g_1\rangle - |e\rangle$ transition and laser detuning Δ_2 for the $|g_2\rangle - |e\rangle$ transition as

$$\Delta_e(k) = \Delta_1 - \frac{2\mu_B(B - B_{ref})}{\hbar} + \frac{\hbar k^2}{m} \tag{2.41}$$

$$\delta(k) = \Delta_2 - \Delta_1 + \frac{2\mu_B(B - B_{ref})}{\hbar} - \frac{\hbar k^2}{m} \tag{2.42}$$

where the laser detuning Δ_1 and Δ_2 are given by

$$\Delta_1 \equiv \omega_1 - \frac{E_e - E_{g_1}}{\hbar} \tag{2.43}$$

$$\Delta_2 \equiv \omega_2 - \frac{E_e - E_{g_2}}{\hbar} \tag{2.44}$$

2.3.3 Scattering State Wave Function

I will now proceed to evaluate the scattering state wave function from which the optically induced phase shift can be determined. At $r \to \infty$, only the triplet part of the wave function contributes to the scattering state i.e. for the bound states, $\langle r|e\rangle = 0$, $\langle r|g_2\rangle = 0$, and $\langle r|E\rangle = 0$ as $r \to \infty$. Taking the projection of $|r\rangle$ on Eq. 2.15 and writing the state in terms of b_k and $b_{k'}$,

$$\langle r\to\infty|\Psi_{E_k}\rangle=\Psi_{E_k}(r\to\infty)=b(k)\langle r\to\infty|E_k\rangle+\sum_{k'\neq k}b(k')\langle r\to\infty|E_{k'}\rangle. \tag{2.45}$$

The asymptotic form of the dressed continuum state wave function for box normalization as $r\to\infty$ is given by,

$$\langle r\to\infty|E_{k'}\rangle \;=\; \frac{1}{\sqrt{V}}\frac{[\sin[k'r+\Delta(k')]]}{k'r}, \tag{2.46}$$

where the factor $1/\sqrt{V}$ is needed for box normalization, and $\Delta(k')$ is the phase shift induced due to the Feshbach resonance. $\Delta(k')$ is written as the sum of the resonant part of the phase shift $\tilde{\Delta}(k')$ and the background part of the phase shift $\delta_{bg}(k')$.

$$\Delta(k') \;=\; \tilde{\Delta}(k')+\delta_{bg}(k'). \tag{2.47}$$

Substituting Eq. 2.28 and Eq. 2.46 in Eq. 2.45 yield,

$$\begin{aligned}\Psi_{E_k}(r\to\infty) \;&=\; \frac{b(k)}{kr\sqrt{V}}\Bigg[\sin[kr+\Delta(k)] \\ &\quad+\sum_{k'\neq k}\frac{\hbar^2|\Omega_1^2|}{4}\frac{\langle E_{k'}|g_1\rangle\langle g_1|E_k\rangle}{(E_{k'}-E_k)\,D(E,E_k)}\frac{k}{k'}\sin[k'r+\Delta(k)]\Bigg].\end{aligned} \tag{2.48}$$

Evaluating the summation in the second term as the principal part of a complex integral gives,

$$\Psi_{E_k}(r\to\infty)=\frac{b(k)}{kr\sqrt{V}}\left[\sin[kr+\Delta(k)]+\frac{\Omega_1^2}{4}\frac{2\pi^2 mk|\langle g_1|\tilde{E}_k\rangle|^2}{D(E,E_k)}\cos[kr+\Delta(k)]\right], \tag{2.49}$$

where $D(E,E_k)$ for the broad and the narrow Feshbach resonance is given in Eq. 2.39 and Eq. 2.40, respectively.

2.3.4 Evaluation of the Optically Induced Phase Shift ϕ

From the scattering state wave function, I now evaluate the optically induced phase shift. To satisfy the condition for box-normalization of the input state, the output triplet scattering

state, Eq. 2.49, must have the form

$$\Psi_{E_k}(r\to\infty) = \frac{1}{\sqrt{V}}\frac{[\sin(kr+\Delta(k)+\phi(k)]}{kr}, \tag{2.50}$$

where $\Delta(k)$ is phase shift induced by the magnetic Feshbach resonance, $\phi(k)$ is the light-induced phase shift, and the total phase shift $\delta(k)\equiv\Delta(k)+\phi(k)$.

Expanding Eq. 2.50,

$$\Psi_{E_k}(r\to\infty)=\frac{1}{\sqrt{V}kr}[\sin(kr+\Delta(k))\cos(\phi(k))+\cos(kr+\Delta(k))\sin(\phi(k))] \tag{2.51}$$

Comparing Eq. 2.51 with Eq. 2.49,

$$k\cot[\phi(k)] = \frac{D(E,E_k)}{\frac{\Omega_1^2}{4}2\pi^2 m|\langle g_1|\tilde{E}_k\rangle|^2} \tag{2.52}$$

Using $x=k|a_{bg}|$ in the above equation purely for the purpose of convenience in evaluating the momentum integrals later gives,

$$x\cot[\phi(k)] = \frac{D(E,E_k)|a_{bg}|}{\frac{\Omega_1^2}{4}2\pi^2 m|\langle g_1|\tilde{E}_k\rangle|^2} \tag{2.53}$$

Here

$$\begin{aligned}|\langle g_1|\tilde{E}_k\rangle|^2 &= \frac{\epsilon|a_{bg}|^3}{2\pi^2}\frac{1}{[\tilde{\Delta}_0-\epsilon\,x^2]^2+x^2[1+\tilde{\Delta}_0-\epsilon\,x^2]^2}, \\ &= \frac{\epsilon|a_{bg}|^3}{2\pi^2}L(\tilde{\Delta}_0,x),\end{aligned} \tag{2.54}$$

where

$$L(\tilde{\Delta}_0, x) = \frac{1}{[\tilde{\Delta}_0 - \epsilon\, x^2]^2 + x^2\,[1 + \tilde{\Delta}_0 - \epsilon\, x^2]^2}. \tag{2.55}$$

$$\tilde{\Delta}_0 = \frac{B - B_\infty}{\Delta B},$$

$$\epsilon = \frac{E_{bg}}{2\mu_B \Delta B},$$

$$E_{bg} = \frac{\hbar^2}{m a_{bg}^2}. \tag{2.56}$$

Substituting Eq. 2.39 and Eq. 2.54 in Eq. 2.53, the optically induced phase shift $\phi_B(x)$ for the *broad* Feshbach resonance is

$$x \cot[\phi_B(x)] = -\frac{\tilde{\Delta}_e(x) + \frac{\tilde{\Omega}_2^2}{4\,\tilde{\delta}(x)} + \frac{\tilde{\Omega}_1^2}{4}\,\frac{\hbar\gamma_e}{2\mu_B \Delta B}\left(\frac{\tilde{\Delta}_0 + (1+\tilde{\Delta}_0)x^2}{\tilde{\Delta}_0^2 + (1+\tilde{\Delta}_0)^2 x^2}\right) + \frac{i}{2}}{\frac{\tilde{\Omega}_1^2}{4}\,\frac{\hbar\gamma_e}{2\mu_B \Delta B}\, L(\tilde{\Delta}_0, x)}, \tag{2.57}$$

and substituting Eq. 2.40 and Eq. 2.54 in Eq. 2.53, the optically induced phase shift $\phi_N(x)$ for the *narrow* Feshbach resonance is

$$x \cot[\phi_N(x)] = -\frac{\tilde{\Delta}_e(x) + \frac{\tilde{\Omega}_2^2}{4\,\tilde{\delta}(x)} + \frac{\tilde{\Omega}_1^2}{4}\,\frac{\hbar\gamma_e}{2\mu_B \Delta B}\left(\frac{1}{\tilde{\Delta}_0 - \epsilon x^2}\right) + \frac{i}{2}}{\frac{\tilde{\Omega}_1^2}{4}\,\frac{\hbar\gamma_e}{2\mu_B \Delta B}\, L(\tilde{\Delta}_0, x)}. \tag{2.58}$$

In Eq. 2.57 and Eq. 2.58, the dimensionless frequencies are defined as

$$\tilde{\delta}(x) = \frac{\delta(x)}{\gamma_e};\quad \tilde{\Delta}_e(x) = \frac{\Delta_e(x)}{\gamma_e};\quad \tilde{\Omega}_2 = \frac{\Omega_2}{\gamma_e};\quad \tilde{\Omega}_1 = \frac{\Omega_1}{\gamma_e}.$$

Eq. 2.57 and Eq. 2.58 gives the optically induced change in the scattering phase shifts for broad and narrow Feshbach resonance in terms of experimental parameters. Using Eq. 2.57 and Eq. 2.58, the optically controlled two-body loss rates and the zero-energy scattering lengths can be calculated.

2.3.5 Evaluation of the Total Phase Shift δ

The next step is to evaluate the total phase shift δ. The total phase shift δ is the sum of the Feshbach resonance phase shift Δ without the optical fields and the light induced phase

shift ϕ,

$$\delta(k) \equiv \Delta(k) + \phi(k). \tag{2.59}$$

From Eq. 2.59 and $\cot\delta = \frac{\cos\delta}{\sin\delta}$,

$$k\cot\delta = \frac{k\cot\Delta\, k\cot\phi - k^2}{k\cot\Delta + k\cot\phi} \tag{2.60}$$

Using $x = k|a_{bg}|$ in the above equation,

$$x\cot\delta = \frac{x\cot\Delta\, x\cot\phi - x^2}{x\cot\Delta + x\cot\phi}, \tag{2.61}$$

where the phase shift Δ induced by the magnetic Feshbach resonance can be written as [Jag16b]

$$x\cot\Delta = \frac{\tilde{\Delta}_0 - \epsilon x^2}{1 + \tilde{\Delta}_0 - \epsilon x^2}. \tag{2.62}$$

The phase shift ϕ is given by Eq. 2.57 or Eq. 2.58.

2.3.6 Two-body Loss Rate Constant K_2 and Scattering Length a

In two-body scattering, the relative momentum-dependent two-body scattering amplitude is given by

$$f(k) = \frac{1}{2ik}(e^{2i\delta} - 1) = \frac{1}{k\cot\delta(k) - ik}. \tag{2.63}$$

where $\delta(k)$ is the total phase shift evaluated in Eq. 2.61. In this section, I will evaluate the two-body scattering length and the loss rate constant from the two-body scattering amplitude $f(k)$.

In a scattering problem between two particles with density n_a and n_b, the optically induced loss is defined by the two-body loss rate constant K_2,

$$\dot{n}_a = -(K_2 n_b) n_a \tag{2.64}$$

The two-body loss rate K_2 can be expressed as

$$K_2(k) = v_{rel}\,\sigma_{inelastic} = \frac{\hbar k}{\mu}\sigma_{inelastic}, \tag{2.65}$$

where v_{rel} is the relative velocity between the two particles, μ is the reduced mass, and $\sigma_{inelastic}$ is the inelastic cross section.

In order to determine K_2 in Eq. 2.65, the inelastic cross-section $\sigma_{inelastic}$ has to be evaluated. I will now proceed to evaluate the inelastic cross-section $\sigma_{inelastic}$ using the elastic $\sigma_{elastic}$ cross-section and the total σ_{total} cross-section. The elastic cross section $\sigma_{elastic}$ is given by,

$$\sigma_{elastic} = 4\pi|f(k)|^2. \tag{2.66}$$

From the optical theorem, the total cross section σ_{tot} is given by

$$\sigma_{total} = \frac{4\pi}{k} Im(f(k)). \tag{2.67}$$

Using Eq. 2.66 and Eq. 2.67, rewriting the inelastic cross section

$$\begin{aligned} \sigma_{inelastic} &= \sigma_{total} - \sigma_{elastic} \\ \sigma_{inelastic} &= \frac{4\pi}{k} Im(f(k)) - 4\pi|f(k)|^2. \end{aligned} \tag{2.68}$$

It is convenient to define

$$k\cot\delta(k) \equiv q'(k) + iq''(k) \tag{2.69}$$

and evaluating $q'(k)$ and $q''(k)$ from Eq. 2.61. Substituting Eq. 2.69 in Eq. 2.63,

$$f(k) = \frac{1}{q'(k) - i[k - q''(k)]}. \tag{2.70}$$

Using Eq. 2.70 in Eq. 2.71 yields

$$\sigma_{inelastic} = -\frac{4\pi}{k}\frac{q''(k)}{[q'(k)]^2 + [x - q''(k)]^2}. \tag{2.71}$$

Substituting Eq. 2.71 in Eq. 2.65 with $\mu = m/2$, gives

$$K_2(k) = -\frac{8\pi\hbar}{m}\frac{q''(k)}{[q'(k)]^2+[k-q''(k)]^2}. \tag{2.72}$$

Eq. 2.72 is the momentum-dependent two-body loss rate constant K_2. The relative momentum averaged two-body loss rate constant is determined by assuming a Boltzmann distribution for relative momentum between atoms. Therefore, the relative momentum averaged two-body loss rate constant $\overline{K_2}$ is given by

$$\overline{K_2}(k) = \int_0^\infty \frac{4\pi k^2 dk}{(k_0\sqrt{\pi})^3}\, e^{-\frac{k^2}{k_0^2}}\, K_2(k) \tag{2.73}$$

where $(\hbar k_0)^2 = 2\mu k_B T = m k_B T$.

The momentum-dependent two-body scattering length is the negative of the real part of the scattering amplitude given in Eq. 2.63.

$$a(k) = -Re(f(k)) \tag{2.74}$$

Using Eq. 2.70, the real part of the scattering amplitude is written as

$$\mathrm{Re}[f(k)] = \frac{q'(k)}{[q'(k)]^2+[q''(k)-k]^2}. \tag{2.75}$$

Substituting, Eq. 2.75 in Eq. 2.74 yields,

$$a(k) = -\frac{q'(k)}{[q'(k)]^2+[q''(k)-k]^2} \tag{2.76}$$

Eq. 2.76 gives the relative momentum-dependent scattering length in terms of the real and imaginary part of $k\cot\delta(k)$ for the total phase shift $\delta(k)$. Assuming a Boltzmann distribution for relative momentum of atoms, the momentum-averaged two-body scattering length $\overline{a}(k)$ is then

$$\overline{a}(k) = \int_0^\infty \frac{4\pi k^2 dk}{(k_0\sqrt{\pi})^3}\, e^{-\frac{k^2}{k_0^2}}\, a(k), \tag{2.77}$$

where $(\hbar k_0)^2 = 2\mu k_B T = m k_B T$.

Using the effective range expansion, the optical and magnetic parts of the scattering length can be extracted from the optically induced phase shift in Eq. 2.58 and the magnetically induced phase shift in Eq. 2.62. Writing the effective range expansion for the optically induced phase shift gives,

$$x \cot \phi(x) = -\frac{1}{a_{opt}} + \frac{k^2 \, r_{opt}}{2} \tag{2.78}$$

where a_{opt} is the optical part of the scattering length and r_{opt} is the optical part of the effective range. Comparing Eq. 2.78 with Eq. 2.52 yields

$$a_{opt} = |a_{bg}| \frac{\frac{\Omega_1^2}{4} 2\pi^2 m |\langle g_1 | \tilde{E}_k \rangle|^2}{D(E, E_k)}. \tag{2.79}$$

Similarly, writing the effective range expansion for the phase shift induced by the magnetic Feshbach resonance in Eq. 2.58 and extracting the scattering length a_F for the magnetic Feshbach resonance gives the expected result,

$$a_F = a_{bg} \frac{1 + \tilde{\Delta}_0}{\tilde{\Delta}_0} = a_{bg} \left(1 - \frac{\Delta B}{B - B_{res}} \right). \tag{2.80}$$

2.4 Optical Tuning of Ground State $|g_1\rangle$

In the last section, the continuum-dressed model was used to calculate the optically induced phase shift in the scattering wave function of the atoms near a magnetic Feshbach resonance and in the presence of optical fields. One of the main advantages of this model is that it allows us to determine the rate at which the ground state $|g_1\rangle$ tunes as a function of the optical control parameters such as the Rabi frequency and the frequency of the optical beams. The tuning rate of $|g_1\rangle$ can be extracted from the energy denominator derived in Eq. 2.39 and Eq. 2.40 for the case of broad and narrow Feshbach resonances, respectively. Since all the experiments reported in this thesis involved working near the narrow Feshbach resonance, I will predict the tuning of ground state $|g_1\rangle$ near the narrow Feshbach resonance.

Alternatively, the energy of state $|g_1\rangle$ in a simple three-level Λ EIT system can be determined by solving the dressed state problem in the atom-field basis. In this section, I will demonstrate that the tuning rate determined by finding the eigenvalues of the energy denominator predicted by the continuum-dressed state model yields the same result as solving a three-level Λ EIT system using the dressed state treatment. I will further demon-

strate a exceptional control over the energy of the bound state $|g_1\rangle$ by illustrating the tuning of $|g_1\rangle$ for various optical parameters. I will begin this section by finding the real part of the energy denominator for the zero momentum case $k = 0$.

2.4.1 Tuning Rate of $|g_1\rangle$: Continuum-dressed State Model

For the zero-momentum $k = 0$ case, the energy denominator evaluated for the broad resonance in Eq. 2.39 and the narrow resonance in Eq. 2.40 yield the same result. The real part of Eq. 2.39 and Eq. 2.40 for $k = 0$ both yield,

$$\frac{D(E,E_k)}{\hbar} = -\Delta_e - \frac{\Omega_2^2}{4\delta} - \frac{\Omega_1^2}{4}\frac{\hbar}{2\mu_B \Delta B}\left(\frac{1}{\tilde{\Delta}_0}\right). \tag{2.81}$$

Substituting $\tilde{\Delta}_0 = (B - B_{res})/\Delta B = \Delta_0/\Delta B$ in Eq. 2.81 gives,

$$\frac{D(E,E_k)}{\hbar} = -\Delta_e - \frac{\Omega_2^2}{4\delta} - \frac{\Omega_1^2}{4}\frac{\hbar}{2\mu_B \Delta_0}. \tag{2.82}$$

Rewriting the single-photon detuning Δ_e and the two-photon detuning δ in terms of the laser detunings Δ_1, Δ_2 in Eq. 2.43 and Eq. 2.44, and magnetic field detuning Δ_0 yield,

$$\frac{D(E,E_k)}{\hbar} = -(\Delta_1 - \Delta_0) - \frac{\Omega_2^2}{4(\Delta_2 - \Delta_1 + \Delta_0)} - \frac{\Omega_1^2}{4}\frac{\hbar}{2\mu_B \Delta_0}. \tag{2.83}$$

Rewriting Eq. 2.83 and equating to zero yields,

$$\Delta_0\left[(\Delta_1 - \Delta_0)(\Delta_2 - \Delta_1 + \Delta_0) + \frac{\Omega_2^2}{4}\right] - \frac{\Omega_1^2}{4}\frac{\hbar}{2\mu_B}(\Delta_2 - \Delta_1 + \Delta_0) = 0. \tag{2.84}$$

Next I will determine the tuning rate of state $|g_1\rangle$ with energy E_{g_1}. The energy of the triplet state E_T tunable with respect to E_{g_1} can be defined in terms of the magnetic detuning Δ_0 as

$$\hbar\,\Delta \equiv E_T - E_{g_1} = -\hbar\,\Delta_0 \tag{2.85}$$

Replacing Δ_0 with $-\Delta$ in Eq. 2.84 yields,

$$-\Delta\left[(\Delta_1 + \Delta)(\Delta_2 - \Delta_1 - \Delta) + \frac{\Omega_2^2}{4}\right] - \frac{\Omega_1^2}{4}\frac{\hbar}{2\mu_B}(\Delta_2 - \Delta_1 - \Delta) = 0. \tag{2.86}$$

The tuning rate of all three dressed states can be evaluated by solving Eq. 2.86 for Δ. In the next section, I will demonstrate that solving for the eigenenergies of a Three-level Λ EIT system yield the same result.

2.4.2 Tuning Rate of $|g_1\rangle$: Dressed State Treatment of a Three-level Λ EIT system

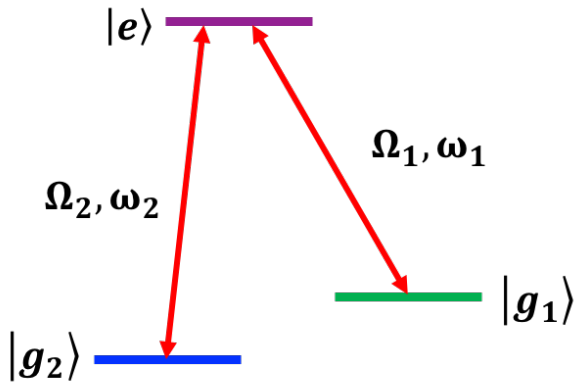

Figure 2.7 Three-level Λ EIT system. Optical fields ω_1 (with Rabi frequency Ω_1) and ω_2 (with Rabi frequency Ω_2) couple the ground molecular states $|g_1\rangle$ and $|g_2\rangle$ to the excited molecular state $|e\rangle$ of the singlet potential.

In the atom-field basis, the eigenstates are represented by also including the photon number n_1 and n_2 in the ν_1 and ν_2 optical beams, respectively. Hence, the states $|g_1\rangle$, $|g_2\rangle$, and $|e\rangle$ are replaced by atom-field product states.

For the two-photon transition illustrated in Fig. 2.7, n_1 photons in state $|g_1\rangle$ and n_2 photons in state $|g_2\rangle$ are present initially. The initial state is $|n_1, n_2, g_1\rangle$. The two-photon process can be summarized in two-steps,
i) The $|g_1\rangle - |e\rangle$ transition resulting in the loss of one photon in the ν_1 beam. Therefore,

$$|n_1, n_2, g_1\rangle \rightarrow |n_1 - 1, n_2, e\rangle. \tag{2.87}$$

ii) The $|g_2\rangle - |e\rangle$ transition results in the gain of one photon in the ν_2 beam from the ν_1

beam. Therefore,

$$|n_1-1, n_2, e\rangle \rightarrow |n_1-1, n_2+1, g_2\rangle. \tag{2.88}$$

The Hamiltonian of the system with no interactions is,

$$\vec{H}_0 = \hat{n}_1\hbar\omega_1 + \hat{n}_2\hbar\omega_2 + |e\rangle\langle e|E_e + |g_1\rangle\langle g_1|E_{g_1} + |g_2\rangle\langle g_2|E_{g_2} \tag{2.89}$$

where E_{g_1}, E_{g_2}, and E_e are the energy of the states $|g_1\rangle$, $|g_2\rangle$, and $|e\rangle$, respectively. The interaction Hamiltonian H_{int} in the presence of optical fields in the rotating-wave approximation is written as,

$$\vec{H}'_{int} = -\frac{1}{2}\mu_{eg_1}\left[|e\rangle\langle g_1|\,a_1 + |g_1\rangle\langle e|\,a_1^+\right]\epsilon_{10} - \frac{1}{2}\mu_{eg_2}\left[|e\rangle\langle g_2|\,a_2 + |g_2\rangle\langle e|\,a_2^+\right]\epsilon_{20} \tag{2.90}$$

where μ_{eg_1} and μ_{eg_2} are the dipole moment operators, a and a^+ are the annihilation and creation operators, and ϵ_{10} and ϵ_{20} are the single photon fields. From the properties of creation and annihilation operators, we know

$$\langle n_1-1|a_1|n_1\rangle = \sqrt{n_1} \approx \sqrt{\bar{n}_1} \tag{2.91}$$

$$\langle n_1|a_1^+|n_1-1\rangle = \sqrt{n_1} \approx \sqrt{\bar{n}_1} \tag{2.92}$$

where I assume a coherent state $\frac{\Delta n_1}{\bar{n}_1} = \frac{1}{\sqrt{\bar{n}_1}} << 1$. Using Eq. 2.91 and Eq. 2.92 and from the definition of Rabi frequency,

$$-\mu_{eg_1}\epsilon_{10} \approx \frac{\hbar\Omega_1}{\sqrt{\bar{n}_1}} \tag{2.93}$$

$$-\mu_{eg_2}\epsilon_{20} \approx \frac{\hbar\Omega_2}{\sqrt{\bar{n}_2}} \tag{2.94}$$

where Ω_1 and Ω_2 are the Rabi frequencies for the $|g_1\rangle - |e\rangle$ and $|g_2\rangle - |e\rangle$ transitions, respectively.

Using Eq. 2.93 and Eq. 2.94 in Eq. 2.90 yields,

$$\vec{H}'_{int} \approx \frac{\hbar\Omega_1}{2\sqrt{\bar{n}_1}}\left[|e\rangle\langle g_1|\,a_1 + |g_1\rangle\langle e|\,a_1^+\right] + \frac{\hbar\Omega_2}{2\sqrt{\bar{n}_2}}\left[|e\rangle\langle g_2|\,a_2 + |g_2\rangle\langle e|\,a_2^+\right] \tag{2.95}$$

I now proceed to rewrite the energies of the states $|n_1-1, n_2+1, g_2\rangle$ and $|n_1-1, n_2, e\rangle$ by

defining the energy E_1^0 of state $|n_1, n_2, g_1\rangle$ as zero. Therefore, For $|n_1, n_2, g_1\rangle$,

$$E_1^0 \equiv 0 \equiv n_1\hbar\omega_1 + n_2\hbar\omega_2 + \hbar\omega_{g_1}. \tag{2.96}$$

For state $|n_1-1, n_2, e\rangle$,

$$E_2^0 = -\hbar\omega_1 + \hbar(\omega_e - \omega_{g_1}) \equiv -\hbar\Delta_1, \tag{2.97}$$

where

$$\Delta_1 \equiv \omega_1 - \omega_{eg_1}, \tag{2.98}$$

is the single photon detuning. For state $|n_1-1, n_2+1, g_2\rangle$,

$$E_3 = -\hbar\,\omega_1 + \hbar\omega_2 + \hbar(\omega_{g_2} - \omega_{g_1}) \tag{2.99}$$

Adding and subtracting ω_e in Eq. 2.99 yields,

$$E_3 = \hbar\big[\omega_2 - \omega_1 + \omega_e + \omega_{g_2} - \omega_e - \omega_{g_1}\big] \tag{2.100}$$

Rewriting the above equation gives,

$$E_3 = \hbar\big[\big(\omega_2 - (\omega_e - \omega_{g_2})\big) - \big(\omega_1 - (\omega_e - \omega_{g_1})\big)\big] \tag{2.101}$$

Defining the single-photon detunings Δ_1 for the the $|g_1\rangle - |e\rangle$ transition and Δ_2 for the the $|g_2\rangle - |e\rangle$ transition as

$$\Delta_2 \equiv \omega_2 - (\omega_e - \omega_{g_2}) \tag{2.102}$$

$$\Delta_1 \equiv \omega_1 - (\omega_e - \omega_{g_1}) \tag{2.103}$$

Then E_3 is rewritten in terms of optical detunings,

$$E_3 \equiv \hbar\,[\Delta_2 - \Delta_1] \tag{2.104}$$

The two-photon detuning is defined as

$$\delta_{21} = \Delta_1 - \Delta_2 \tag{2.105}$$

where $\delta_{21} = 0$ defines the optical field arrangement when the frequency difference between the ν_1 and ν_2 beam is equal to the energy difference between the $|g_1\rangle$ and $|g_2\rangle$ states.

Rewriting Eq. 2.104 in terms of the two-photon detuning in Eq. 2.105 yields

$$E_3 \equiv -\hbar\delta_{21} \tag{2.106}$$

Using equation Eq. 2.96, Eq. 2.97, and Eq. 2.106, the Hamiltonian of the system in the matrix form is written as

$$H = \hbar \begin{bmatrix} 0 & \Omega_1/2 & 0 \\ \Omega_1/2 & -\Delta_1 & \Omega_2/2 \\ 0 & \Omega_2/2 & \Delta_2-\Delta_1 \end{bmatrix} \tag{2.107}$$

In order to solve for the eigenvalues of the Hamiltonian in Eq. 2.107, the Schrödinger equation is written as

$$H \begin{bmatrix} \alpha \\ \beta \\ \gamma \end{bmatrix} = \hbar\epsilon \begin{bmatrix} \alpha \\ \beta \\ \gamma \end{bmatrix} \tag{2.108}$$

where ϵ is the energy eigenvalue and α, β, γ are the eigenvectors. Solving Eq. 2.108 for the eigenvalue gives,

$$\det \begin{vmatrix} -\epsilon & \Omega_1/2 & 0 \\ \Omega_1/2 & -\Delta_1-\epsilon & \Omega_2/2 \\ 0 & \Omega_2/2 & \Delta_2-\Delta_1-\epsilon \end{vmatrix} = 0 \tag{2.109}$$

Solving the determinant in Eq. 2.109 yields,

$$\epsilon\left[\left(\Delta_1+\epsilon\right)\left(\Delta_2-\Delta_1-\epsilon\right)+\frac{\Omega_2^2}{4}\right]+\frac{\Omega_2^2}{4}\left(\Delta_2-\Delta_1-\epsilon\right)=0. \tag{2.110}$$

As expected, Eq. 2.110 is a cubic equation in ϵ and gives three solutions which represent the eigenvalue of the three dressed states in our Λ EIT system. Eq. 2.110 is the same equation as Eq. 2.86 with Δ replaced by ϵ, thereby illustrating that both the dressed state treatment of a simple Λ EIT system and the energy denominator derived from the optically controlled scattering state in the continuum-dressed state model yield the same results for the tuning rate of $|g_1\rangle$.

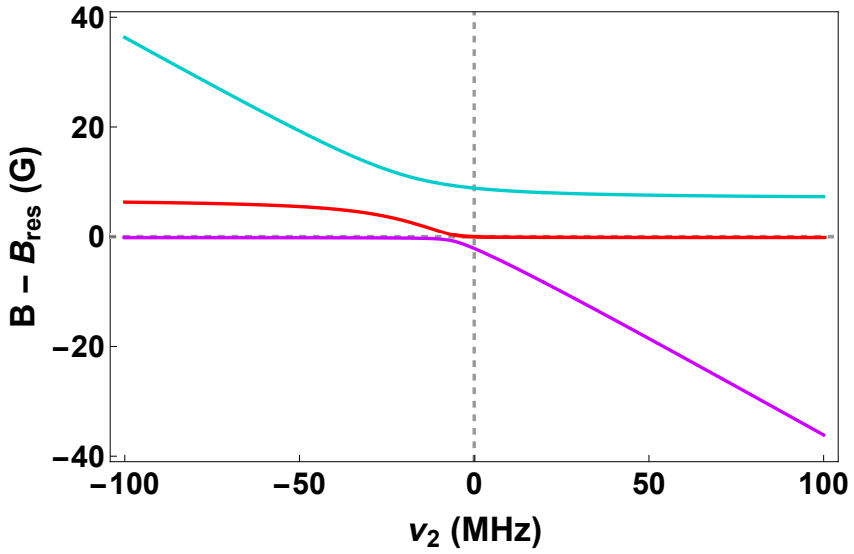

Figure 2.8 Eigenvalues of the energy denominator as a function of frequency ν_2. Here B = 0 refers to the magnetic field at which the narrow Feshbach resonance occurs and $\nu_2 \equiv 0$ represents the two-photon detuning $\delta = 0$. The Rabi frequencies $\Omega_1 = 0.5\,\gamma_e$, $\Omega_2 = 2.0\,\gamma_e$ and the detuning $\Delta_1 =$ 18.85 MHz.

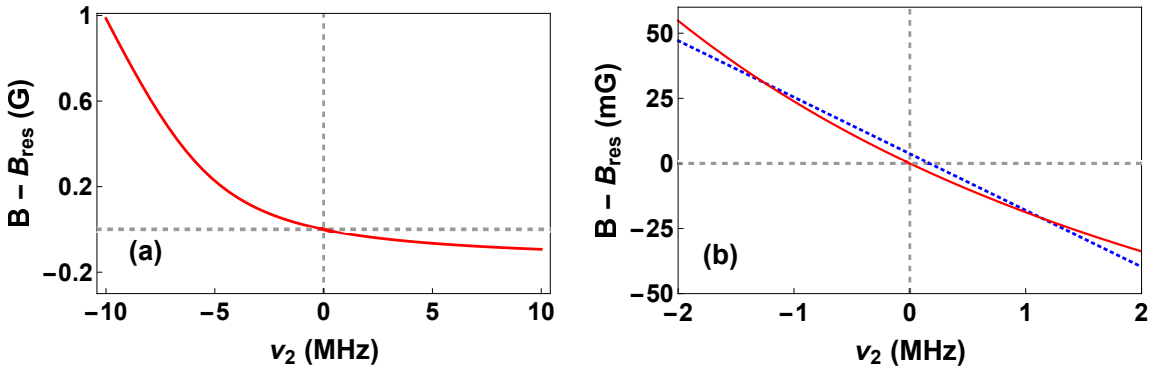

Figure 2.9 (a) Tuning of the ground state $|g_1\rangle$ as a function of the frequency ν_2. (b) Theoretical prediction (red dots) of the ground state position is fitted to a line $y = mx + c$ (blue line) to calculate the tuning rate. Here B = 0 refers to the magnetic field at which the narrow Feshbach resonance occurs and $\nu_2 \equiv 0$ represents the two-photon detuning $\delta = 0$. The Rabi frequencies and the detuning are $\Omega_1 = 0.5\,\gamma_e$, $\Omega_2 = 2.0\,\gamma_e$ and $\Delta_1 = 18.85$ MHz.

2.4.3 Tuning Rate of $|g_1\rangle$: Predictions of the Continuum-dressed State Model

In this section, I will use the continuum-dressed state model to illustrate the tuning of the state $|g_1\rangle$ for different optical parameters. Optical control of interactions near a magnetic Feshbach resonance is achieved by tuning the ground state $|g_1\rangle$ using optical fields and making the ground state $|g_1\rangle$ degenerate with the triplet continuum $|T,k\rangle$ in the bare basis picture. In our optical technique, the presence of both the optical beams contributes to the tuning the ground state $|g_1\rangle$.

The tuning of state $|g_1\rangle$ is determined by solving Eq. 2.84 for Δ_0, yielding three solutions. Each of these solutions is dependent on the magnetic field B and the frequency ν_2 of the EIT beam. Since all the experiments reported in this thesis involves the tuning of $|g_1\rangle$ by varying ν_2, all plots shown in this section are generated with ν_2 as the tuning parameter.

Fig. 2.8 shows the the three solutions as a function of frequency ν_2. The y-axis represents the position of the three states with respect to the narrow Feshbach resonance. Here B = 0 refers to the magnetic field at which the narrow Feshbach resonance occurs. The optical parameters used to generate this plot are Rabi frequencies $\Omega_1 = 0.5\,\gamma_e$, $\Omega_2 = 2.0\,\gamma_e$ and the detuning $\Delta_1 = 18.85$ MHz. Here $\nu_2 \equiv 0$ represents the two-photon detuning $\delta = 0$.

Of the three states shown in Fig. 2.8, the state that has maximum $|g_1\rangle$ contribution is shown in red. It is the only relevant state since the experiments are done very close to the narrow Feshbach resonance. Fig. 2.9a shows the expanded view of the red curve to illustrate the tuning of the ground state $|g_1\rangle$ as a function of the frequency ν_2. To determine the tuning rate of the ground state $|g_1\rangle$ near the two-photon detuning, the red curve is fit to a line, $y = m\,x + c$ (blue line) and shown in Fig. 2.9b. For the optical parameters used, the tuning rate is calculated to be 21.7 mG/MHz.

2.4.4 Tuning of Ground State $|g_1\rangle$ for Different Rabi Frequencies Ω_2

In this section, I will illustrate the tuning of the ground state $|g_1\rangle$ for different Rabi frequencies Ω_2. Fig. 2.10a shows the position of ground state $|g_1\rangle$ with respect to the narrow Feshbach resonance at 543.27 G as a function of the frequency ν_2 for different Rabi frequencies Ω_2. The optical parameters used to generate the plots are Rabi frequency $\Omega_1 = 1\,\gamma_e$ and the detuning $\Delta_1 = 18.85$ MHz. Since the Rabi frequency Ω_1 is held constant, away from the two-photon resonance (ν_2 = -100 MHz), the ground state $|g_1\rangle$ is at the same position for

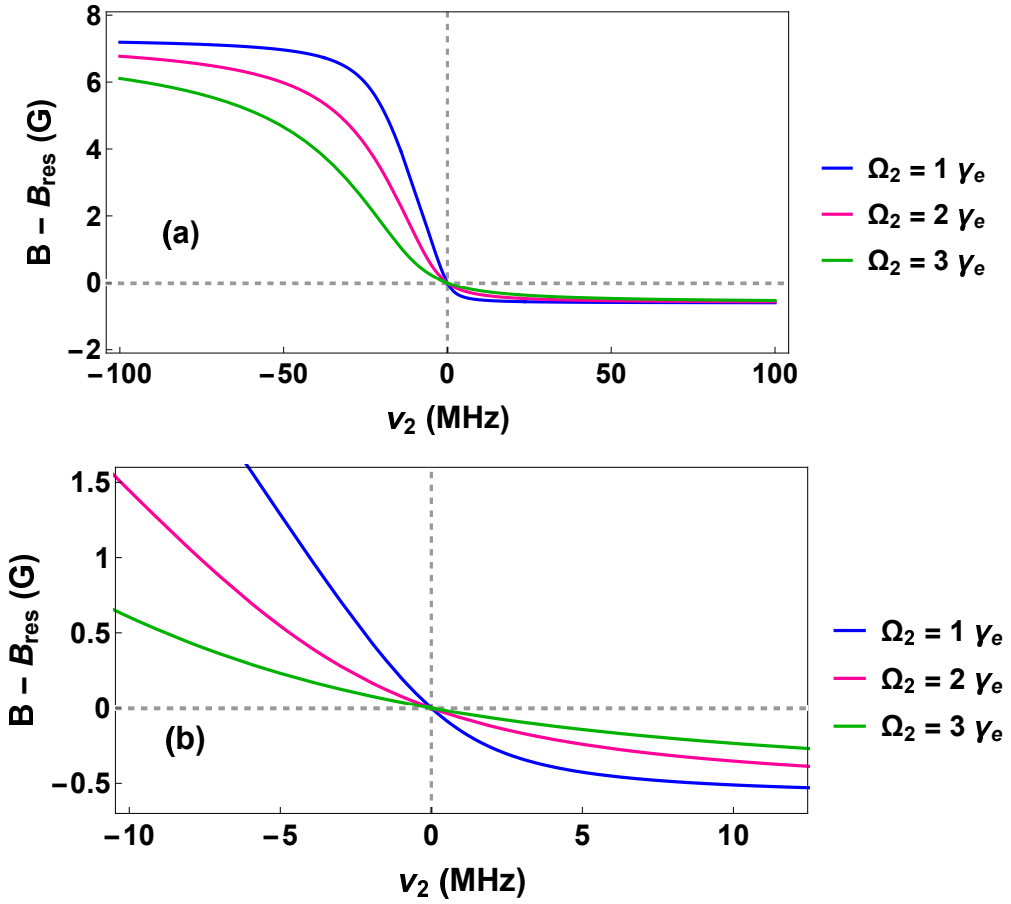

Figure 2.10 (a) Ground state $|g_1\rangle$ tuning versus frequency ν_2 for a fixed $\Omega_1 = 0.5\gamma_e$ and $\Omega_2 = 1\ \gamma_e$ (blue), $\Omega_2 = 2\ \gamma_e$ (magenta), $\Omega_2 = 3\ \gamma_e$ (green); $\Delta_1 = 18.85$ MHz. (b) Expanded plot of Fig. 2.10a. Here B = 0 refers to the magnetic field at which the narrow Feshbach resonance occurs and $\nu_2 \equiv 0$ represents the two-photon detuning $\delta = 0$.

all three Ω_2 values. As the frequency ν_2 is changed, the tuning rate of the ground state $|g_1\rangle$ varies for different values of Ω_2. This is due to the fact that the ratio of Ω_1/Ω_2 is different for a fixed Ω_1. But at the two-photon resonance $\nu_2 = 0$, the ground state $|g_1\rangle$ goes back to its original position (543.27 G) for all values of Ω_2. This is illustrated clearly in the Fig. 2.10b, which is the expanded view of Fig. 2.10a.

2.4.5 Tuning of Ground State $|g_1\rangle$ for Different Rabi Frequencies Ω_1

Fig. 2.11a shows $|g_1\rangle$ state tuning for different Rabi frequencies Ω_1 as a function of the frequency ν_2. Here B = 0 G represents the narrow Feshbach resonance at 543.27 G. The Rabi

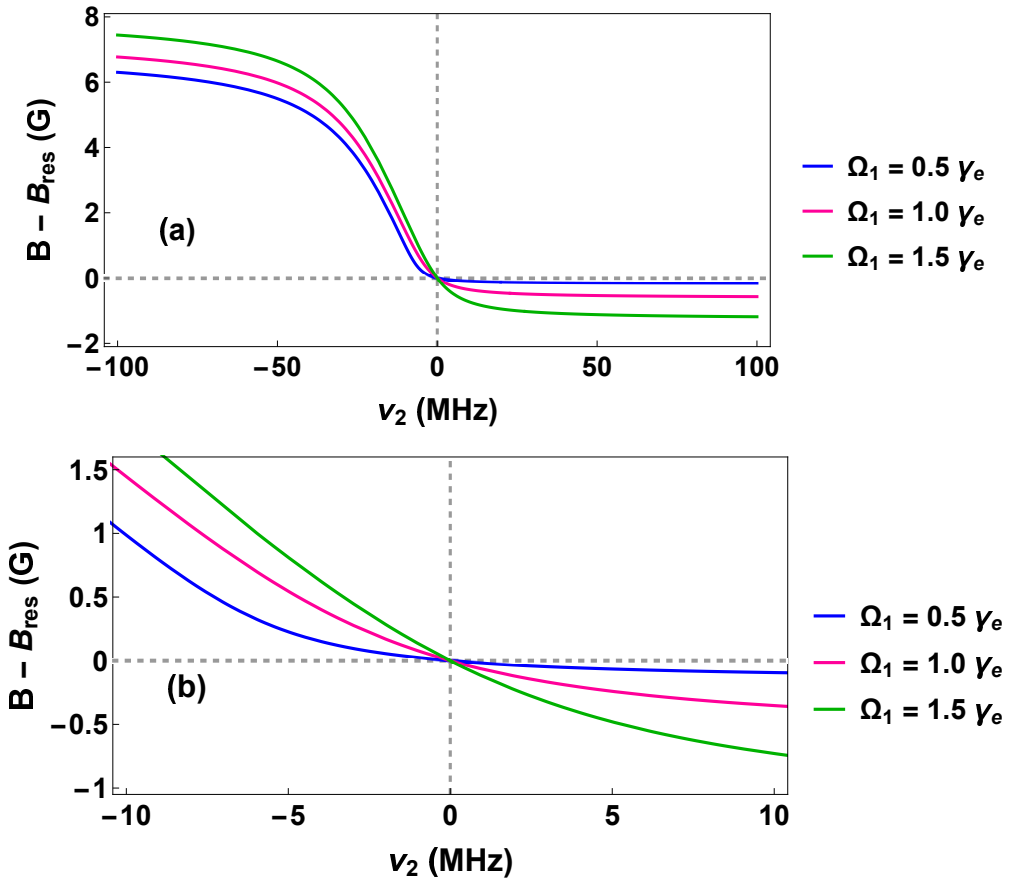

Figure 2.11 (a) Ground state $|g_1\rangle$ tuning versus frequency ν_2 for a fixed Ω_2 and $\Omega_1 = 0.5\,\gamma_e$ (blue), $\Omega_1 = 1\,\gamma_e$ (magenta), $\Omega_1 = 1.5\,\gamma_e$ (green). Here $\Omega_2 = 2\,\gamma_e$ and $\Delta_1 = 18.85$ MHz. (b) Expanded plot of Fig. 2.11a. Here B = 0 refers to the magnetic field at which the narrow Feshbach resonance occurs and $\nu_2 \equiv 0$ represents the two-photon detuning $\delta = 0$.

frequency $\Omega_2 = 2\,\gamma_e$ and the detuning $\Delta_1 = 18.85$ MHz are used to compute the plot. The ν_1 optical beam shifts the ground state $|g_1\rangle$ and this shift is dependent on the Rabi frequency Ω_1. Hence the ground state $|g_1\rangle$ is at different initial positions (near ν_2 = - 100 MHz) for different Ω_1. But at two-photon resonance, $\nu_2 = 0$, the ground state goes back to its original position for all values of Ω_1 and is shown in Fig. 2.11b.

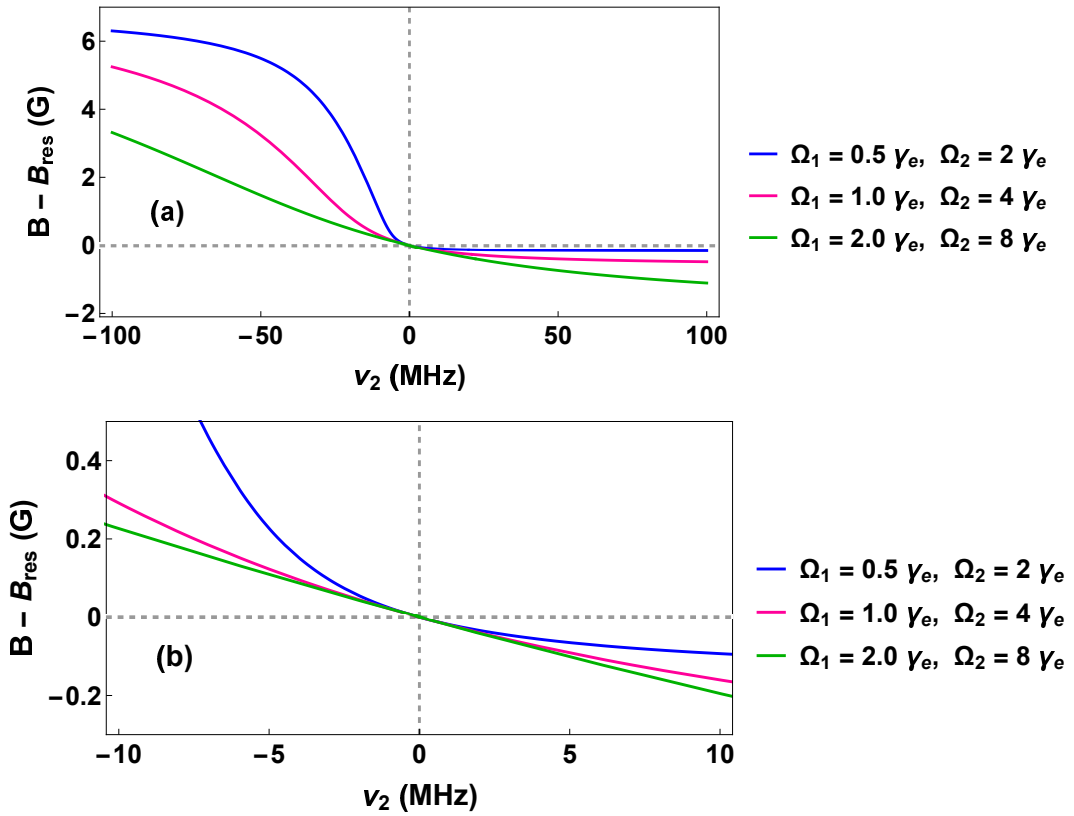

Figure 2.12 (a) Ground state $|g_1\rangle$ tuning versus frequency ν_2 for a fixed Ω_1/Ω_2 ratio with $\Omega_1 = 0.5\,\gamma_e$, $\Omega_2 = 2\,\gamma_e$ (blue), $\Omega_1 = 1\,\gamma_e$, $\Omega_2 = 4\,\gamma_e$ (magenta), $\Omega_1 = 2\,\gamma_e$, $\Omega_2 = 8\,\gamma_e$ (green); $\Delta_1 = 18.85$ MHz. (b) Expanded plot of Fig. 2.12a. Here B = 0 refers to the magnetic field at which the narrow Feshbach resonance occurs and $\nu_2 \equiv 0$ represents the two-photon detuning $\delta = 0$.

2.4.6 Tuning of Ground State $|g_1\rangle$ for Different Ratio of Rabi Frequencies Ω_1 / Ω_2

Fig. 2.12a displays the plot of ground state tuning as a function of the frequency ν_2. To generate this plot, both Ω_1 and Ω_2 is varied, but the ratio of Rabi frequencies Ω_1 and Ω_2 is held constant. The detuning $\Delta_1 = 18.87$ MHz is used to produce this plot. Fig. 2.12b is an enlarged representation of Fig. 2.12a.

Near the two-photon resonance, the tuning rate of the ground state is same for all combination of Ω_1 and Ω_2. This is further examined by fitting the slope of all three curves to a line, $y = mx + c$ (yellow line) and is shown in Fig. 2.13. For the optical parameters employed, a tuning rate of 21.7 mG/MHz is obtained for all three curves.

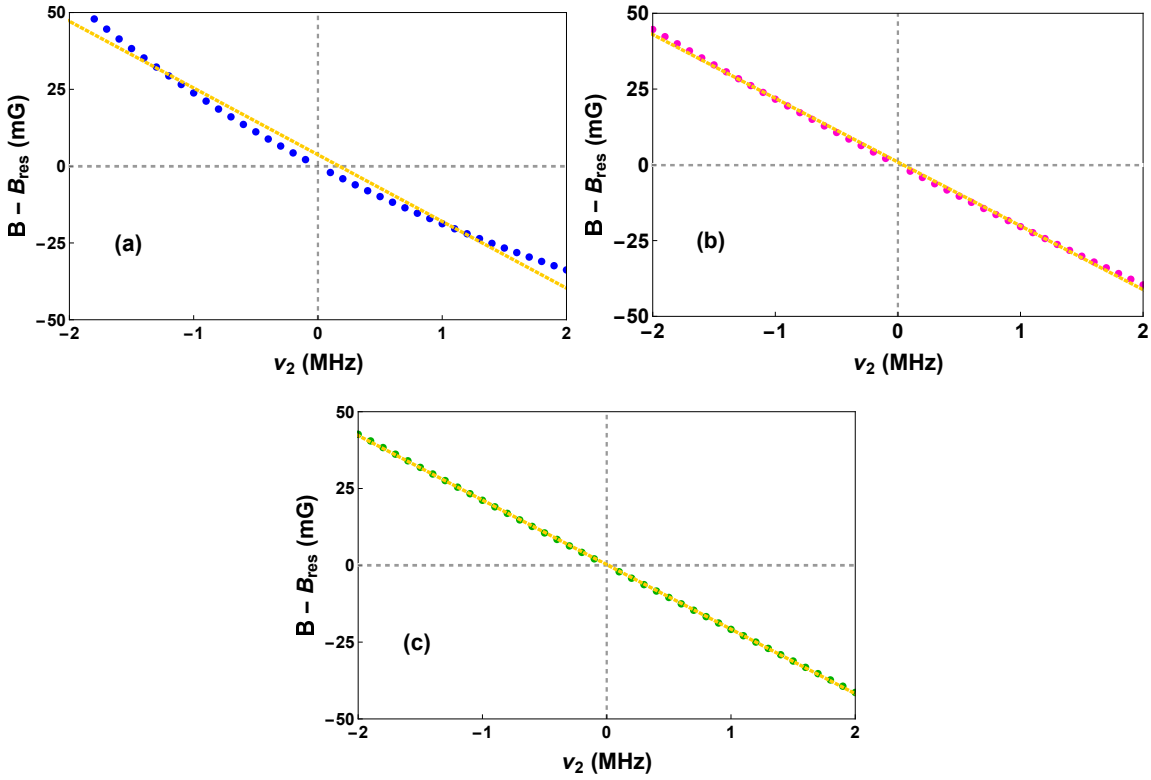

Figure 2.13 Theoretical prediction (dots) of the ground state position is fitted to a line $y = mx + c$ (yellow line) to calculate the tuning rate for (a) $\Omega_1 = 0.5\,\gamma_e, \Omega_2 = 2\,\gamma_e$ (blue), (b) $\Omega_1 = 1\,\gamma_e, \Omega_2 = 4\,\gamma_e$ (magenta), (c) $\Omega_1 = 2\,\gamma_e, \Omega_2 = 8\,\gamma_e$ (green). Here B = 0 refers to the magnetic field at which the narrow Feshbach resonance occurs and $\nu_2 \equiv 0$ represents the two-photon detuning $\delta = 0$. The detuning $\Delta_1 = 18.85$ MHz.

CHAPTER

3

EXPERIMENTAL METHODS

In this chapter, I will discuss the experimental setup used to create an ultracold gas of ^{6}Li atoms and the optical system used to control two-atom interactions. The process of creating an ultracold gas has been well documented in the previous thesis from our group [O'H00; Geh03; Kin06] and has gone through minor modifications recently [Ell14]. Hence in this chapter, the cooling and trapping techniques will only be discussed briefly in Section 3.1.

The main focus of this chapter will be on the newly developed optical system used to control the interactions in ultracold atoms by electromagnetically induced transparency (EIT). The optical system involves three diode lasers, a reference laser that acts as a frequency reference and two lasers that generate the probe and pump beam for the EIT experiments. All three lasers are frequency stabilized using a variety of frequency stabilizing techniques, which will be discussed in Section 3.2. The measurement and calibration of the frequencies ν_1, ν_2 and the Rabi frequencies Ω_1, Ω_2 of the optical beams will be described in Section 3.3. A stable magnetic field is critical in order to optically control interactions near the narrow Feshbach resonance (width $\Delta B = 0.1$ G) of ^{6}Li. In Section 3.5, I will discuss the path to achieving magnetic field stabilization to better than 10 mG. The primary trapping poten-

tial for our ultracold gas is provided by a far-off resonant CO_2 beam. Therefore, physical parameters of our ultracold gas such as the temperature and density can only be measured by a thorough characterization of the optical trap. This involves measuring the oscillation frequencies of weakly interacting atoms in the trap through a process called parametric resonance, which will be discussed in the final section of this chapter.

3.1 Preparation of Cold Atom Samples

In this section, I will describe the experimental methods used to create an ultracold gas of ^{6}Li atoms. Cooling and trapping of atoms is achieved in several stages by making use of a magneto-optical trap (MOT) and a far-off resonance trap (FORT). Both of these traps are discussed briefly in this section and a detailed description can be found here [Kin06].

3.1.1 Magneto-Optical Trap (MOT)

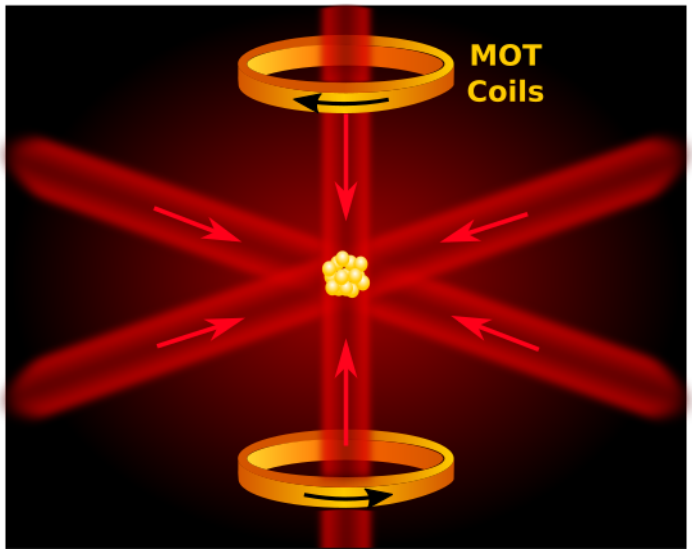

Figure 3.1 Magneto-optical trap (MOT). Six optical beams in three directions (two counter-propagating beams for each direction) and magnetic fields trap the atoms at its center, cooling the atoms to a temperature of approximately 140 μK.

A magneto-optical trap (MOT) works on the principle of optical molasses. A red detuned

optical beam is shined on the atoms in a direction opposite to the direction in which the atom is traveling. When an atom absorbs a photon moving towards it, the momentum of the photon is transferred to the atoms. This results in a momentum kick for the atom in a direction opposite to its initial motion. When the atom re-emits the photon through spontaneous emission, the momentum kick for the atom is in a random direction. After multiple absorptions and emission cycles, the atom gets a net momentum kick opposite to its initial direction of motion thereby slowing the atom.

A pair of counter-propagating beams will, therefore, slow the atom in one dimension. Hence by using six counter-propagating beams, two for each direction, atoms can be trapped in all three dimensions. In our lab, a dye laser resonant with the D_2 transition of ^{6}Li is used to generate the “red" MOT beams in order to initially trap the atoms in all three directions. As the atoms slow down in velocity space, they slowly random walk due to lack of spatial confinement. This random walk can be eliminated by using inhomogeneous magnetic fields to generate a spatially dependent Zeeman shift of the hyperfine levels. This ensures that the atoms experience a restoring force back to the center of the trap.

At the end of this cooling phase, we have typically three million atoms at approximately 140 μk. The next phase of cooling involves a far-off resonance trap, where temperatures as low as 10 nK are achieved.

3.1.2 Far Off Resonance Trap (FORT)

In this stage of cooling, a CO_2 laser at 10.6 μm is used to create a far-off resonance trap. Since the frequency of the CO_2 laser is far away from the D_2 line of lithium transition, it creates an optical dipole force on the atoms. The optical dipole force is proportional to the intensity of the CO_2 laser. The CO_2 beam is focused to a beam size of 60 μm to achieve an intensity of 2×10^6 W/cm^2. After initially cooling the atoms using MOT, the atoms are loaded into the FORT. The atoms are attracted to the high intensity region and confined to the shape of CO_2 potential, with stronger confinement in the radial direction and weaker confinement in the axial direction.

Once the atoms are loaded into the FORT, further cooling is achieved using a two-stage evaporative process, namely, free evaporation and forced evaporation. In the free evaporation cooling stage, a high bias magnetic field is applied, so that the collisional rate of the atoms increases drastically and wait for approximately 10 s. As the atoms collide with each other, the hotter atoms remove energy from the colder atoms and escape from the optical

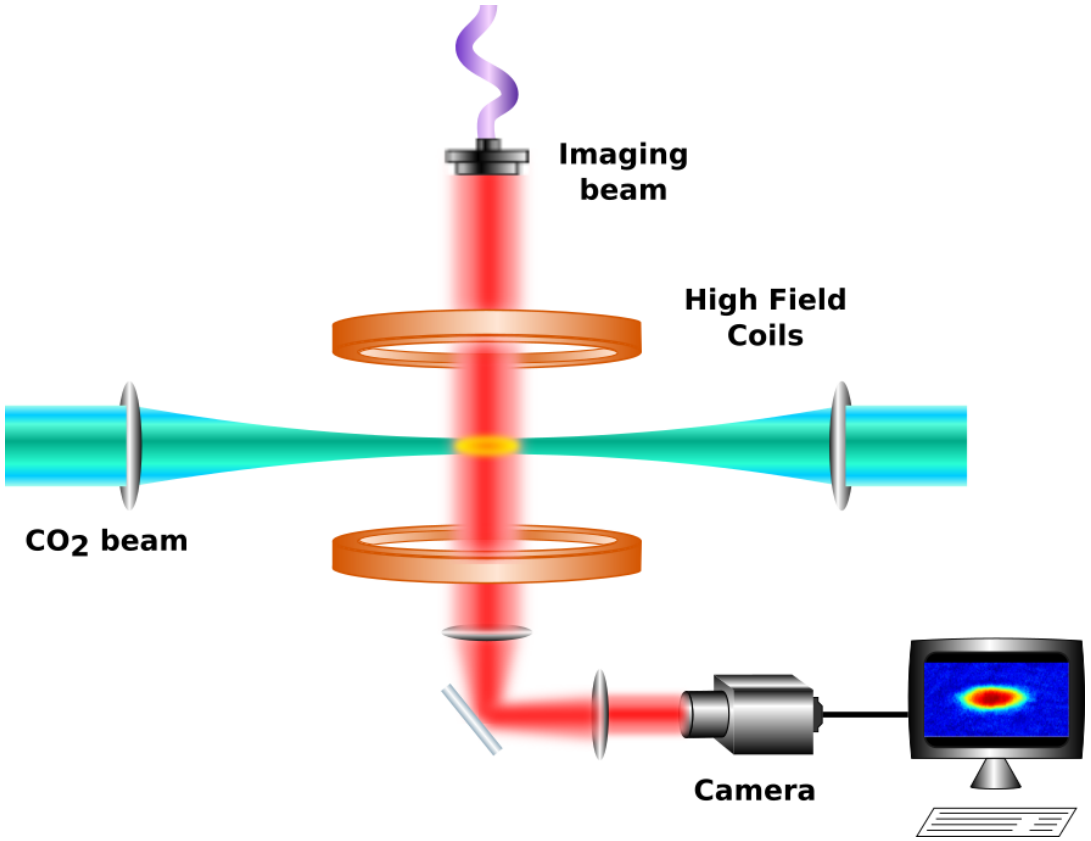

Figure 3.2 Schematic for trapping and imaging cold atoms. The CO_2 laser beam is focused to a beam size of 60 μm and traps the atoms at its focus. The high field coils generate magnetic fields to tune the interactions between cold atoms. The imaging beam path for the high resolution imaging setup is also shown.

trap, thereby leaving behind the colder atoms. The efficiency of the free evaporation depends on the rate of collisions. Therefore, a magnetic field where the scattering cross-section of the atom is maximum is chosen. For experiments near the broad Feshbach resonance ($B_{res} = 832.2$ G) in ^{6}Li, the resonance magnetic field of the broad Feshbach resonance at 832.2 G is used. For experiments near the narrow Feshbach resonance ($B_{res} = 543.28$ G), the atoms are cooled at 300 G where the background scattering length is about 300 a_0, where a_0 is the Bohr radius. Cooling at the resonance magnetic field of the narrow Feshbach resonance is avoided due to excessive atom loss because of three-body collisions [Haz12]. This process is allowed to take place for 5 sec and results in 4.5 to 5 $\times 10^5$ atoms per spin state at 150 μk.

The next stage in evaporative cooling is the forced evaporation stage, where the trap

depth is reduced adiabatically by changing the intensity of the CO_2 beam at the same high bias magnetic field. Since the collisional rate of the atoms is maximum at the high bias magnetic field, the hotter atom escapes when the trap depth is reduced leading to the coldest atoms remaining in the trap. The final temperature of the atoms depends on the lowering time and the lowest value of the CO_2 laser beam intensity. Our system is capable of achieving around 100,000 atoms per spin state at 0.1 μk. The optical trap is then reraised to the final trap depth based on the atom density required of our experiments. This completes the cooling and trapping stages of our experiment and we are left with an ultracold gas of ^{6}Li atoms that can be studied extensively.

Following the preparation of an ultracold gas, experiments are performed to optically control the two-body interactions of the atoms. The final stage of the experimental cycle involves imaging the atomic cloud through absorption imaging.

3.1.3 Imaging the Atomic Cloud

Fig. 3.2 shows the imaging setup including the paths of CO_2 and imaging beams used in our lab. The imaging beam is much larger (2.54 cm) than the size of the atomic cloud (200 μm).In absorption imaging, atoms absorb the photons in the imaging beam and cast a shadow of the atom cloud on the CCD camera. The images are taken with (signal shot) and without (reference shot) the atom cloud under the same experimental conditions. The signal and the reference images are subtracted from each other to produce the false color 2D column density image shown in Fig. 3.2. From the false color image, atom number and the cloud widths are extracted.

3.2 Development of Optical Control System

In this section, I will explain in detail the optical system for controlling interactions in ultracold atoms using EIT. The basic level scheme for EIT control of interactions is shown in Fig. 3.3.

Optical fields ν_1 and ν_2, with Rabi frequencies Ω_1 and Ω_2, couple the ground molecular states of the singlet potential, $|g_1\rangle$ and $|g_2\rangle$, to the excited state $|e\rangle$. The triplet continuum $|T,k\rangle$ is coupled to state $|g_1\rangle$ with a second order hyperfine coupling constant V_{HF}, which causes the narrow Feshbach resonance at $B_{res} = 543.27$ G where the width $\Delta B = 0.1$ G [Haz12]. The narrow Feshbach resonance is an energy-dependent resonance, where the

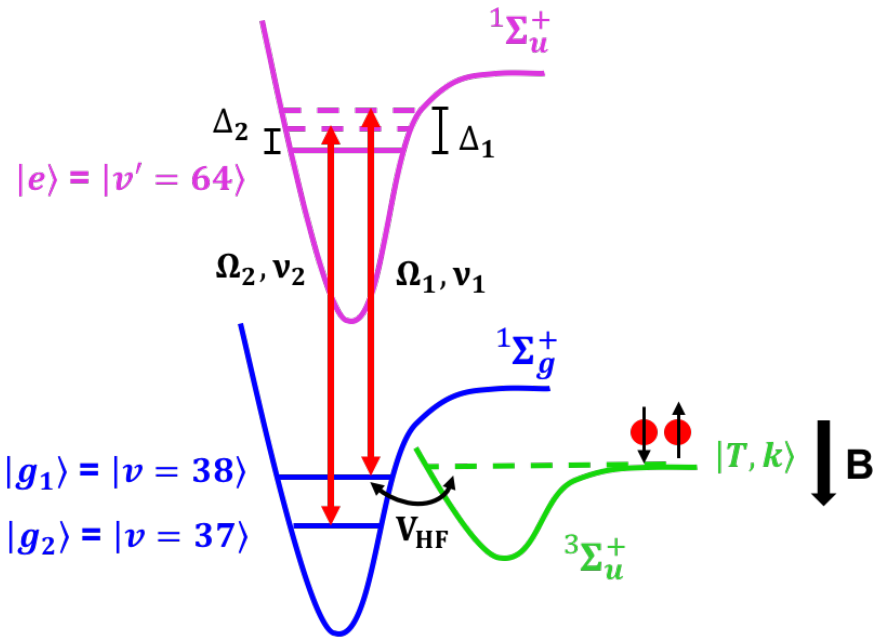

Figure 3.3 Basic level scheme for controlling interactions in ^{6}Li. Optical fields ν_1 (with Rabi frequency Ω_1 and detuning Δ_1) and ν_2 (with Rabi frequency Ω_2 and and detuning Δ_2) couple the ground molecular states $|g_1\rangle$ and $|g_2\rangle$ to the excited molecular state $|e\rangle$ of the singlet potential. The atoms are predominantly in the spin triplet state $|T,k\rangle$ which has an hyperfine coupling V_{HF} to state $|g_1\rangle$ causing the Feshbach resonance. The triplet state moves downward with increasing magnetic field B. For our optical control experiments in ^{6}Li, $|g_1\rangle = |v = 38\rangle$, $|g_2\rangle = |v = 37\rangle$, and $|e\rangle = |v' = 64\rangle$ are chosen.

resonance position can be tuned energetically by changing the temperature of the ultracold gas. The two lowest hyperfine states $|1\rangle$ and $|2\rangle$ also have a broad Feshbach resonance at $B_{res} = 832.2$ G with width $\Delta B = 300$ G [ZÏ3].

All the experiments reported in this thesis are primarily done near the narrow Feshbach resonance near 543.2 G. The atoms are predominantly in the spin triplet state $|T,k\rangle$, which tunes downward with magnetic field B as $-2\mu_B B$, where μ_B is the Bohr magneton. The states used in our experiments are,

$$|g_1\rangle = |v=38\rangle \tag{3.1}$$

$$|g_2\rangle = |v=37\rangle \tag{3.2}$$

$$|e\rangle = |v'=64\rangle \tag{3.3}$$

While designing an optical system for the level scheme shown in Fig. 3.3, several important considerations should be taken into account. For certain experiments, the optical fields should be tuned between the broad and the narrow Feshbach resonance which is separated by 300 G. This involves tuning the frequency of the lasers by approximately 1 GHz. Therefore a wide tunability of about 1 GHz is required. The frequency difference between states $|g_1\rangle$ and $|g_2\rangle$ is 57 GHz. Therefore, a large frequency offset between the ν_1 and ν_2 optical fields is needed. Also, since the experiments involve electromagnetically induced transparency, which uses the principle of quantum interference to suppress atom loss, the stability of the lasers is critical to maintaining coherence. Therefore, the relative frequency difference between the lasers is stabilized to better than 10 kHz. The optical system was therefore designed to achieve the following,

(i) Wide frequency tunability of ν_1 beam

(ii) Large frequency offset between ν_1 and ν_2

(iii) Good frequency stability between ν_1 and ν_2

A schematic design of our two-field optical system is shown in Fig. 3.4. The reference laser is locked to a Fabry-Perot cavity using a Pound-Drever-Hall (PDH) locking scheme. The PDH lock provides a high bandwidth error signal that can stabilize fast jitter in the lasers. The PDH scheme will be explained in detail later. A part of the beam from the reference laser is then sent into an iodine gas cell in a saturation absorption setup (explained below), which generates an error signal as it becomes resonant with one of the several iodine molecular resonances. As the cavity can drift due to thermal and mechanical fluctuations, the cavity is locked to the iodine error signal. This makes the *reference laser-cavity-Iodine* system the ultimate frequency reference for our experiments. The optical field ν_1 is generated by locking the ν_1 laser to the reference laser using a frequency offset lock (explained below).

As frequency offset lock provides wide tunability, it satisfies one of the primary requirements of having a widely tunable ν_1 field. The cavity has several resonances with width 7 MHz, which are separated by its free spectral range (1.5 GHz). The beam from the ν_2 laser is sent into the other open port of the cavity and is locked to the nearest cavity resonance that lies 57 GHz above the ν_1 laser. Therefore, a large frequency offset along with wide tunability and good stability is achieved, which are the fundamental requirements of our optical system to pursue our optical control experiments.

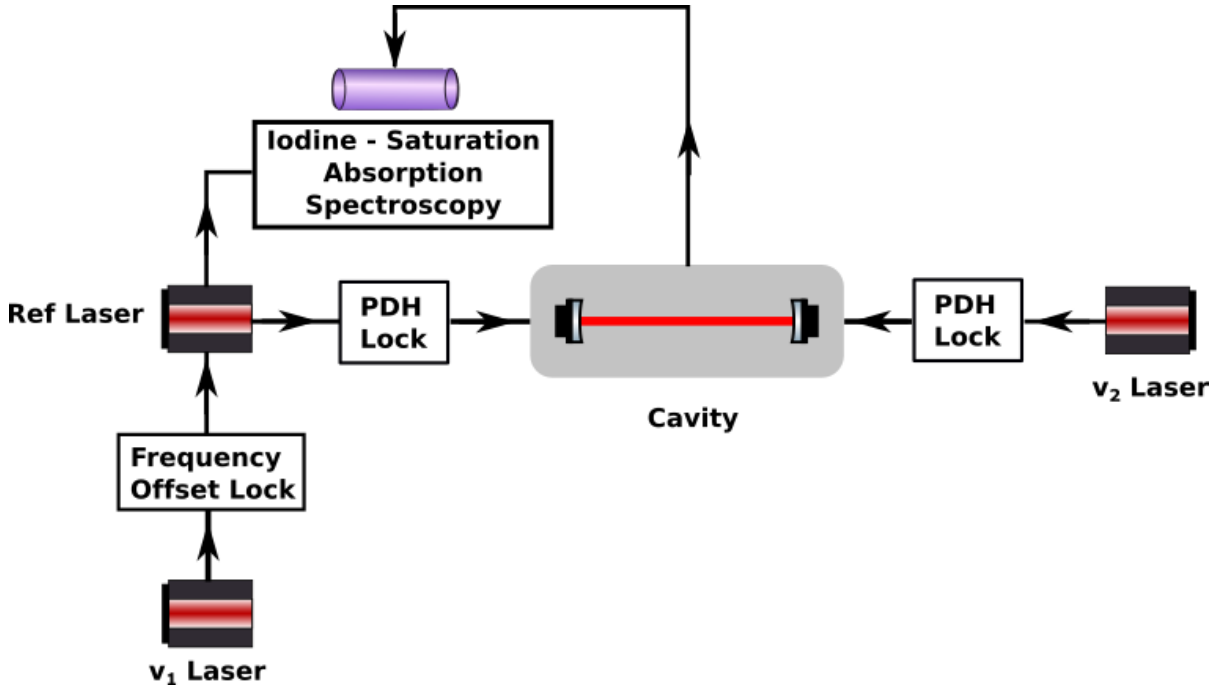

Figure 3.4 A simple schematic of the two-field optical control system

3.2.1 Pound Drever Hall (PDH) Lock

The Pound Drever Hall (PDH) locking technique is used to lock our reference and ν_2 laser to the cavity. Fig. 3.5 shows the setup for the PDH lock implemented in our system for the reference laser. Since the ν_2 laser has an identical setup, it is not shown in Fig. 3.5.

The electro-optic modulator (EOM) (Thorlabs EO-PM-R-30-C1) phase modulates the frequency of the optical field from the reference laser at 30 MHz. This phase modulation generates two sidebands at ±30 MHz, in addition to the carrier(reference) frequency ω_c. The carrier frequency ω_c along with both sidebands $\omega_c + 30$ and ω_c - 30 are then sent to the Fabry Perot (FP) cavity through a half wave plate (HWP) and a polarizing beam splitter (PBS). The reflected beam from the cavity is incident on an amplified photo-detector (Thorlabs PDA10A) which has a bandwidth of 150 MHz. The sideband frequencies ±30 MHz of the reference beam are greater than the line-width (7 MHz) of the cavity. With ω_c near a cavity resonance, the sidebands are reflected from the front surface of the cavity without any significant phase shift while the carrier frequency can be partially reflected or transmitted. The beat between the reflected carrier frequency with each of its sidebands is detected by the photo-detector. When the carrier frequency is near the cavity resonance, the incident

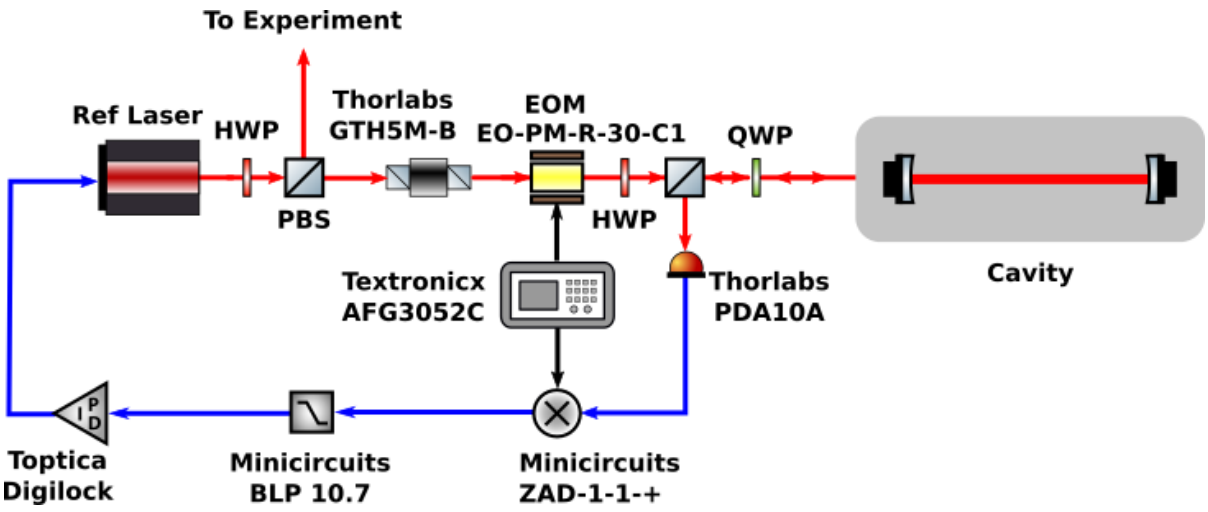

Figure 3.5 Pound Drever Hall locking set up for the reference laser

and reflected components of the carrier frequency have no phase shift. Hence the beats between the carrier and the upper sideband (+30 MHz) and the lower sideband (-30 MHz) are 180 degrees out of phase with respect to each other, thereby canceling each other with no signal at the photo-diode.

If the carrier frequency deviates from the cavity resonance, the reflected carrier beam suffers a phase shift with respect to the incident beam. Therefore, the beat between the carrier and the upper sideband (+30 MHz) and the beat between the carrier and the lower sideband (-30 MHz) are no longer 180 degrees out of phase with each other to provide perfect signal cancellation at the detector. This generates a non-zero beat signal (30 MHz) at the detector. In order to generate the error signal, the beat signal is mixed with the local oscillator to yield a DC signal. An arbitrary waveform generator (Textronics AFG3052C) is used as a local oscillator to provide a sinusoidal modulation signal to both the EOM and the mixer (Minicircuits ZAD-1-1-+). The error signal is then passed through a low pass filter (1.9 MHz) to remove all higher harmonics. The error signal is then fed into a high bandwidth (10 MHz) digital servo system (Toptica Digilock), which generates the correction signal for stabilizing the frequency of the reference laser.

Any residual amplitude modulation from the EOM creates an additional DC component in the error signal. This can be avoided if the polarization axis of the EOM matches with the optical beam. Hence a Glan Thompson polarizer (Thorlabs GTH5M-B) is used before the EOM for polarization matching.

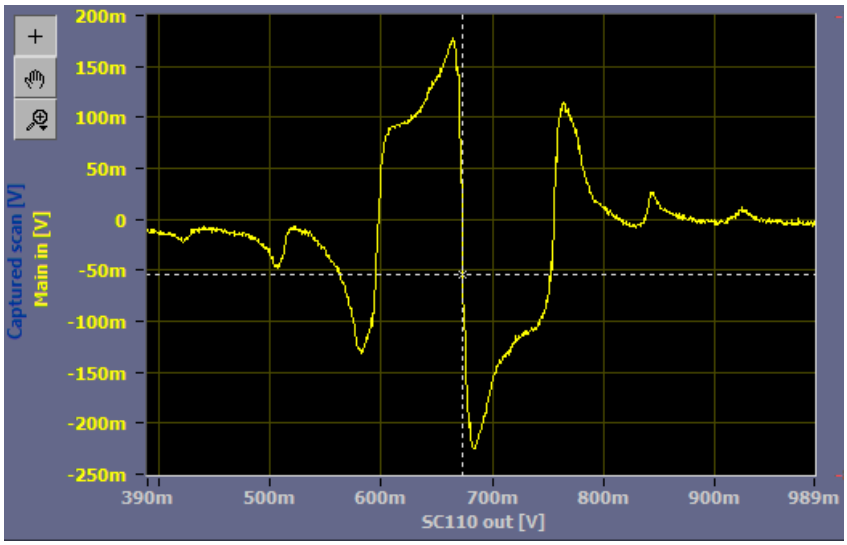

Figure 3.6 Error signal generated by the Pound Drever Hall lock.

3.2.2 Frequency Offset Lock

In our optical setup, the ν_1 laser is locked to the reference laser by a frequency offset lock. As explained earlier in this section, the ν_1 beam needs to have wide tunability. The frequency offset lock method is chosen as it provides wide tunability and large capture range [Sch99].

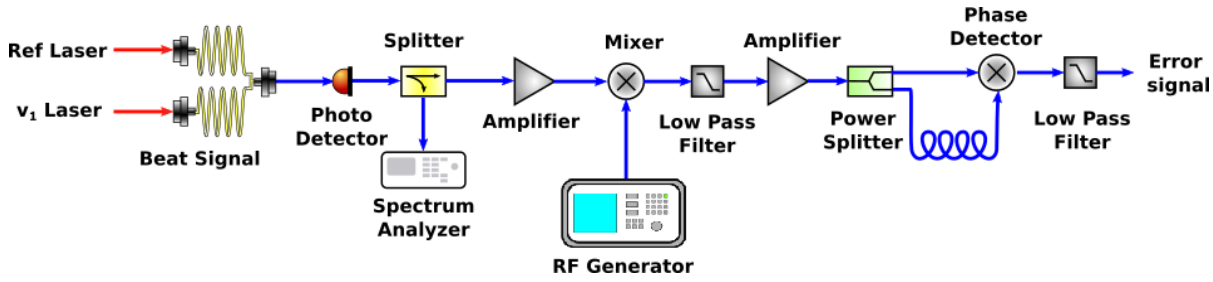

Figure 3.7 Schematic of frequency offset lock for the ν_1 laser

Fig. 3.7 shows the setup for the frequency offset lock. The optical beams from the ν_1 and reference lasers are fiber coupled into a high bandwidth photo-detector (EOT ET-4000AF). A high bandwidth (9 GHz) detector is used as the optical transition for $|\nu = 38\rangle$ to $|\nu' = 64\rangle$ state is 3 GHz away from the molecular resonance of the Iodine. The beat signal generated

by the photo-detector is observed on the spectrum analyzer after passing through a splitter (Mini-Circuits ZFRSC-42-S+). The other part of the beat signal is amplified by an amplifier (ZJL-4HG+). The amplified signal is then mixed with the local oscillator. The output of the mixer (ZX05-30W-S+) is passed through the low pass filter (BLP-150+) and amplified (ZKL-2+) again. The amplified signal is now split into two using a power splitter (ZFRSC-2050+).

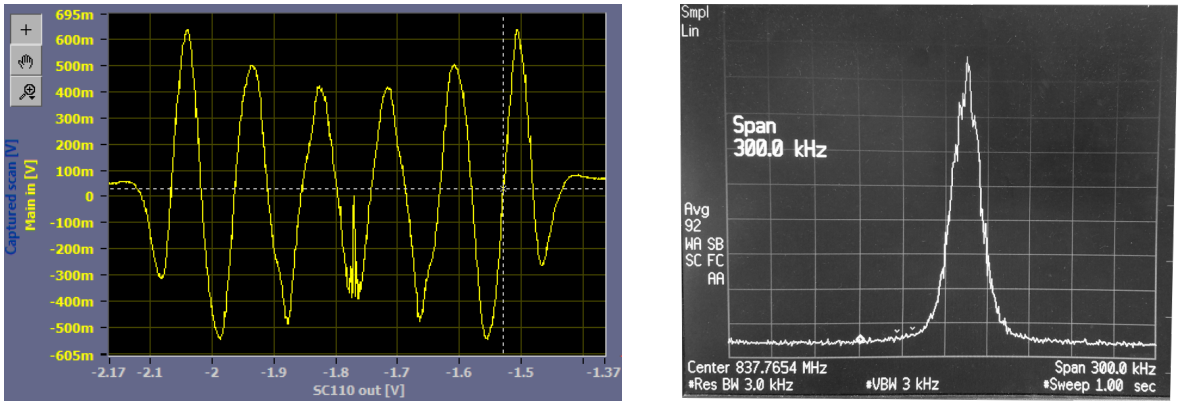

(a) **(b)**

Figure 3.8 (a) Error signal of frequency offset lock (b) Beat signal between reference laser and ν_1 laser

One part of the signal goes to the phase detector directly while the other part is sent through a delay line (4 m) before reaching phase detector (ZRPD-1+). The delay line is introduced to create a phase shift in the signal reaching the mixer. Any frequency drift of the ν_1 laser changes the phase shift between the direct signal and the signal through the delay line. The output of the mixer is sent through a low pass filter (BLP-1.9+) in order to remove higher harmonics and the error signal is generated. The error signal is then sent into a high bandwidth servo system (10 MHz) to stabilize the frequency of the ν_1 laser.

Fig. 3.8a shows the error signal generated from the frequency offset lock as a function of beat frequency between the ν_1 and reference laser. The envelope on the peaks is due to the limited bandwidth of the phase detector. The zero crossings are spaced by $c/L \approx 75$ MHz, where c and L are the velocity of light and the length of the delay line, respectively. The ν_1 laser is locked to one of the several zero crossings. This locking point can be tuned by changing the frequency of the RF generator up to 1 GHz, thus providing wide tunability. In

addition, it also provides broad capture range ($c/2L \approx 37$ MHz). After locking the ν_1 laser to one of the zero crossings of the error signal, the beat signal(shown in Fig. 3.8b) between the ν_1 and reference laser is measured using a spectrum analyzer (Fig. 3.8b) at a measurement bandwidth of 3 kHz and a sweep time of 1 second. Since the span range in Fig. 3.8b is 300 kHz (Each horizontal box = 30 kHz), we can conclude that the lock stability between ν_1 and reference laser is less than 30 kHz.

3.2.3 Saturation Absorption Spectroscopy

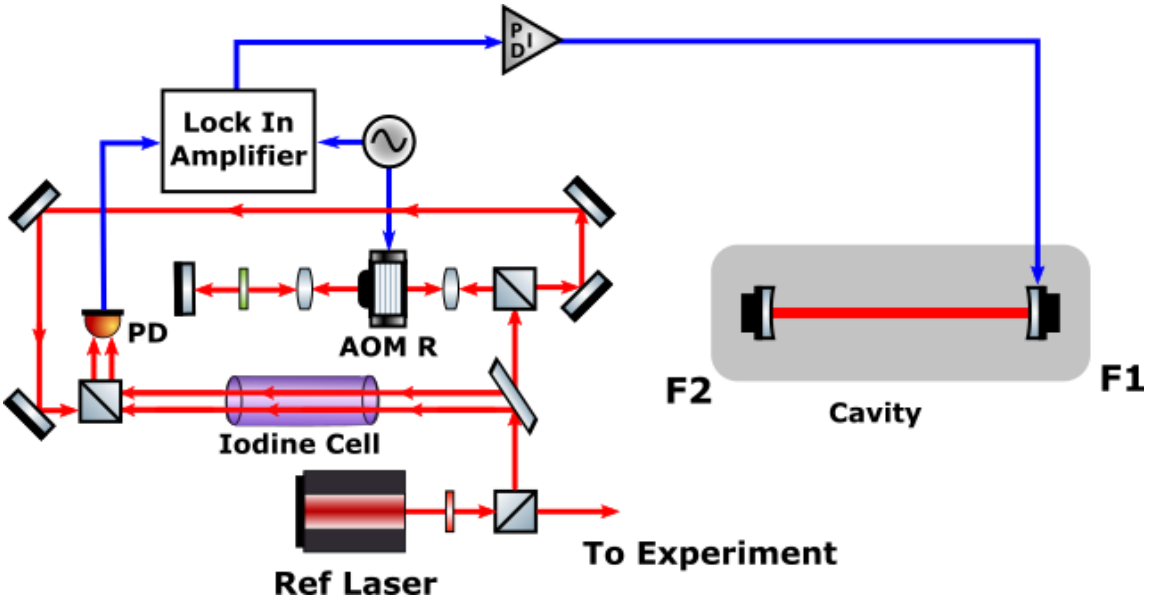

Figure 3.9 Schematic of saturation absorption spectroscopy setup

In the previous section, we saw how the reference and ν_2 lasers are locked to the cavity. But the cavity itself can drift due to mechanical and thermal vibrations. Hence the cavity needs to be locked to a stable reference source. In our optical setup, the cavity is locked to one of the iodine peaks. The saturation absorption spectroscopy setup shown in Fig. 3.9 is used to generate error signal shown in Fig. 3.10.

A 30 mW beam from the reference laser is sent through a 90/10 beam splitter plate. 90% of the power is transmitted (pump beam) through the beam splitter and rest of the power is reflected from the front and back surface of the beam splitter. The two reflected (probe)

beams are then passed through an iodine cell and collected on a balanced photo-detector (Thorlabs PDB210A). The pump beam is double passed through an AOM, which increases the frequency by +236 MHz. The AOM also modulates the frequency of the pump beam. An Agilent 33210A function generator provides the modulation signal to the AOM with a V_{pp} of 3 Volts (9 MHz) at 33 kHz. The pump beam is then aligned to counter propagate and overlap with one of the probe beams.

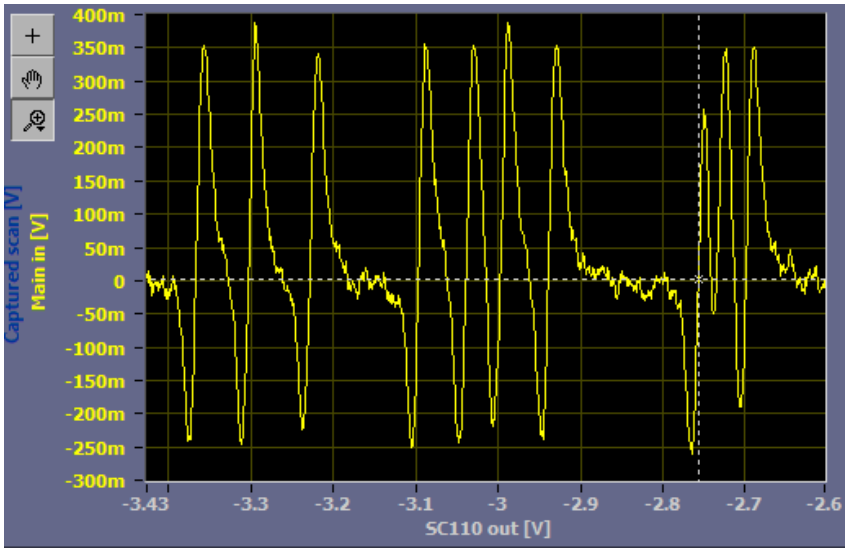

Figure 3.10 Error Signal from the saturation absorption spectra

Both of the probe beams A and B interact with the iodine molecules. The absorption spectra of probe beam A is Doppler broadened, whereas for probe beam B it is *Doppler-free* due to the overlap of a strong counter-propagating pump beam that interacts with the same velocity group. This burns a hole in the Doppler broadened absorption spectra and facilitates the observation of narrow molecular transitions in iodine molecules. Both the probe beams are incident on a balanced detector which subtracts the signals. The photo-detector's output along with the modulation signal to the AOM are sent to the lock-in amplifier. The lock-in amplifier generates a discriminator error signal shown in Fig. 3.10. The cavity is locked to one of the zero crossings by a home built servo.

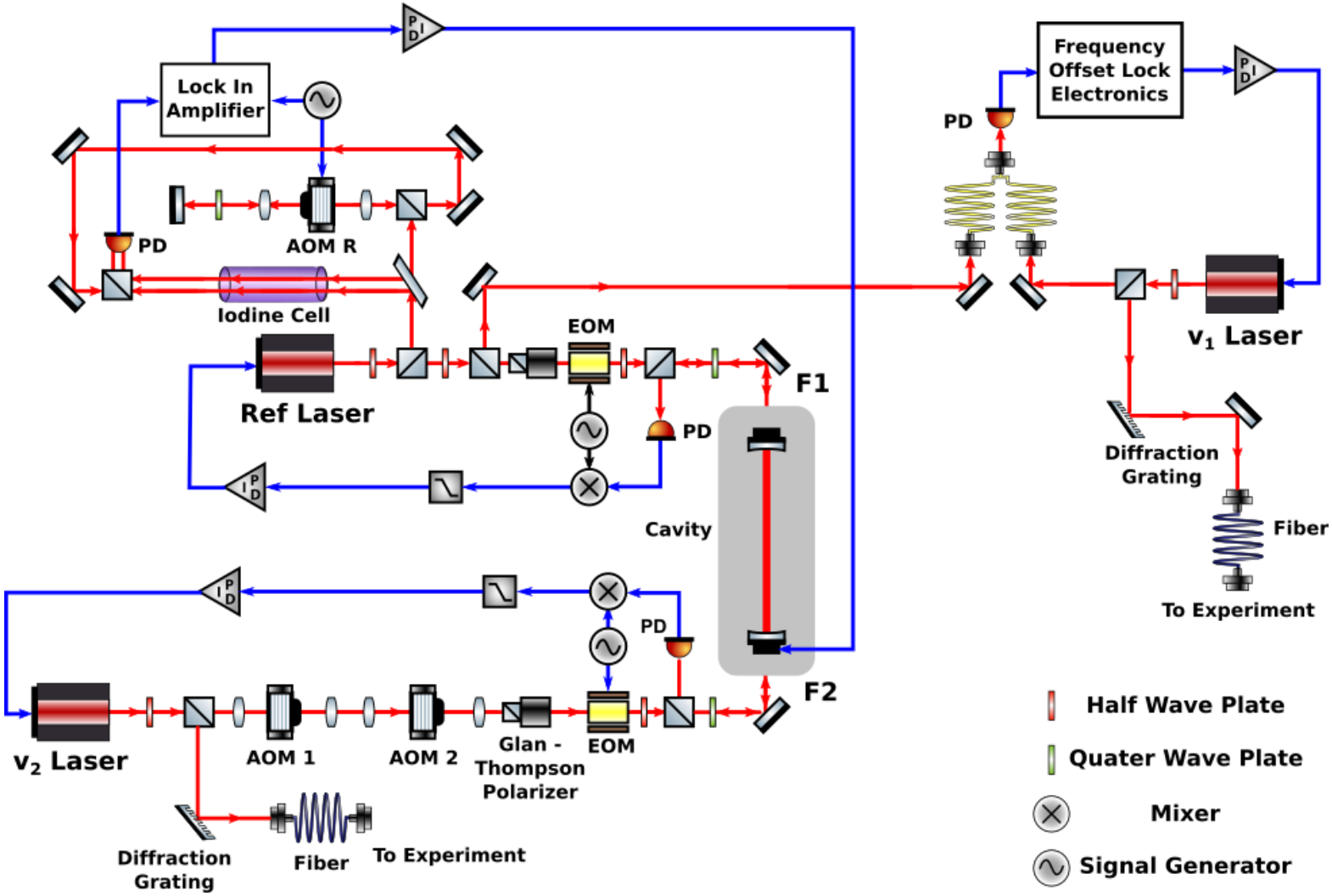

Figure 3.11 Schematic of two-field optical control system.

Having discussed the different parts of our optical control setup, the full schematic is shown in Fig. 3.11. In summary, ν_2 and reference lasers are locked to the cavity and the cavity is locked to an iodine peak. The ν_1 laser is locked to the reference laser. The reference laser beam is split into three parts; one part goes to the cavity for PDH lock, another part goes to the beat signal for frequency offset lock and another part to the saturation absorption spectroscopy for the cavity lock. Also, a part of the ν_2 laser beam is sent to the cavity and the rest is sent to the main chamber. Similarly, the ν_1 laser beam is sent to generate the beat signal for the frequency offset lock and to the main chamber.

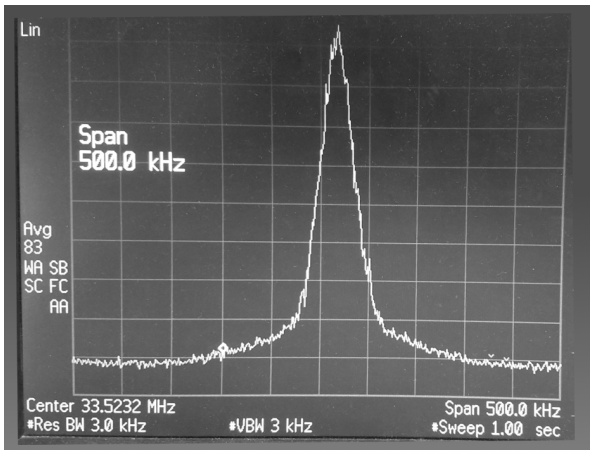

Figure 3.12 Beat Signal between ν_1 and ν_2 Lasers

After locking all three lasers and the cavity, the beat signal between ν_1 and ν_2 laser was measured and is shown in Fig. 3.12. The measurement settings used are 3 kHz measurement bandwidth, 1 second sweep time and 500 kHz span range. The beat shown in Fig. 3.12 is an average of 100 scans swept for 1 second each. Fig. 3.12 illustrates that the overall frequency stability between the ν_1 and ν_2 laser is less than 50 kHz.

As shown in Fig. 3.11, the optical beams are sent to the experiment after passing through the diffraction grating (Opti Grate BPF-677). The diode lasers (Toptica TA pro), which generates ν_1 and ν_2 optical beams, has a tapered amplifier with a wide spectral bandwidth. The tapered amplifier in addition to amplifying the ν_1 and ν_2 frequency also amplifies the atomic transition frequency (670.9 nm). Hence when the optical beams illuminate the atoms, there is an additional loss due to the resonant atomic transition. This loss is

eliminated by incorporating the diffraction grating in our optical setup. The bandwidth of the diffraction grating is approximately 0.1 nm and hence it acts as a wavelength filter.

3.3 Measurement of Optical Frequencies and Rabi Frequencies

In this section, I will discuss the frequency measurement for our optical transitions. I will also discuss the calibration of Rabi frequencies Ω_1 and Ω_2 of the ν_1 and ν_2 beams.

3.3.1 Measurement of ν_1 Beam Frequency

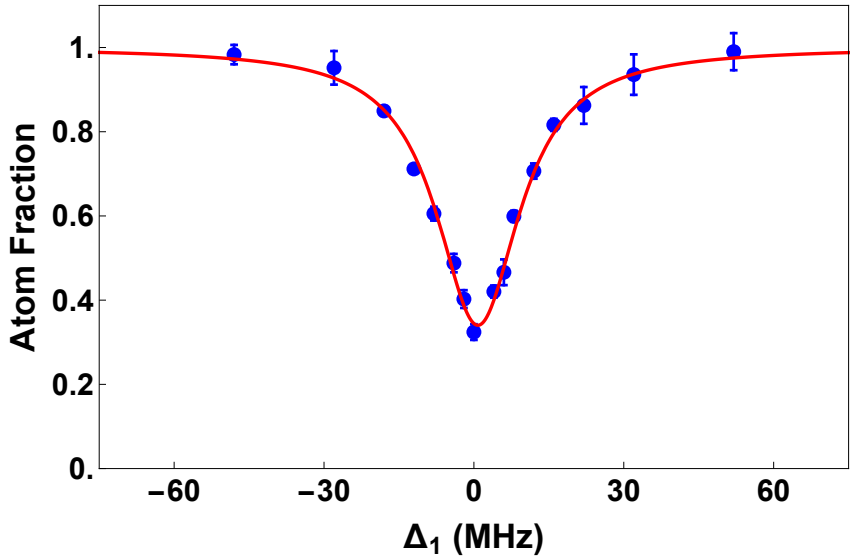

Figure 3.13 Atom loss spectra as a function of single photon detuning at B = 840 G, without the ν_2 beam. Blue Dots: Measured atom fraction. Solid Red line: Fit to continuum-dressed state model.

In this section, the method used to find the optical frequency for the $|g_1\rangle$ to $|e\rangle$ transition will be discussed. As shown in Fig. 3.3, $|\nu = 38\rangle$ is used for the ground molecular state $|g_1\rangle$ and $|\nu' = 64\rangle$ for the excited molecular state $|e\rangle$. For ^{6}Li, near the broad resonance, the triplet state $|T, k\rangle$ is mixed with the ground molecular state $|g_1\rangle$ due to strong hyperfine

coupling. Hence, when the ν_1 beam is resonant with the $|T,k\rangle - |e\rangle$ transition, atom loss occurs.

To measure the transition frequency, evaporative cooling is performed at 832 G with a 50-50 mixture of atoms in state $|1\rangle$ and $|2\rangle$. The magnetic field is then swept to 840 G and allowed to stabilize for 3 seconds. The ν_1 beam is then turned on for 5 ms. After the ν_1 beam is turned off, atoms in state $|1\rangle$ are imaged immediately. The remaining atom fraction from the image is plotted as a function of single photon detuning, Δ_1 and shown in Fig. 3.13. The frequency at which the peak loss occurs is the resonant frequency for $|\nu = 38\rangle$ to $|\nu' = 64\rangle$ at 840 G and is measured to be,

$$\nu_1\,(38 \rightarrow 64) = 444.1401 \pm 0.0002\,\text{THz}. \tag{3.4}$$

3.3.2 Measurement of ν_2 beam frequency

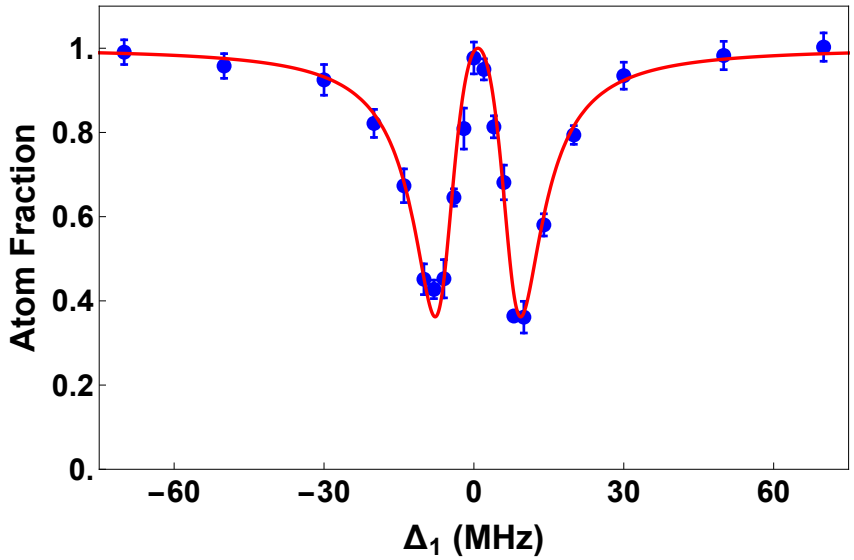

Figure 3.14 Atom loss spectra as a function of single photon detuning at B = 840 G, and $\Delta_2 = 0$. Blue Dots: Measured atom fraction. Solid Red line: Fit to continuum-dressed state model

The ν_2 beam couples the state $|\nu = 37\rangle$ to $|\nu' = 64\rangle$. When the ν_1 beam is on, atoms in triplet state $|T\rangle$ are excited to the singlet excited state $|e\rangle$. This results in atom loss. But when both ν_1 and ν_2 beams are on, the transition probability amplitudes destructively interfere

with each other. Due to the destructive quantum interference, absorption is inhibited and a transparency window in the absorption spectrum is created. If the ν_2 beam is on resonance, the transparency window will be at the center of the atom loss peak.

To measure the transition frequency, a 50-50 mixture of atoms in state $|1\rangle$ and $|2\rangle$ are evaporatively cooled at 832 G. The magnetic field is then swept to 840 G and allowed to stabilize for 3 seconds. The ν_2 beam is first turned on for 100 ms, to collect all the atoms in the additional attractive potential created by the ν_2 beam due to its high intensity. The ν_1 beam is then turned on for 5 ms. After the ν_1 beam is turned off, atoms are imaged immediately. The atom fraction from the image is plotted as a function of single photon detuning, Δ_1 (by changing ν_1 and holding ν_2 constant) is shown in Fig. 3.14. The resonant ν_2 frequency is measured to be,

$$\nu_2\,(37 \rightarrow 64) = 444.1965 \pm 0.0002\,\text{THz}. \tag{3.5}$$

3.3.3 Calibration of Rabi Frequency Ω_1 of ν_1 beam

As explained in Chapter 2, near the narrow resonance, the ν_1 beam Ω_1 can shift the position of ground state $|g_1\rangle$. The light shift Σ of the state $|g_1\rangle$ is proportional to $-\Omega_1^2/4\,\Delta_1$. The Rabi frequency Ω_1 is proportional to the intensity I of the ν_1 beam,

$$\Omega_1 = 2\,\pi \times c_1\,(\text{MHz}) \times \sqrt{I} \tag{3.6}$$

where c_1 is the proportionality constant and depends on the transition strength. The intensity I,

$$I = \frac{2\,P}{\pi\,\omega_0^2} \tag{3.7}$$

where P and ω_0 are the power and the beam waist of the ν_1 beam. The beam waist of the ν_1 beam is 750 μm. The Rabi frequency Ω_1 can be calibrated by measuring the light shift of the ground state $|g_1\rangle$ for different intensity of the ν_1 beam.

The experimental sequence for calibrating Ω_1 is as follows. Atoms are cooled at 300 G and the magnetic field is swept to the field of interest B. The ν_1 beam with an intensity I is then applied for 5 ms. The atoms are imaged immediately after the ν_1 beam is turned off. Fig. 3.15 shows atom loss as a function of magnetic field B. The narrow peak in Fig. 3.15 corresponds to the position of ground state $|g_1\rangle$. The intensities of the ν_1 beam used to generate Fig. 3.15 (a),(b) and (c) are 7.35 mW/mm^2, 13.58 mW/mm^2, 24.9 mW/mm^2 respectively. The solid

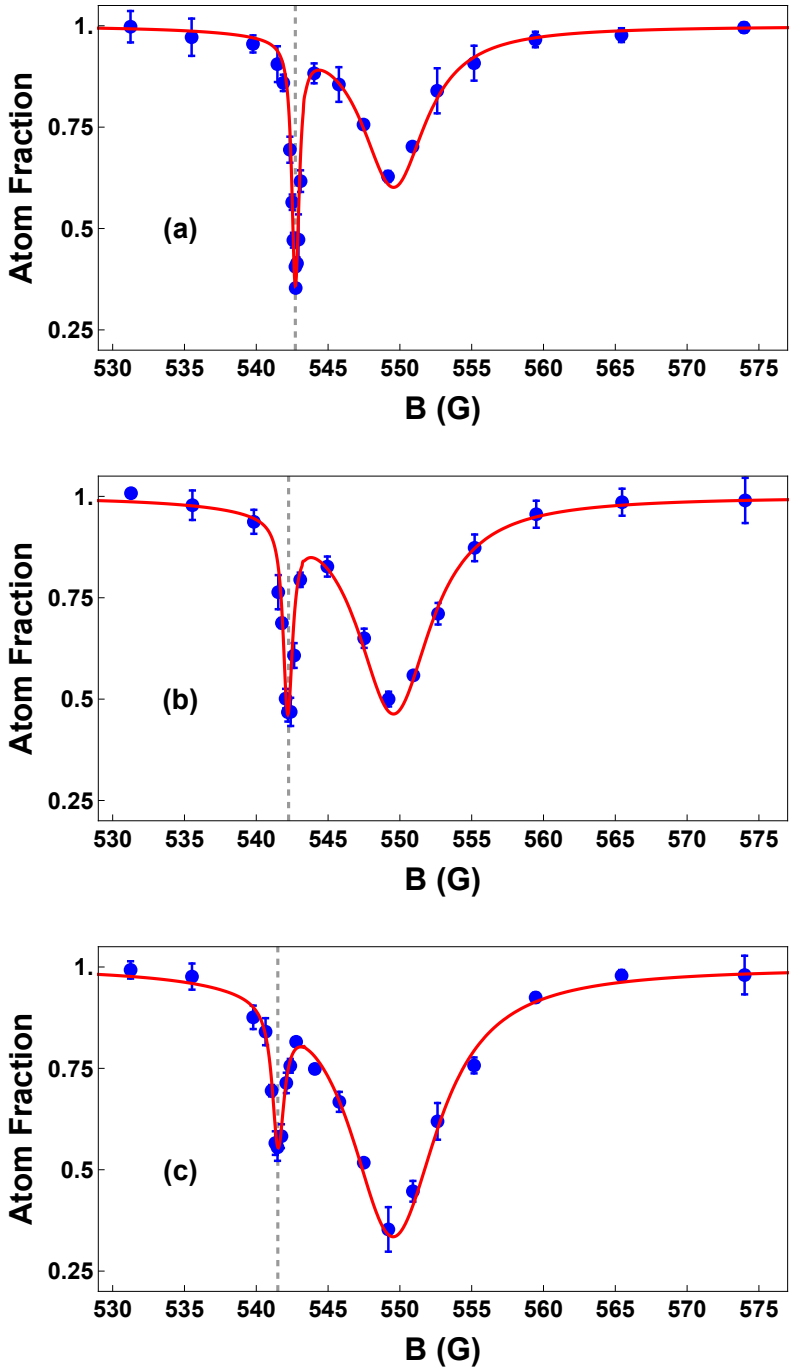

Figure 3.15 Atom loss spectra as a function of magnetic field when $\Delta_1 = 18.84$ MHz, in the absence of ν_2 beam. The ν_1 laser intensities used to generate (a), (b) and (c) are 7.35 mW/mm^2, 13.58 mW/mm^2, 24.9 mW/mm^2 respectively. Blue Dots: Measured atom fraction. Solid Red line: Fit to continuum-dressed state model.

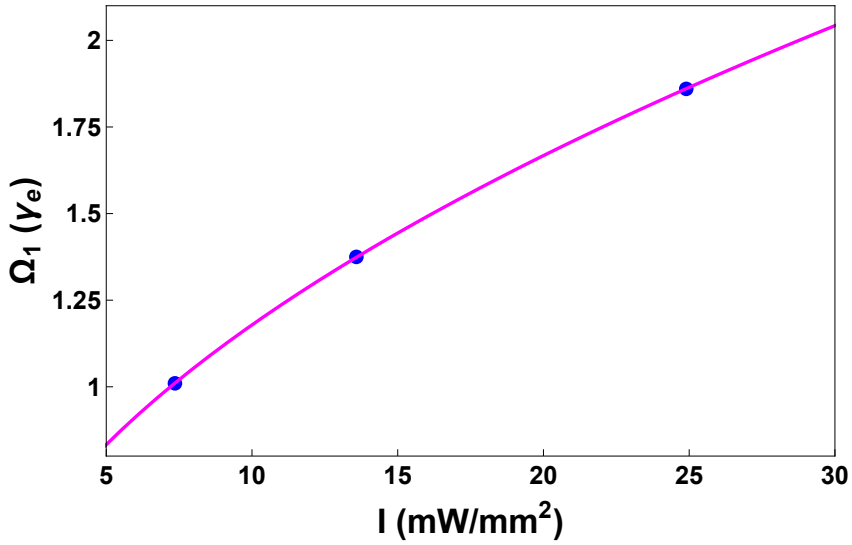

Figure 3.16 Intensity of ν_1 laser versus calculated Rabi frequency in the units of γ_e. Blue dots: Measured Rabi frequency from Fig. 3.15. Solid Magenta Line: Fit to Eq. 3.6.

red lines in Fig. 3.15 are the results of the continuum-dressed state model explained in Chapter 2. From the model, the Rabi frequencies are determined for the applied intensities and is plotted in Fig. 3.16 (blue dots). The measured Rabi frequencies Fig. 3.16 (blue dots) are then fitted with Eq. 3.6, Fig. 3.16 (magenta line). From the fit, we get

$$c_1 = 4.4\,\text{MHz}. \tag{3.8}$$

The Rabi frequency Ω_1 can also estimated from the predicted electric dipole transition matrix element. For the $v = 38 \rightarrow v' = 64$ transition, the predicted oscillator strength is $f_{eg} = 0.025$ [Rob95]. The corresponding Rabi frequency is

$$\Omega_1 = 2\pi \times 4.77\,\text{MHz}\sqrt{I}, \tag{3.9}$$

where I is the intensity of the optical beam given in mW/mm^2. Comparing Eq. 3.9 with Eq. 3.6, we get

$$c_1 = 4.77\,\text{MHz}, \tag{3.10}$$

which is in good agreement with the measured value of 4.4 MHz.

3.3.4 Calibration of Rabi Frequency Ω_2 of the ν_2 beam

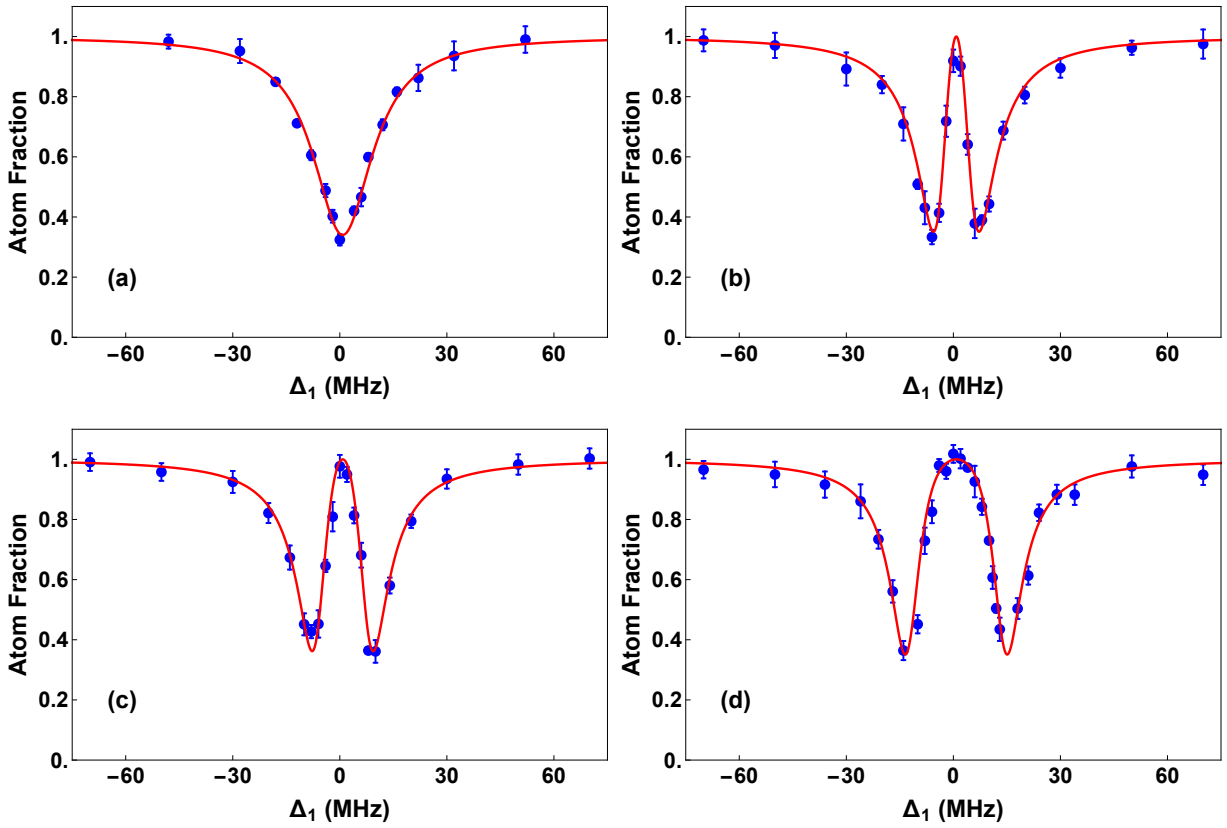

Figure 3.17 Atom loss spectra as a function of single photon detuning, Δ_1, at B = 840 G, when Δ_2 = 0. The ν_2 laser intensities used to generate (a), (b), (c) and (d) are 0 mW/mm^2, 102 mW/mm^2, 183 mW/mm^2, 509 mW/mm^2 respectively. Blue Dots: Measured atom fraction. Solid red line: Fit to continuum-dressed state model.

When the ν_1 beam is on resonance with the $|T,k\rangle$-$|e\rangle$ transition, atom loss occurs. But when both the ν_1 beam and ν_2 beams are at resonance, a transparency window in absorption is created due to quantum interference. The width of the transparency window is dependent on the Rabi frequency Ω_2 of ν_2 beam. Ω_2 is written as,

$$\Omega_2 = 2\pi \times c_2\,(\mathrm{MHz}) \times \sqrt{I} \tag{3.11}$$

where c_2 is the proportionality constant which depends on the transition strength , and I is the intensity of the beam.

Atoms are cooled at 840 G and the ν_2 beam is applied for 100 ms. The ν_1 beam is then turned on for 5 ms and the atom fraction is measured as a function of two-photon detuning δ, by changing the ν_1 beam frequency ν_1 and holding the ν_2 beam frequency ν_2 constant. Fig. 3.17 shows the atom fraction as a function of two-photon detuning δ for different values of Intensity I of the ν_2 beam. The solid red lines are the results of the continuum-dressed state model explained in Chapter2, from which the measured Rabi frequencies are determined. The intensities of ν_2 beam used in Fig. 3.17 (a), (b), (c) and (d) are 0 mW/mm^2, 102 mW/mm^2, 183 mW/mm^2, 509 mW/mm^2, respectively. Fig. 3.18 (blue dots) shows the measured Rabi frequencies Ω_2 (blue dots) as a function of laser intensity I. The measured Rabi frequencies Fig. 3.16 (blue dots) are then fitted with equation 3.6, Fig. 3.16 (magenta line). From the fit, we get

$$c_2 = 1.26\,\text{MHz}. \tag{3.12}$$

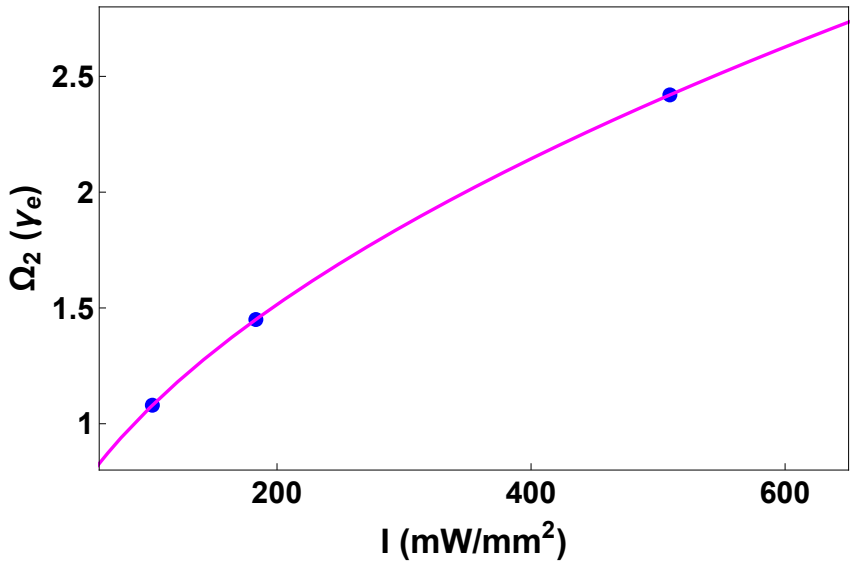

Figure 3.18 Intensity of ν_2 laser versus Rabi frequency in units of γ_e. Blue dots: Measured Rabi frequency from Fig. 3.17. Solid Magenta Line: Fit to Eq. 3.11.

For the $v = 37 \rightarrow v' = 68$ transition, the predicted oscillator strength is $f_{eg} = 1.98 \times$

10^{-3} [Rob95]. The corresponding Rabi frequency is

$$\Omega_2 = 2\pi \times 1.34\,(\text{MHz})\sqrt{I}, \tag{3.13}$$

Comparing Eq. 3.13 with Eq. 3.11, we get

$$c_2 = 1.34\,\text{MHz}, \tag{3.14}$$

which is in good agreement with the measured value of 1.26 MHz.

3.4 Calibration of the Radio-Frequency (RF) Antenna

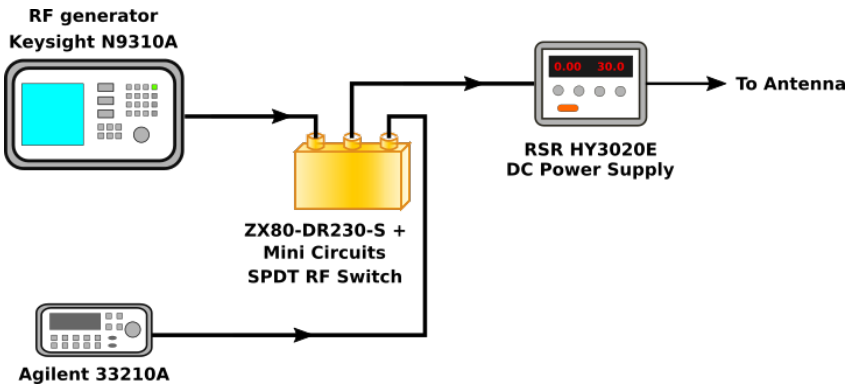

Figure 3.19 Electronics setup for the radio frequency antenna

In all our experiments, Atoms are created in the lowest two hyperfine states, $|1\rangle$ and $|2\rangle$. The energy difference between the hyperfine levels is in the radio frequency range. Hence by applying an RF signal to the antenna present inside the vacuum chamber, the atom population in the hyperfine states of ^{6}Li can be manipulated.

The RF antenna is primarly used for the following purposes,

(i) to create a 50-50 mixture of atoms in the two lowest hyperfine states $|1\rangle$ and $|2\rangle$

(ii) to perform RF spectroscopy by making transitions between the hyperfine states $|1\rangle$, $|2\rangle$, and $|3\rangle$.

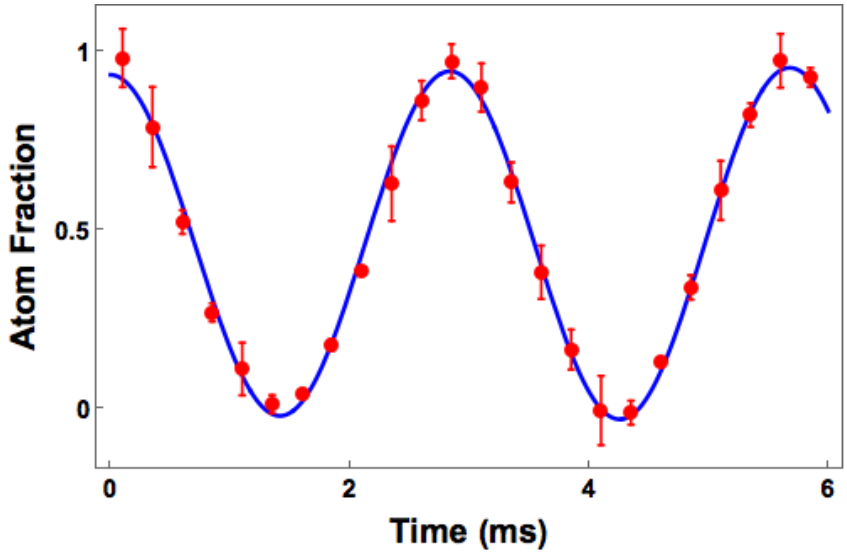

(a)

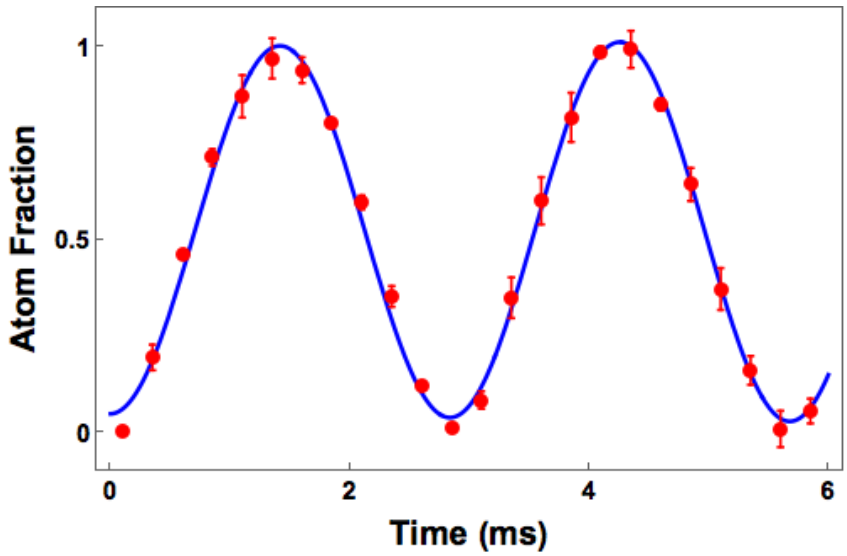

(b)

Figure 3.20 Rabi oscillation of the states $|1\rangle$ and $|2\rangle$. (a) and (b) atom fraction in state $|1\rangle$ and $|2\rangle$ respectively.

Fig. 3.19 shows the electronics setup used in our RF experiments. In order to create an equal spin mixture of states $|1\rangle$ and $|2\rangle$, a noisy sine wave of frequency 7.5 MHz at 8 G is applied by an Agilent 33210A signal generator for 1 second.

In order to perform RF spectroscopy, a Keysight N9310A RF generator generates the RF signal for atom transfer between two hyperfine states. The signals from both the Agilent and Keysight generators are sent to an RF switch (Mini-Circuits ZX80-DR230-S+ SPDT), which selects the output based on the experiment. The output of the switch is then amplified by an RF amplifier (RSR HY3020E) and the amplified signal is sent to the antenna inside the vacuum chamber.

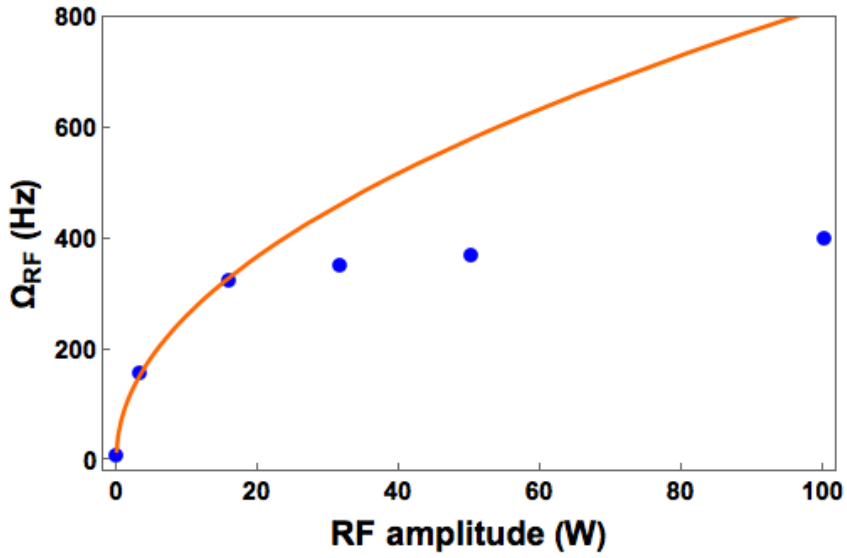

Figure 3.21 Rabi Frequency of the antenna as a function of the amplitude of RF signal

The calibration of the RF antenna involves the determination of the RF amplitude corresponding to the Rabi frequency Ω_{12} for the transition from the hyperfine state $|1\rangle$ to the hyperfine state $|2\rangle$. To calibrate the RF antenna, Atoms are cooled in the lowest hyperfine state $|1\rangle$ and an RF pulse is applied to transfer atoms from state $|1\rangle$ to $|2\rangle$. The atom in both states $|1\rangle$ and $|2\rangle$ are then imaged. Fig. 3.20 (red dots) shows the atom fraction remaining in $|1\rangle$ (Fig. 3.20 a) and the atoms arriving in $|2\rangle$ (Fig. 3.20 b) as function of time for an RF amplitude of 31.6 W. The blue curve is a fit to an exponentially decaying sinusoidal function, $A0+(A\sin(2\pi f t)e^{-\alpha t})$, where f is the Rabi frequency of the RF transition. From the fit, we

determine the Rabi frequency $\Omega_{12} = 350$ Hz. Fig. 3.21 shows the measured Rabi frequency Ω_{12} as a function of RF power applied to the antenna and illustrates that the antenna will be in the saturation region if the RF power exceeds 40 W. This happens due to the RF amplifier saturating after it reaches its maximum output power of 100 W. Hence all our experiments are done with an RF amplitude of 31.6 W (350 Hz).

3.5 Stabilization of the Bias Magnetic Field

Optical control of a narrow Feshbach resonance requires a stable bias magnetic field. In this section, I will explain the significance of a stable magnetic field and its implementation in our system. ^{6}Li has a narrow Feshbach resonance at 543.27 G of width $\Delta B = 100$ mG. In order to explore the narrow Feshbach resonance, a magnetic field stability of at least 10 mG is essential.

3.5.1 Achieving a Stable Magnetic Field

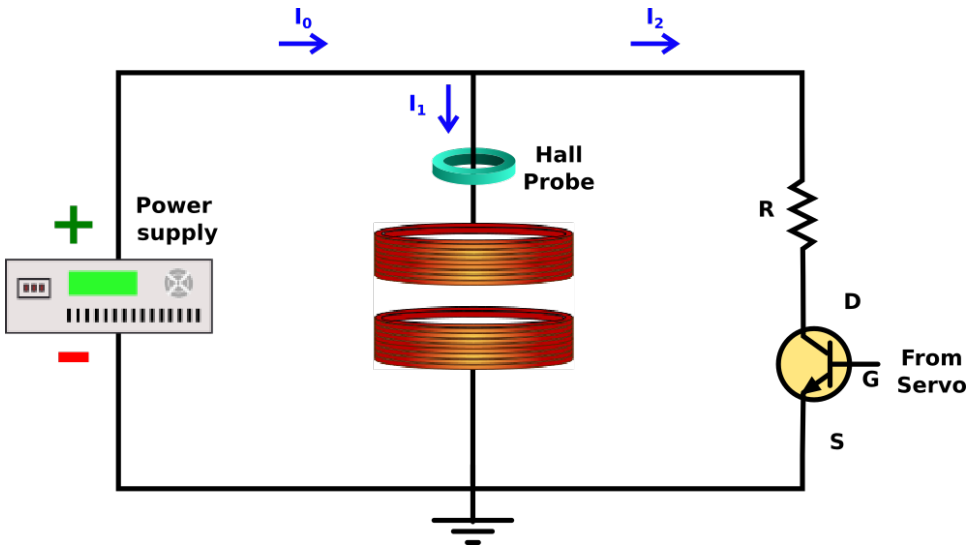

Figure 3.22 Schematic of magnetic field stabilization using a home built servo.

In our lab, Agilent 6651A power supply was initially used as the current supply for the high magnetic field coils. The current from the power supply goes to the coil through a

current sensor (LEM IT 200-S UltraStab), which measures the current through the coil. This power supply is unstable and induces a drift of 200 mG in 30 minutes, which is inadequate to investigate narrow Feshbach resonances. When we first began this project, we were left only with the choice of building a servo system to minimize the drift and thereby stabilize the magnetic field. After discussing with other research groups pursuing cold atom experiments, our power supply was upgraded to a Danfysik system 9100 power supply. This power supply was rated for a current drift of ± 10 ppm, which corresponds to a magnetic field drift of 5 mG at 500 G. However, the power supply suffered from a 60 Hz ripple with an amplitude of 100 mG (Red curve in Fig. 3.24a).

A servo controller was built to suppress the 60 Hz ripple, AC part of the current, as the drift of the DC part of the current was within the quoted range. Fig. 3.22 shows a simplistic representation of the setup to suppress the AC ripple. I_0 is the total current with the 60 Hz ripple from the power supply. I_1 and I_2 are the current that goes through the power supply and the field effect transistor (FET), respectively. The gate-source voltage (V_{gs}) of the FET is controlled by the output of the home build servo (Fig. 3.23). The current from the power supply measured by the hall probe is converted into a voltage and provided as the input to the servo. The circuit diagram of the servo is shown in Fig. 3.23. The input voltage to the servo is first AC coupled by passing through a capacitor (10 μF). The AC coupled voltage is then inverted and amplified in three stages by using op-amp circuits. In the last stage of amplification, a DC voltage adjustable by a 10 k potentiometer, is added to the amplified AC voltage. This DC voltage is chosen based on the Ohmic region of the FET (IRF510PBF) used.

The Ohmic region is linear with respect to the gate-source voltage V_{gs} for constant drain-source voltage V_{ds}, i.e. the resistance of the FET can be modified by changing the V_{gs}. Hence by controlling the V_{gs}, the ripple from I_0 can be diverted into the FET network as I_2. Since the Hall probe is actively measuring I_1, the servo generates corresponding V_{gs} to minimize the ripple in I_1. The maximum value of I_2 is set by a series resistor R (20 Ω) parallel to the power supply.

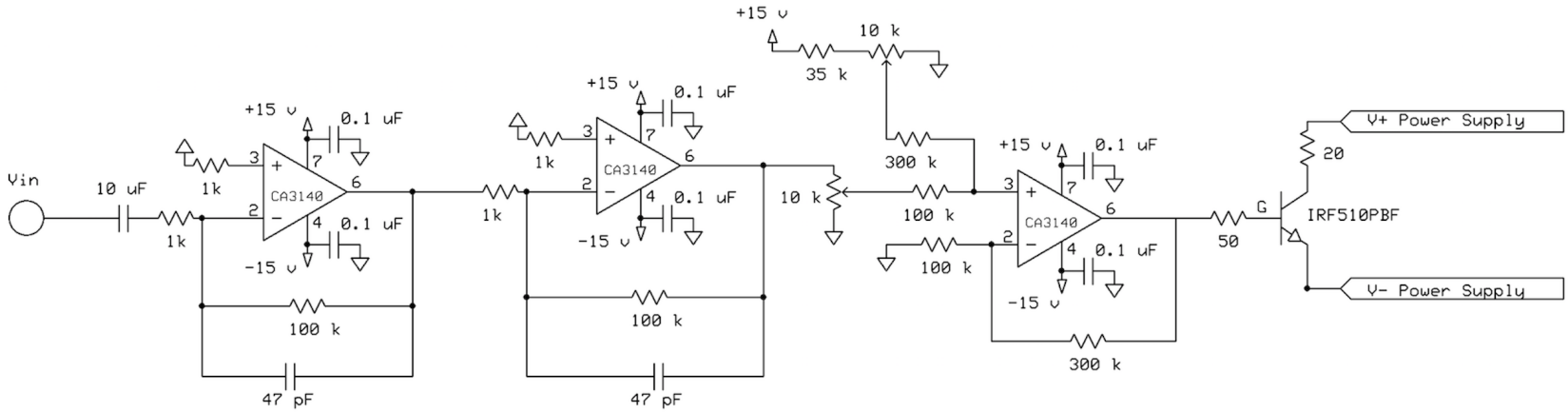

Figure 3.23 Schematic of home built servo for magnetic field stabilization.

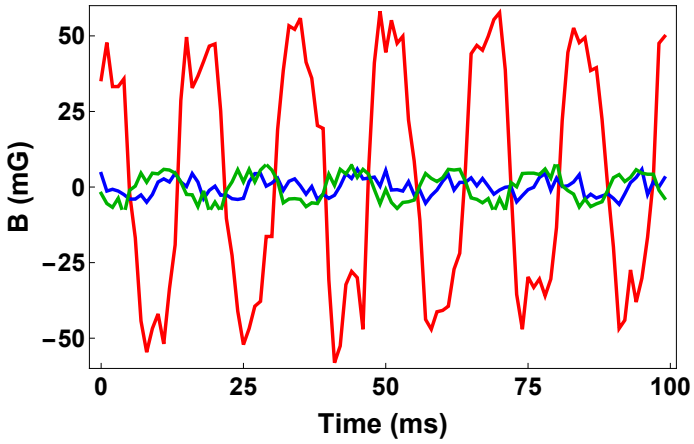

(a)

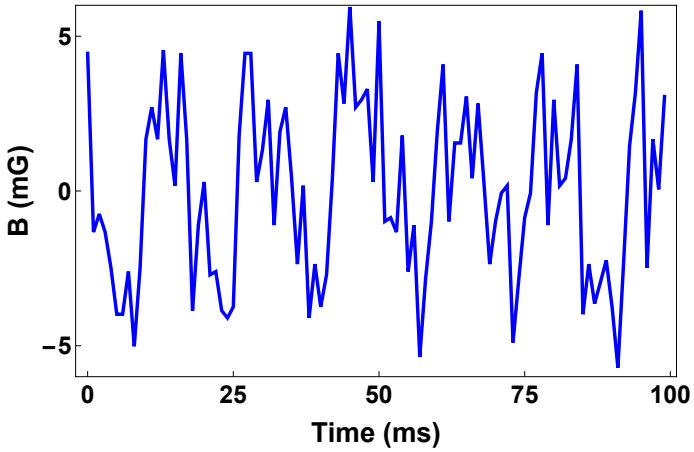

(b)

Figure 3.24 Output of the power supply in mG measured by the Hall probe. (a) Magnetic field measurement with (Blue) and without servo (Red). The power supply output when it is switched off is shown in green. (b) Expanded plot of magnetic field measurement with servo.

After implementing the servo into the magnetic coil system, the 100 mG ripple (Fig. 3.24a) was reduced to 10 mG and the repeatability of the applied current for the different cycles was within ±10 mG. The red and blue curves in Fig. 3.24a shows the AC part of the output of the power supply in mG with and without the home built servo, respectively. The green curve in Fig. 3.24a is the output when the power supply is switched off. The amplitudes of the blue and green curves are comparable as shown in Fig. 3.24a, and is limited only by the noise level in the measuring device. Fig. 3.24b is an expanded view of the blue curve (output with servo) in Fig. 3.24a, illustrating a suppressed 60 Hz ripple with an amplitude

of 10 mG. The servo controls the AC part of the current, however, there was a slow drift of the DC current (10 mG/s) due to the heating of FET network. But this effect is negligible as the duration required for a stable magnetic field in a typical experimental sequence is few milliseconds.

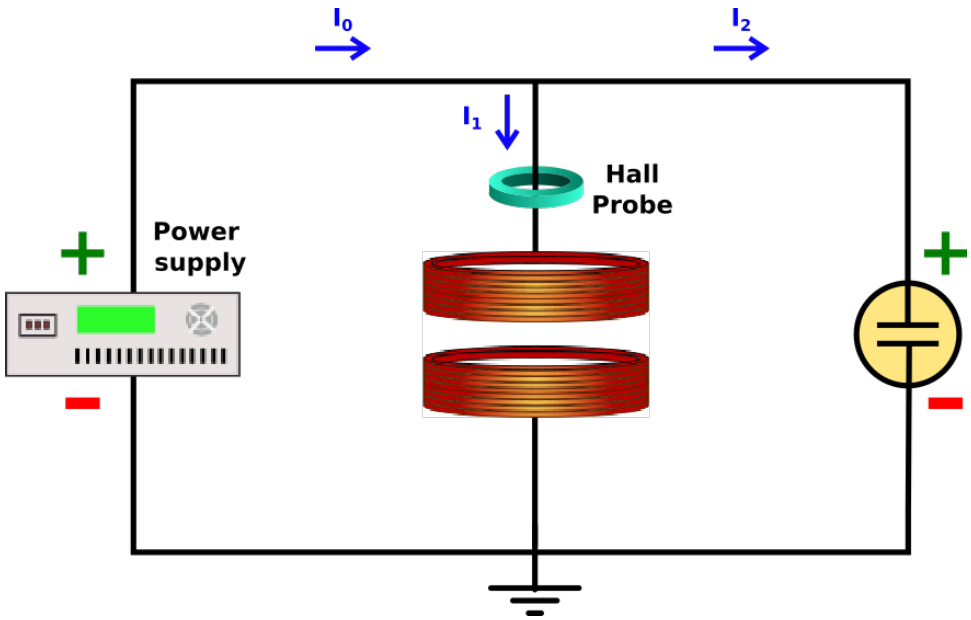

Figure 3.25 Schematic of magnetic field stabilization using a set of by-pass capacitors.

I also tried another simple technique (shown in Fig. 3.25) to remove the 60 Hz ripple in which a set of bypass capacitors connected in parallel to the coils were added. Since the noise is at low frequency, the value of the bypass capacitor has to be higher. For 60 Hz, 250 mF capacitors were used. This technique also suppressed the 60 Hz noise to the level limited by our measuring device. Fig. 3.26 shows the output of the power supply in mG for different values of capacitors. Fig. 3.26 further illustrates that the ripple from the power supply is suppressed as the capacitance is increased. When the capacitance reaches 250 mF, the amplitude of the ripple current is comparable to the noise level of the power supply when it is turned off.

The disadvantage of this technique is that the capacitors connected in parallel to the coil, increase the total time constant of the system thereby taking longer time for the current to reach its required value. This was not a significant problem since achieving a

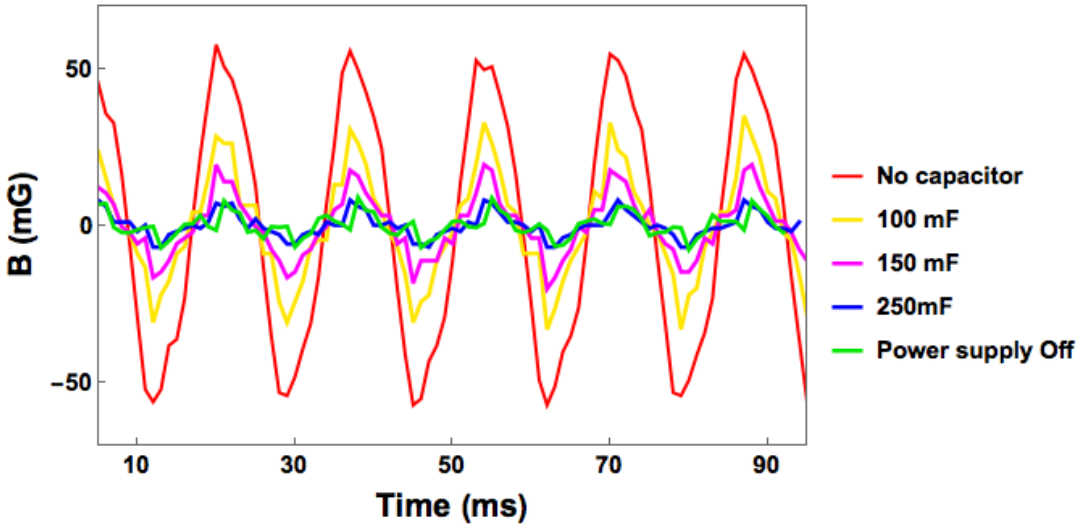

Figure 3.26 Magnetic field measurement by Hall probe for different values of by-pass capacitors.

stable magnetic field requires a wait time of 3 seconds after evaporative cooling. Now with capacitors in parallel, the wait time has to be increased to 4 seconds.

Also, after corresponding with the engineers at Danfysik about the AC ripple for two years, I finally made them fix the engineering flaw in the current supply. One of the terminals behind the power supply was not connected to the common ground causing the ground loop issue. The problem is solved by soldering the terminal to the ground through a 1 kΩ resistor.

3.5.2 Testing the Stability of Magnetic Field - RF spectroscopy

As shown in Fig. 3.24b, the noise level in the magnetic field measured by the Hall probe is 10 mG. It is not possible to conclude the stability of magnetic field from this measurement. Hence it is necessary to measure the fluctuation in the magnetic field directly by measuring its effect on the atoms. The radio frequency spectroscopy was used to test the stability of the magnetic field. As mentioned in the Section 3.4, the energy difference between hyperfine levels are in the radio frequency range. Hence applying an RF pulse can transfer atoms between states $|1\rangle$ and $|2\rangle$. Since the hyperfine energy levels are magnetic field dependent, any deviation from the calculated width of the RF transition is due to the fluctuation in the magnetic field.

Atoms are cooled at 300 G and the magnetic field is ramped to 528 G, zero crossing for

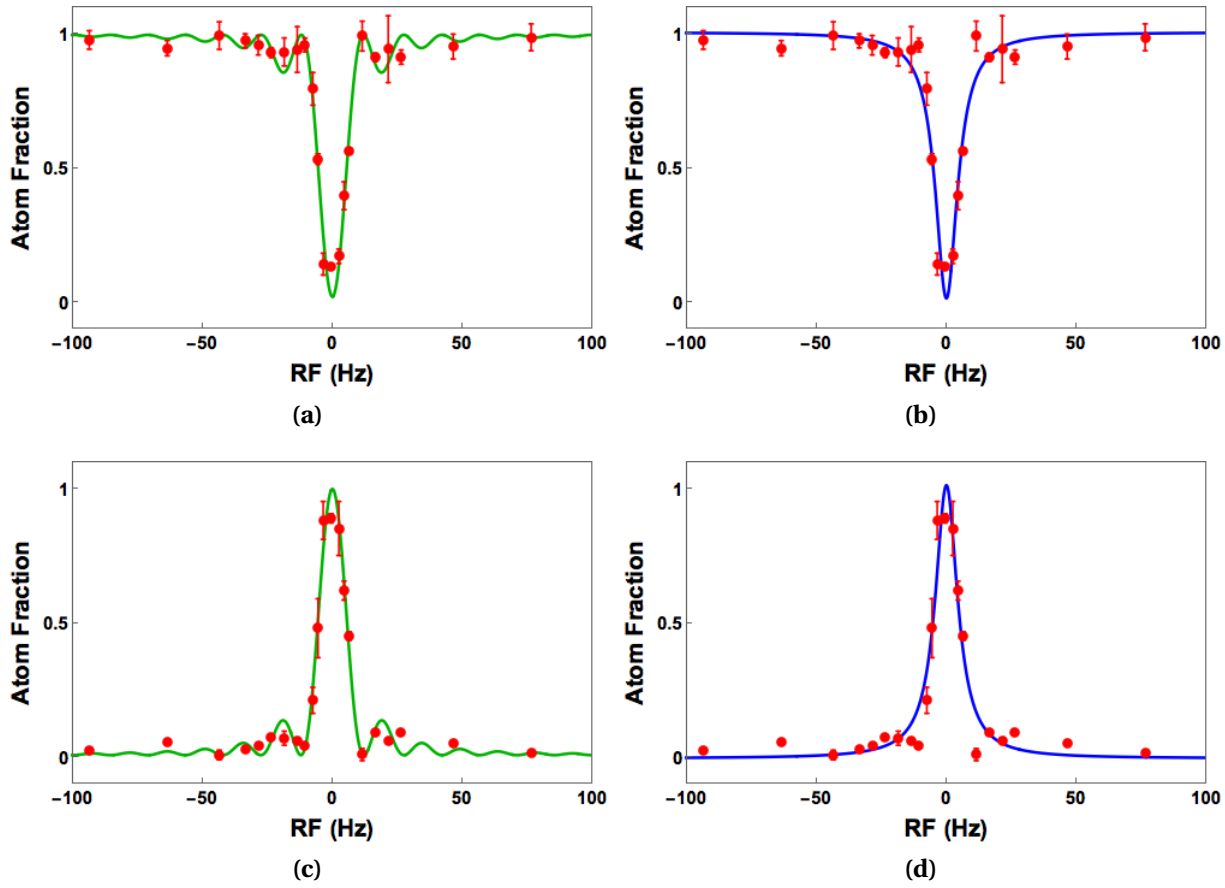

Figure 3.27 Radio frequency spectra to measure the magnetic field stability. The green curves in (a) and (c) are fit of the atom fraction (red dots) in state $|1\rangle$ and $|2\rangle$ with Eq. 3.15, respectively. (b) and (d) Lorenztian fit (blue curve) to the atom fraction (red dots) in state $|1\rangle$ and $|2\rangle$, respectively.

$|1\rangle$ - $|2\rangle$ mixture. At 528 G, an imaging optical pulse is applied to remove the atoms in state $|2\rangle$. With atoms only in state $|1\rangle$, the magnetic field is ramped to 531 G. At 531.189 G, an RF pulse is applied for the $|1\rangle$ - $|2\rangle$ transition for 70 ms with an amplitude of 7.1 Hz and image the atoms remaining in state $|1\rangle$ and the atoms remaining in state $|2\rangle$ as a function of RF frequency. The resulting RF spectra are shown in Fig. 3.27. The red dots in Fig. 3.27 (a),(b) and (c),(d) shows the atom fraction in state $|1\rangle$ and state $|2\rangle$, respectively.

The RF transter function [Sho90] for $|1\rangle$ - $|2\rangle$ transition is given by,

$$P(t) = \frac{\Omega_{RF}^2}{(\Omega_{RF}^2 + \Delta^2)} \sin\left(\sqrt{\frac{\Omega_{RF}^2 + \Delta^2}{\Omega_{RF}^2}}\frac{\pi t}{2}\right) \tag{3.15}$$

where Ω_{RF}, Δ, and t are the Rabi frequency, detuning and the time duration of the RF pulse. The green line in the Fig. 3.27 (a) and (c) is a fit of the data (red dots) with the RF transfer function given in equation 3.15. For t = 70 ms and $\Delta = 0$, the Rabi frequency $\Omega_{RF} = 7.5$ Hz. The Rabi frequency from the fit is in good agreement with the applied RF amplitude, 7.1 Hz.

The blue line in the Fig. 3.27 (b) and (d) is the Lorenzian function $L(\gamma, F_0)$ fit to the data(red dots) given by,

$$L(\gamma, F_0) = A_0 + A_1 \left(\frac{\gamma^2}{\gamma^2 + (F - F_0)^2} \right) \tag{3.16}$$

where γ and F_0 are the width and the resonant frequency of RF transition. After fitting the Lorentzian function $L(\gamma, F_0)$ to the data we get, $F_0 = 75.617343$ MHz and $\gamma = 10$ Hz. At 531.189 G, 10 Hz corresponds to 3 mG. Hence, the measured RF spectra illustrate that the magnetic field stability of our system is better than 3 mG.

3.6 Measuring the Trap Frequencies

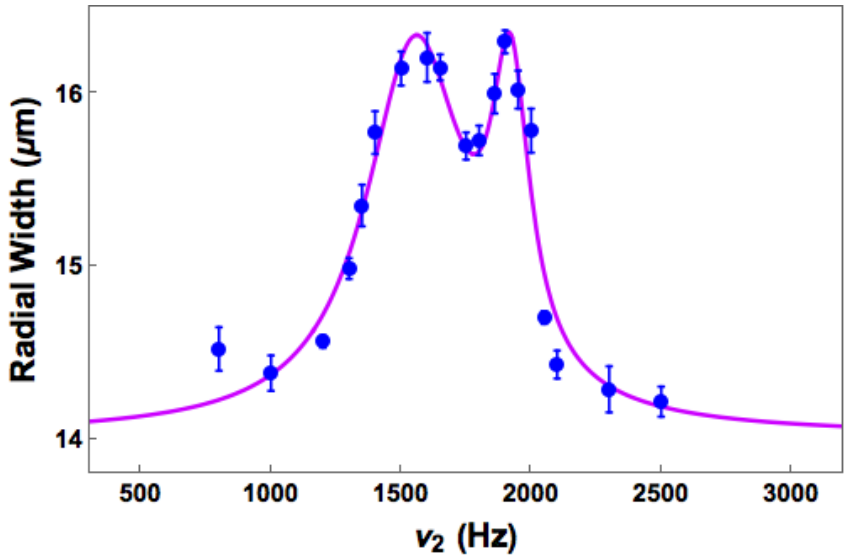

Figure 3.28 Radial width of the atom cloud as a function of modulation frequency ν_m. The largest radial width corresponds to twice the trap frequencies in the two radial direction.

The parametric resonance is used to measure the axial and radial oscillation frequencies

of the far-off resonance trap. In this method, the CO_2 trap is sinusoidally modulated by a small amplitude. This perturbation adds extra energy to the atoms in the trap and increases the mean square width of the atom cloud. The cloud width is largest when the modulation frequency ν_m is equal to twice the trap frequency.

To perform this experiment, atoms are prepared at the two lowest hyperfine state $|1\rangle$ and $|2\rangle$. After cooling the atoms at 300 G, the optical trap is re-raised to 5% trap depth. A sinusoidal modulation with an amplitude of 25 mV is then applied for 100 ms. The magnetic field is then ramped to 528 G and the atom cloud is imaged. The modulation amplitude and the duration is chosen such that the change in the width of atom cloud is approximately 10% - 15%. Fig. 3.28 shows the radial widths (magenta dots) measured from the atom cloud as the function of the modulation frequency ν_m. The radial widths (magenta dots) are then fitted with a Lorentzian function (solid line in Fig. 3.28)

$$L(\gamma_1, F_1, \gamma_2, F_2) = A_0 + A_1\left(\frac{\gamma_1^2}{\gamma_1^2+(F-F_1)^2}\right) + A_2\left(\frac{\gamma_2^2}{\gamma_2^2+(F-F_2)^2}\right), \tag{3.17}$$

where γ_1, F_1 and γ_2, F_2 are the widths and the frequencies of the two radial directions. The trap frequencies from the fit are given by,

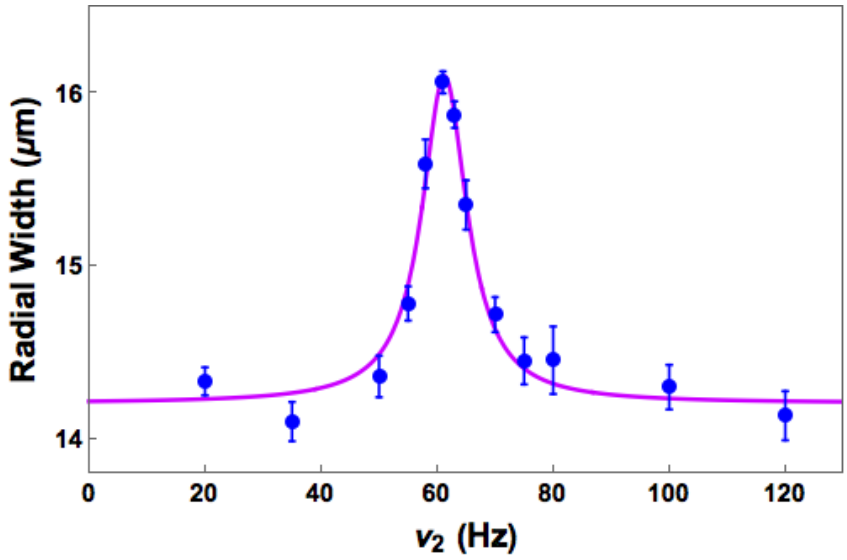

Figure 3.29 Radial width of the atom cloud as a function of modulation frequency ν_m. The largest radial width corresponds to twice the trap frequency in the axial direction.

$$\omega_x = 2\,\pi \times (777 \pm 9.5)\,\mathrm{Hz} \tag{3.18}$$

$$\omega_y = 2\,\pi \times (960 \pm 4.32)\,\mathrm{Hz} \tag{3.19}$$

Fig. 3.29 shows the plot of the radial width of the cloud when the CO_2 trap is modulated for 500 ms with the amplitude of 50 mV. The magenta dots in Fig. 3.29 are the measured radial widths from the atom cloud as a function of modulation frequency ν_m. The Lorentzian function (solid line in Fig. 3.29)

$$L(\gamma_3, F_3) = A_0 + A_1 \left(\frac{\gamma_3^2}{\gamma_3^2 + (F - F_3)^2} \right), \tag{3.20}$$

where γ_3, F_3 are the width and the resonant frequency, is then fitted to the data (magenta dots). The axial frequency from the fit is

$$\omega_z = 2\,\pi \times (30.6 \pm 0.5)\,\mathrm{Hz} \tag{3.21}$$

CHAPTER

4

EXPERIMENTS ON OPTICAL CONTROL OF INTERACTIONS IN ULTRACOLD GASES

In this chapter, I will discuss experiments that demonstrate control of scattering interactions near a Feshbach resonance using electromagnetically induced transparency (EIT). Optical control of interactions is illustrated by determining the scattering length from the measured mean-field induced frequency shifts in the radio frequency (RF) spectra. This chapter begins with a brief review of the underlying physics in optically tuning the bound states of ^{6}Li near a magnetic Feshbach resonance. In Section 4.2, measurement of mean-field energy shifts using RF spectroscopy will be discussed. Section 4.3 involves a detailed derivation of the line shapes for the RF transitions to measure mean-field shifts. The experimental results demonstrating the control of scattering length by changing the magnetic field (Section 4.4) and optical field (Section 4.5) will be presented. In addition to tuning the scattering length using optical fields, the spatial control of interactions in ultracold gases is

also demonstrated, where the scattering length is made to vary as a function of the axial position in the atomic cloud. Exploiting this spatial control, an interaction “sandwich" is achieved, where the center of the cloud is resonantly interacting and the wings of the cloud are weakly interacting. Section 4.6 involves the experimental results demonstrating spatial control of interactions in ^{6}Li gas.

4.1 Optical Control of the Scattering Length using EIT

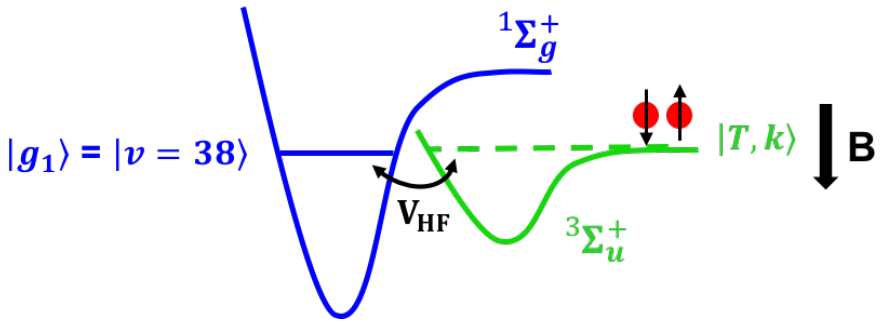

Figure 4.1 Energy level scheme for magnetic Feshbach Resonance. Colliding atoms reside in the triplet potential. The triplet continuum $|T,k\rangle$ is tuned magnetically. The triplet continuum $|T,k\rangle$ and singlet vibrational state $|g_1\rangle$ has a hyperfine coupling V_{HF}. When the triplet continuum $|T,k\rangle$ is degenerate with the singlet ground state $|g_1\rangle$, Feshbach resonance occurs.

In this section, I will give a brief overview of the underlying physics for optically tuning the Feshbach bound state $|g_1\rangle$ near a magnetic Feshbach resonance. A detailed discussion of this topic is presented in Chapter 2. Fig. 4.1 shows the energy level scheme for a magnetic Feshbach resonance. The atoms are cooled in the two lowest hyperfine states of ^{6}Li. Near a narrow Feshbach at 543.2 G, the atoms are predominantly in the triplet continuum $|T,k\rangle$. The singlet states are energetically not accessible to the atoms. The triplet continuum has a non-zero magnetic moment and can be magnetically tuned at the rate of $\propto -2\mu_B B$. The singlet vibrational state $|g_1\rangle$ has a zero magnetic moment and cannot be magnetically tuned. When the triplet continuum $|T,k\rangle$ is magnetically tuned to be energetically degenerate with the singlet vibrational state $|g_1\rangle$, a Feshbach resonance occurs due to a hyperfine coupling V_{HF} between $|T,k\rangle$ and $|g_1\rangle$. At the Feshbach resonance, the scattering cross section maximizes and the two-body scattering length diverges ($a \to \infty$). Above the Feshbach

resonance, the scattering length is negative ($a < 0$) and the interactions are attractive. Below the Feshbach resonance, the scattering length is positive ($a > 0$) and the interactions are repulsive. Thus, by magnetically tuning the triplet continuum $|T, k\rangle$ with respect to the energy of the singlet ground state $|g_1\rangle$, the scattering length can be manipulated.

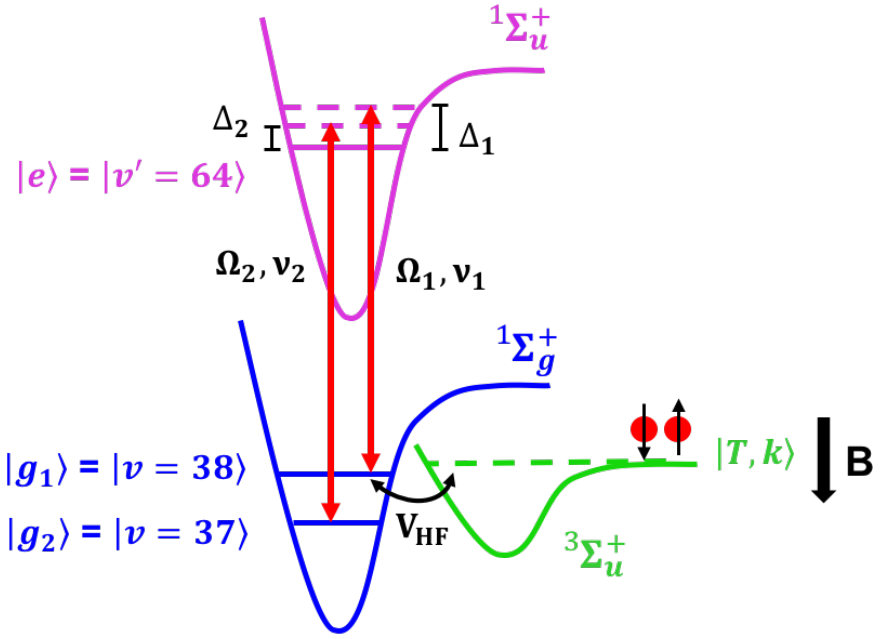

Figure 4.2 Basic level scheme for controlling interactions in ^{6}Li. Optical fields ν_1 (with Rabi frequency Ω_1 and detuning Δ_1) and ν_2 (with Rabi frequency Ω_2 and and detuning Δ_2) couple the ground molecular states $|g_1\rangle$ and $|g_2\rangle$ to the excited molecular state $|e\rangle$ of the singlet potential. The atoms are predominantly in the triplet state $|T, k\rangle$ which has an hyperfine coupling V_{HF} to state $|g_1\rangle$ causing the Feshbach resonance. The triplet state moves downward with increasing magnetic field B. For the optical control experiments in ^{6}Li, $|g_1\rangle = |v = 38\rangle$, $|g_2\rangle = |v = 37\rangle$, and $|e\rangle = |v' = 64\rangle$.

Although the singlet state $|g_1\rangle$ cannot be magnetically tuned, it can be optically tuned by inducing a light shift. In the experiments, two optical fields ν_1 and ν_2 are used to optically tune the singlet bound state $|g_1\rangle$. Fig. 4.2 shows the energy level scheme for two-field optical technique. The ν_1 beam with Rabi frequency Ω_1 and detuning Δ_1, couples the ground singlet molecular state $|g_1\rangle$ to the excited molecular state $|e\rangle$. The ν_2 beam with Rabi frequency Ω_2 and detuning Δ_2, couples the ground singlet molecular state $|g_2\rangle$ to the excited molecular

state $|e\rangle$. The presence of a single optical field ν_1 shifts the singlet ground state $|g_1\rangle$ due to the AC stark shift. This light shift is dependent on the square of the Rabi frequency Ω_1 and detuning Δ_1. When a second optical field ν_2 is applied in addition to ν_1, the position of the state $|g_1\rangle$ can be tuned by changing the frequency or intensity of either of the optical fields. In all the experiments reported in this thesis, the light shift of state $|g_1\rangle$ is controlled by varying the frequency of the ν_2 optical field and holding constant all other control parameters, such as the Rabi frequencies, Ω_1 and Ω_2, the magnetic field B, and the frequency of the ν_1 optical field.

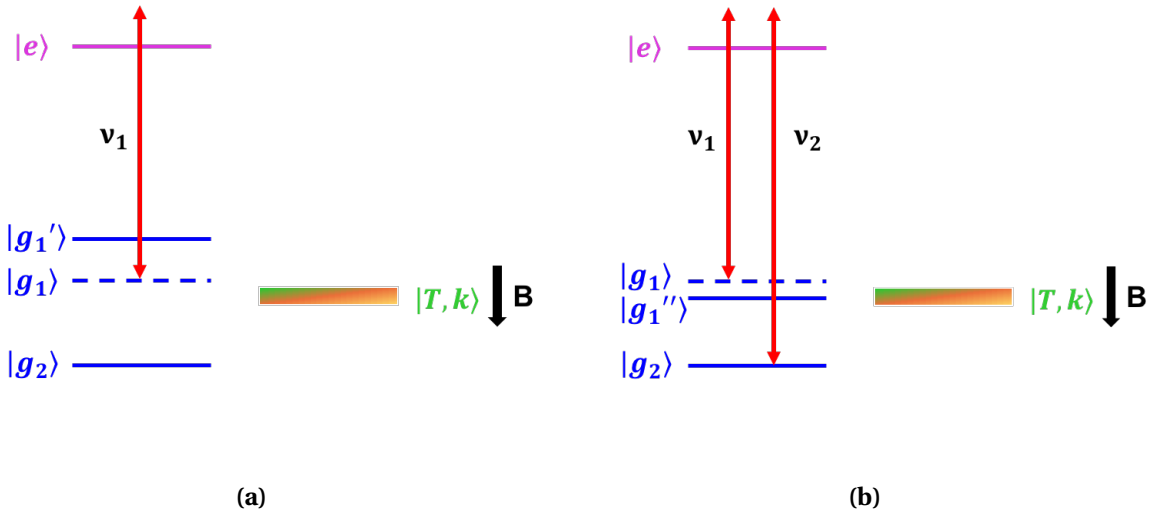

Figure 4.3 Tuning of the ground state $|g_1\rangle$. The dotted line shows the position of unshifted ground state $|g_1\rangle$. The ν_1 and ν_2 beams couple the ground molecular states $|g_1\rangle$ and $|g_2\rangle$ to the excited molecular state $|e\rangle$ of the singlet potential. The triplet state $|T,k\rangle$ is magnetically tuned near the narrow Feshbach resonance. (a) Single optical field ν_1 shifts the ground state $|g_1\rangle$ to $|g_1'\rangle$. (b) Two optical fields ν_1 and ν_2 tunes the ground state $|g_1\rangle$ to $|g_1''\rangle$.

Fig. 4.3a shows the AC stark shift of the ground state $|g_1\rangle$ by a single optical field ν_1. Fig. 4.3b shows the tuning of the ground state $|g_1\rangle$ by two optical fields ν_1 and ν_2. The dotted line in Fig. 4.3 shows the position of unshifted ground state $|g_1\rangle$. The triplet state $|T,k\rangle$ is magnetically tuned near the unshifted position of the bound state $|g_1\rangle$ (dotted line). In Fig. 4.3a, $|g_1'\rangle$ shows the position of shifted ground state due to the single optical field. In Fig. 4.3b, $|g_1''\rangle$ shows the position of shifted ground state due to two optical fields. Optical

control is achieved by tuning the light shifted state $|g_1''\rangle$ near the triplet continuum $|T,k\rangle$, thereby controlling the interactions.

From Chapter 2, the two-photon detuning δ in Hz is given by

$$\delta = (\nu_2 - \nu_1) - \left(\frac{E_{g_2}}{h} - \frac{E_T}{h}\right), \tag{4.1}$$

where ν_2 and ν_1 are the frequencies of ν_2 and ν_1 optical beams, E_{g_2} is the energy of the $|g_2\rangle$ state, and E_T is the energy of the triplet continuum $|T,k\rangle$. The two-photon detuning

$$\delta = 0, \tag{4.2}$$

happens when the difference in frequency between the two optical beams is equal to the energy difference between the $|g_2\rangle$ state and the triplet state $|T,k\rangle$. This condition is particularly interesting. When $\delta = 0$, the energy of the $|g_1\rangle$ state is returned to its original unshifted position- the position when no optical fields are applied. When $\delta < 0$, the energy of the $|g_1\rangle$ state is below the original unshifted position and when $\delta > 0$, the energy of the $|g_1\rangle$ state is above the original unshifted position. In all the experiments reported in this thesis, the two-photon detuning is varied by holding the frequency ν_1 constant and varying the frequency ν_2. All plots in the following sections, where the two-photon detuning δ is varied, implies a change in frequency ν_2 of the optical beam.

The ground state $|g_1\rangle$ can be optically tuned around its original unshifted position by varying the two-photon detuning δ. The tuning rate of the ground state $|g_1\rangle$ is dependent on the Rabi frequencies Ω_1, Ω_2 and two-photon detuning δ. Near the unshifted position, the tuning rate is given by

$$\text{Tuning Rate of } |g_1\rangle \approx \frac{\Omega_2^2}{\Omega_1^2}\,\delta. \tag{4.3}$$

4.2 Mean-Field Shift Measurement using RF Spectroscopy

In order to demonstrate two-field optical control of interaction in cold atoms, we need to establish a method to measure the interactions between atoms. In this section, I will explain in detail the RF spectroscopy technique used to measure the interaction strength.

In the experiments, the three lowest hyperfine states $|1\rangle$, $|2\rangle$ and $|3\rangle$ of ^{6}Li near 543 G are used to demonstrate this technique. Atoms are initially prepared only in state $|3\rangle$. Fig. 4.4a

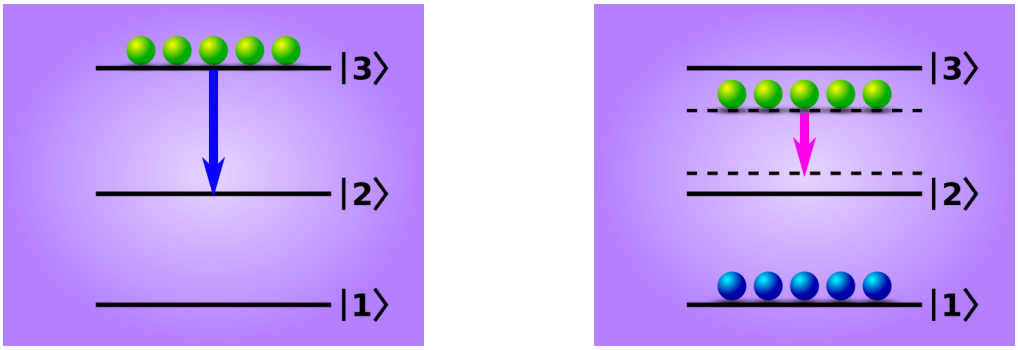

Figure 4.4 Mean-field shift measurement using RF spectroscopy. The states $|1\rangle$, $|2\rangle$ and $|3\rangle$ are the three lowest hyperfine states of ^{6}Li. RF transfer from the state $|3\rangle$ to the state $|2\rangle$ (a) without atoms present in state $|1\rangle$ and (b) with atoms present in state $|1\rangle$. The atoms in state $|1\rangle$ creates a mean-field interaction induced energy shift (dotted levels) of states $|2\rangle$ and $|3\rangle$ due to the $|1\rangle-|2\rangle$ narrow Feshbach resonance near 543.2 G and $|1\rangle-|3\rangle$ broad Feshbach resonance near 690 G, respectively.

shows the hyperfine levels with atoms in state $|3\rangle$. The atoms in state $|3\rangle$ are transferred to state $|2\rangle$ by applying a resonant RF π pulse. The required frequency of the RF pulse is dependent on the hyperfine splitting of the states $|2\rangle$ and $|3\rangle$ at the applied magnetic field [Zha13].

When atoms are prepared in the states $|1\rangle$ and $|3\rangle$ (Fig. 4.4b), they interact with each due to the $|1\rangle$ - $|3\rangle$ Feshbach resonance at 690 G with a width of 120 G [Bar05]. The interaction between states $|1\rangle$ and $|3\rangle$ causes a mean-field shift of their hyperfine energy levels, which is proportional to the scattering length and the density of atoms in state $|1\rangle$. The $|1\rangle-|3\rangle$ two-body scattering length near 543 G due to the Feshbach resonance at 690 G is $a_{13}\approx -267\,a_0$ [Haz12]. Since their interaction is very weak and attractive near 543 G, the state $|3\rangle$ is shifted downward in proportional to $n_1 a_{13}$, where n_1 is the averaged density of atoms in state $|1\rangle$.

Similarly near the narrow Feshbach resonance at 543 G, states $|1\rangle$ and $|2\rangle$ interact with each other causing a shift in their hyperfine levels. The background scattering length for the states $|1\rangle$ and $|2\rangle$ is $a_{bg} = 62\,a_0$. Hence the state $|2\rangle$ is shifted upwards away from the resonance. When the magnetic field is tuned near narrow Feshbach resonance, the shift in state $|2\rangle$ changes as a function of its scattering length. By measuring the RF spectra and extracting its peak transition frequency, the shift in state $|2\rangle$ is measured. The two-body scattering length for the $|1\rangle-|2\rangle$ mixture is then determined from the measured shift in state $|2\rangle$.

4.3 Calculation of Line Shape for Mean-field Shifted RF Spectra

In the previous section, I described briefly the mean-field shift measurement using RF spectroscopy. Prior to showing the experimental results, I would like to discuss the theoretical calculation for the line shape of mean-field shifted RF spectra. In all the experiments, the ν_1 optical beam has a $1/e$ intensity radius $w_1 = 530\,\mu$m, much larger than the $1/e$ cloud radii of the atomic cloud, $\sigma_z = 135\,\mu$m (axial) and $\sigma_r = 7\,\mu$m (radial). The 1/e intensity radius of the ν_2 beam is $w_2 = 175\,\mu$m, comparable to axial size of the atomic cloud. This results in a spatially dependent mean-field shift, which should be taken into account in calculating the line shapes for the mean-field shifted RF spectra.

I begin with the case of atoms in pure state $|3\rangle$, ie., without the presence of atoms in state $|1\rangle$ and state $|2\rangle$. The transition probability [Sho90] for an RF transfer of atoms from pure state $|3\rangle$ to $|2\rangle$ is given by

$$P(\nu_{RF}) = \frac{\Omega_{RF}^2 \sin^2\left[\pi\tau\sqrt{\Omega_{RF}^2 + \nu_{RF}^2}\right]}{\Omega_{RF}^2 + \nu_{RF}^2}, \tag{4.4}$$

where Ω_{RF} is the Rabi frequency of the transition in Hz and ν_{RF} is the frequency of the transition and τ is the duration of the radio frequency pulse. As mentioned in the previous section, the presence of atoms in state $|1\rangle$ cause a mean-field shift in the hyperfine energy levels of state $|2\rangle$ and $|3\rangle$. Hence the transition probability from state $|3\rangle$ to $|2\rangle$ in the presence of atoms in $|1\rangle$ should include a shift $\Delta\nu$ in frequency and can be expressed as

$$P(\nu_{RF}) = \frac{\Omega_{RF}^2 \sin^2\left[\pi\tau\sqrt{\Omega_{RF}^2 + [\nu_{RF} - \Delta\nu]^2}\right]}{\Omega_{RF}^2 + [\nu_{RF} - \Delta\nu]^2}. \tag{4.5}$$

The shift $\Delta\nu$ is given by

$$\Delta\nu = \frac{2\hbar}{m}\,\bar{n}_{3D}(\mathbf{r})[a_{13} - \langle a_{12}\rangle_{p_{rel}}], \tag{4.6}$$

where a_{13} is the two-body scattering length for the $|1\rangle - |3\rangle$ mixture, and $\langle a_{12}\rangle_{p_{rel}}$ is the two-body momentum averaged scattering length for the $|1\rangle - |2\rangle$ mixture and $\bar{n}_{3D}(\mathbf{r})$ is the average 3D density of atoms in $|1\rangle$.

In Section 2.3.6, I have discussed in detail the calculation of momentum averaged scattering length $\langle a_{12}\rangle_{p_{rel}}$. I will summarize the results below. By assuming a classical Boltz-

mann distribution for the relative momentum $\mathbf{p}$ between atoms in states $|1\rangle$ and $|2\rangle$, the momentum averaged scattering length can be expressed as,

$$\langle a_{12}\rangle_{p_{rel}} = \int_0^\infty d\mathbf{p}\, \frac{4\pi\mathbf{p}^2}{\pi^{3/2}p_0^3}\, e^{-\mathbf{p}^2/p_0^2}\, \mathrm{Re}[f(\mathbf{p})] \tag{4.7}$$

where $f(\mathbf{p})$ is the $|1\rangle - |2\rangle$ forward scattering amplitude derived in Eq. 2.70, $p_0 = \sqrt{2mk_BT}$, T is the temperature of the gas, and m is the mass of ^{6}Li atoms. In the presence of the optical beams, the $|1\rangle - |2\rangle$ forward scattering amplitude is also dependent on axial position z and can be expressed as $f(z,\mathbf{p})$.

Previous methods [Haz12] of determining the mean-field shifted RF line shape involved using Eq. 4.7 and Eq. 4.6 in Eq. 4.5, where the scattering length is already momentum averaged. However, for the experiments reported in this thesis, the RF line shape determined from Eq. 4.5 using the momentum averaged scattering length $\langle a_{12}\rangle_{p_{rel}}$ in Eq. 4.7 disagreed with the experimental results. Therefore, a new approach to determine the RF line shape was required.

In the new model, the atoms in state $|2\rangle$ is considered to be immersed in a bath of perturbing atoms in state $|1\rangle$ with 3D density $n_{3D}(\mathbf{r})$ and normalized momentum distribution $W(\mathbf{p}_p)$. For the non-degenerate regime, the momentum distribution of perturbers $W(\mathbf{p}_p)$ in state $|1\rangle$ and the momentum distribution of atoms $W(\mathbf{p}_a)$ in state $|2\rangle$ can be expressed as,

$$W(\mathbf{p}') = \frac{1}{\pi^{3/2}p_0^3}\, e^{-\mathbf{p}'^2/p_0^2}. \tag{4.8}$$

where $\mathbf{p}' = \mathbf{p}_p$ for the perturbers and $\mathbf{p}' = \mathbf{p}_a$ for the active atoms.

Instead of calculating the transition probability of atoms using the relative momentum-averaged scattering length, a two-step approach is used to calculate the final transition probability.

(i) The transition probability of atoms with momentum $\mathbf{p}_a$ in a bath of perturbers with momentum distribution $W(\mathbf{p}_p)$ is initially calculated by using the perturber-momentum averaged scattering length.

(ii) The transition probability obtained in step (i) is then integrated over the atom's momentum distribution $W(\mathbf{p}_a)$ to evaluate the final transition probability.

In order to evaluate the transition probability of atoms with momentum $\mathbf{p}_a$ (step (i) - listed above), the $\mathbf{p}_a$ dependent scattering length of the atoms $a_{12}(p_a)$ in a bath of perturbers

should be first evaluated. Therefore, the $|1\rangle - |2\rangle$ forward scattering amplitude $f(\mathbf{p})$ is first averaged over the momentum distribution of perturbers $W(\mathbf{p}_p)$. Furthermore, in the optical control experiments reported here, the size of the ν_2 beam is comparable to the axial size (z-direction) of the atomic cloud (see Section 4.5), which creates spatially varying interactions. Therefore, in the presence of optical beams, the $|1\rangle - |2\rangle$ forward scattering amplitude $f(\mathbf{p})$ is dependent on the position z due to the spatially varying Rabi frequency $\Omega_2(z)$, and hence denoted as $f(z,\mathbf{p})$.

The optically controlled perturber averaged two-body scattering length $a_{12}^{opt}(p_a,z)$ for the $|1\rangle - |2\rangle$ mixture is given by

$$a_{12}^{opt}(p_a,z) = \int d^3\mathbf{p}_p \, W(\mathbf{p}_p) \mathrm{Re}[f(z,\mathbf{p})]. \tag{4.9}$$

Here, the relative momentum $\mathbf{p} = (\mathbf{p}_a - \mathbf{p}_p)/2$. Note that $a_{12}^{opt}(p_a,z)$ also depends on Ω_1, Ω_2, ν_1, ν_2, and the magnetic field B. A simplified notation of the $|1\rangle - |2\rangle$ perturber averaged scattering length $a_{12}^{opt}(p_a,z)$ is used in this section to avoid confusion. In the absence of the optical fields, the $|1\rangle - |2\rangle$ scattering length a_{12} depends only on B and becomes,

$$a_{12}(p_a) = \int d^3\mathbf{p}_p \, W(\mathbf{p}_p) \, \mathrm{Re}[f(\mathbf{p})]. \tag{4.10}$$

After changing the integration variable from $\mathbf{p}_p$ to $\mathbf{p}$ using the relationship $\mathbf{p}_p = \mathbf{p}_a - 2\mathbf{p}$, Eq. 4.9 becomes

$$a_{12}^{opt}(p_a,z) = -\frac{8}{\pi^{3/2} p_0^3} \int d^3\mathbf{p} \; e^{-(\mathbf{p}_a^2 + 4\mathbf{p}^2 - 4\mathbf{p}_a\cdot\mathbf{p})/p_0^2} \, \mathrm{Re}[f(z,\mathbf{p})] \tag{4.11}$$

Using $d^3\mathbf{p} = p^2 \, dp \, d\Omega_p$ in Eq. 4.11 yields

$$a_{12}^{opt}(p_a,z) = -\frac{8}{\pi^{3/2} p_0^3} \, e^{-\mathbf{p}_a^2/p_0^2} \int_0^\infty dp \, p^2 \; e^{-4p^2/p_0^2} \, \mathrm{Re}[f(z,\mathbf{p})] \; I_\Omega \tag{4.12}$$

where I_Ω is the integration over the perturber solid angle $d\Omega_p$ and is given by

$$\begin{aligned} I_\Omega &= 2\pi \int_0^\pi d\theta \, \sin\theta \; e^{4p_a p \cos\theta / p_0^2} \\ &= \frac{\pi \, p_0^2}{p_a \, p} \, \sinh\left(\frac{4 p_a p}{p_0^2}\right) \end{aligned} \tag{4.13}$$

Substituting Eq. 4.13 in Eq. 4.12 gives

$$a_{12}^{opt}(p_a,z) = -\frac{8}{p_a\, p_0\, \sqrt{\pi}} \int_0^\infty dp\, p\, e^{\left(-\frac{4p^2+p_a^2}{p_0^2}\right)} \sinh\left(\frac{4p_a p}{p_0^2}\right) Re\{f(z,p)\}. \tag{4.14}$$

We see from the above equation that $a_{12}^{opt}(p_a,z)$ depends on $p_a = |\mathbf{p}_a|$ and z. The density dependent frequency shift in Hz for atoms with momentum $\mathbf{p_a}$ is then written as

$$\Delta\nu(p_a,\mathbf{r}) = \frac{2\hbar}{m}\, n_{3D}(\mathbf{r})[a_{13} - a_{12}^{opt}(p_a,z)], \tag{4.15}$$

where $n_{3D}(\mathbf{r})$ is the 3D density of perturbers with momentum $\mathbf{p_p}$, a_{13} is the two-body scattering length for the $|1\rangle - |3\rangle$ mixture, and m is the mass of the atom. The transition probability of atoms with momentum $\mathbf{p_a}$ from state $|3\rangle$ to $|2\rangle$ in the presence of atoms in state $|1\rangle$ is written as

$$P(p_a,\mathbf{r},\nu_{RF}) = \frac{\Omega_{RF}^2 \sin^2\left[\pi\tau\sqrt{\Omega_{RF}^2 + [\nu_{RF} - \Delta\nu(p_a,\mathbf{r})]^2}\right]}{\Omega_{RF}^2 + [\nu_{RF} - \Delta\nu(p_a,\mathbf{r})]^2}, \tag{4.16}$$

where Ω_{RF} is Rabi frequency of the transition in Hz and ν_{RF} is the frequency of the transition and τ is the duration of the radio frequency pulse. The frequency shift $\Delta\nu(p_a,\mathbf{r})$ in Hz is given in Eq. 4.15.

Eq. 4.16 gives the individual transition probability of atoms with momentum $\mathbf{p}_a$. The average transition probability of the atoms is then evaluated (step (ii) - listed above) by integrating the individual transition probability (Eq. 4.16) over the momentum distribution of atoms. The atom-momentum averaged transition probability $P(\mathbf{r},\nu_{RF})$ from state $|3\rangle$ to $|2\rangle$ in the presence of atoms in state $|1\rangle$ is written as,

$$P(\mathbf{r},\nu_{RF}) = \int d^3\mathbf{p}_a\, W(\mathbf{p}_a)\, P(p_a,\mathbf{r},\nu_{RF}). \tag{4.17}$$

The one-dimensional z-dependent density of atoms transferred from state $|3\rangle$ to state $|2\rangle$ is then determined from the $\mathbf{p}_a$-dependent transition probability, by integrating over the radial spatial profile of the active atoms, which are initially in state $|3\rangle$,

$$n_2(z,\nu_{RF}) = \int_0^\infty 2\pi\rho\, d\rho\, n_{3D}(\rho,z)\, P(\mathbf{r},\nu_{RF}) \tag{4.18}$$

Eq. 4.18 determines the spatial profile of the transferred atoms and is one of the most

important results of the theoretical model. Particularly, for experiments demonstrating designer spatial control of interactions (Section 4.6), the axial profile of the transferred cloud from state $|3\rangle$ to state $|2\rangle$ is critical in understanding the experimental results. Eq. 4.18 provides a simple model for predicting the axial profiles of the transferred cloud and is compared to the measurements in Fig. 4.12.

The radio-frequency spectrum is determined by the total number of atoms transferred to state $|2\rangle$ by integrating the 1D density in Eq. 4.18,

$$N_2(\nu_{RF}) = \int_{-\infty}^{\infty} dz\, n_2(z, \nu_{RF}). \tag{4.19}$$

The normalized fraction of the atoms remaining in state $|3\rangle$ is given by,

$$N_3(\nu_{RF})/N_0 = 1 - N_2(\nu_{RF})/N_0, \tag{4.20}$$

where N_0 is the initial number of atoms in state $|3\rangle$. Eq. 4.20 is another important result of our model, which is used to compare the measured RF line shapes in both optical (Section 4.5) and magnetic control (Section 4.4) experiments.

I will conclude this section by calculating relative momentum averaged scattering length $\bar{a}_{12}$ (Eq. 4.7) with the new model. Here, the momentum averaged scattering length $a_{12}^{opt}(z)$ is calculated by initially evaluating the perturber momentum averaged scattering length in Eq. 4.9 and then integrating Eq. 4.9 over the momentum distribution of the active atoms, $W(\mathbf{p}_a)$,

$$a_{12}^{opt}(z) = \int d^3\mathbf{p}_a\, W(\mathbf{p}_a)\, a_{12}^{opt}(p_a, z). \tag{4.21}$$

where $W(\mathbf{p}_a)$ and $a_{12}^{opt}(p_a, z)$ is given in Eq. 4.8 and Eq. 4.9, respectively. Similarly, in the absence of optical beams, the momentum averaged scattering length $\bar{a}_{12}$ is given by

$$\bar{a}_{12} = \int d^3\mathbf{p}_a\, W(\mathbf{p}_a)\, a_{12}(p_a) \tag{4.22}$$

where $a_{12}(p_a)$ is given in Eq. 4.10. I would like to particularly emphasize that the scattering length determined using the *atom-perturber* momentum average (Eq. 4.21 and Eq. 4.22) produces the same result as the scattering length determined by relative momentum average, Eq. 4.7. However, the RF line shape evaluated using the *atom-perturber* momentum averaged scattering length produces a markedly different and correct result than the RF

line shape evaluated using the relative momentum averaged scattering length.

4.4 Magnetically Tuning the Interactions near the Narrow Feshbach Resonance

In this section, I present first the experimental results demonstrating magnetic tuning (no optical fields) of the scattering length near the narrow Feshbach resonance. I will also discuss the experimental procedure for the measurement of mean-field frequency shifts in the RF spectra and the determination of scattering length from the measured mean-field frequency shifts.

A 50-50 mixture of ^{6}Li atoms are prepared in the two lowest hyperfine states $|1\rangle$ and $|2\rangle$. After evaporatively cooling the atoms at 300 G in a CO_2 laser optical trap, the trap is re-raised to 2% of the maximum trap depth. The magnetic field is then ramped to 528 G, where the $|1\rangle - |2\rangle$ mixture is non-interacting. An RF sweep then transfers atoms from state $|2\rangle$ to state $|3\rangle$, resulting in a $|1\rangle - |3\rangle$ mixture. The trap depth is then raised to 5% of the total trap depth and the magnetic field is ramped to the field of interest, near the narrow Feshbach resonance ($B_{res} = 543.27$ G) in ^{6}Li. The magnetic field typically stabilizes after a wait time of 3 seconds due to the inductance of the high-field coils. After achieving a stable magnetic field, an RF pulse is applied for 1.2 ms to transfer the atoms from state $|3\rangle$ and state $|2\rangle$. The remaining atoms in state $|3\rangle$ are imaged as a function of frequency, after a time of flight of 200 μs. This yields the mean-field shifted RF spectra in Fig. 4.5 (orange).

To measure the unshifted RF spectra Fig. 4.5 (green), the above procedure is repeated without atoms in state $|1\rangle$. Here, a resonant optical pulse is applied to kill atoms in state $|1\rangle$ and the residual atoms in state $|2\rangle$. The RF spectrum is then measured for the pure state transition from $|3\rangle$ to $|2\rangle$, without atoms in state $|1\rangle$. The unshifted RF spectra is also used to calibrate the magnetic field. In order to avoid measurement artifacts due to systematic drifts in the magnetic fields, the RF spectra is measured by interweaving the experiment in the presence (shifted RF spectra) and absence (unshifted RF spectra) of atoms in state $|1\rangle$.

Fig. 4.5 shows the measured RF spectra for different magnetic fields near the narrow Feshbach resonance. The RF spectra with and without the atoms in state $|1\rangle$ are shown as orange dots and green dots, respectively. The RF spectra without atoms in state $|1\rangle$ are fitted with the Eq. 4.4 (green curves). Solid orange lines are the fit of shifted RF spectra with Eq. 4.20, where $a_{12}(p_a)$ in Eq. 4.10 depends only on the magnetic field B. The unshifted RF

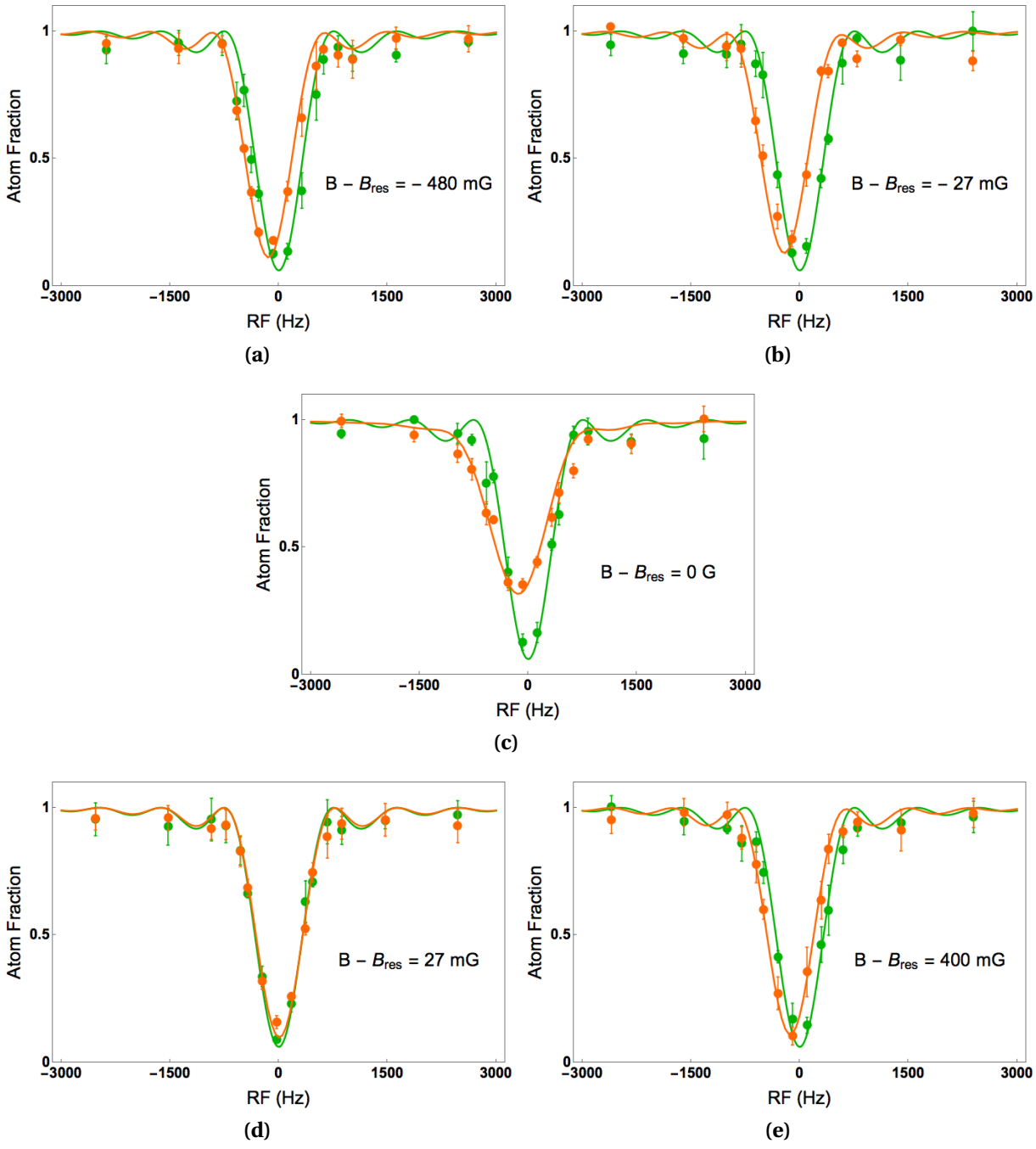

Figure 4.5 Mean-field shift measurement for different magnetic fields near the magnetic Feshbach resonance. The RF spectra with and without the atoms in state $|1\rangle$ are shown in orange dots and green dots, respectively. Solid green lines are the fit of the unshifted RF spectra with Eq. 4.4. Solid orange lines are the fit of the shifted RF spectra with Eq. 4.20, where $a_{12}(p_a)$ in Eq. 4.10 depends on the magnetic field B. The experimental parameters used to generate the solid orange lines are compiled in the Table 4.1.

spectra is used to calibrate the magnetic field.

Fig. 4.5a and Fig. 4.5e represents the mean-field shift spectra where the $|1\rangle - |2\rangle$ scattering length is minimum, almost equivalent to the background scattering length. For an atomic density $\bar{n} \approx 10^{12}$ atoms/cm^3, the shift is -120 Hz at the background. This mean-field induced frequency shift is due to the interaction between the states $|1\rangle - |3\rangle$ and the states $|1\rangle - |2\rangle$ away from the resonance. The $|1\rangle$ - $|3\rangle$ Feshbach resonance is at 690 G and its scattering length near 543 G is -267 a_0. The background scattering length of the states $|1\rangle$ - $|2\rangle$ near 543 G is 62 a_0. Hence the $|1\rangle$ - $|3\rangle$ scattering length dominates and the shift is negative (background shift) for magnetic fields $|B - B_{res}| >> \Delta B$ (Fig. 4.5a and Fig. 4.5e).

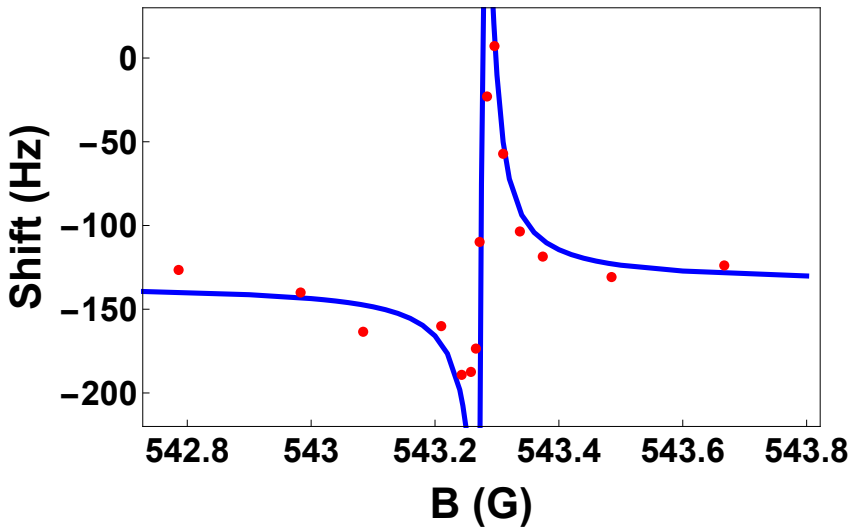

Figure 4.6 Measured mean-field shifts (red dots) as a function of magnetic field. Solid blue curve is calculated from the shifted RF spectra predicted using Eq. 4.20.

The maximum negative shift of -189 Hz is observed at $B - B_{res} = -27$ mG and shown in Fig. 4.5b. The scattering length a_{12} is also maximum and positive at this magnetic field. When the magnetic field is tuned to the resonance $B - B_{res} = 0$ mG, the shift in the RF spectra is -109 Hz. From Fig. 4.5c, we can also see that at $B - B_{res} = 0$ mG, the amplitude of the shifted RF spectra is suppressed and the line shape is broadened. This is due to the large resonant interaction between the states $|1\rangle - |2\rangle$.

As the magnetic field is tuned above resonance, the RF spectra shift further to the right, corresponding to positive frequency shifts. Fig. 4.5d shows a shift of +7 Hz at $B - B_{res} = 27$

mG. The scattering length a_{12} is maximum and negative at this magnetic field. When the magnetic field is increased further, the RF spectra shifts back to the left (decreasing positive values of frequency shifts) and reaches the background shift of -120 Hz as shown in Fig. 4.5e.

From Fig. 4.5, the mean-field induced shifts in the RF spectra for different magnetic fields are extracted and plotted in Fig. 4.6 (red dots). The solid blue curve in Fig. 4.6 is calculated from the shifted RF spectra predicted using Eq. 4.20. The predicted mean-field shifts (solid blue curve in Fig. 4.6), is in good agreement with the measured mean-field shifts (red dots).

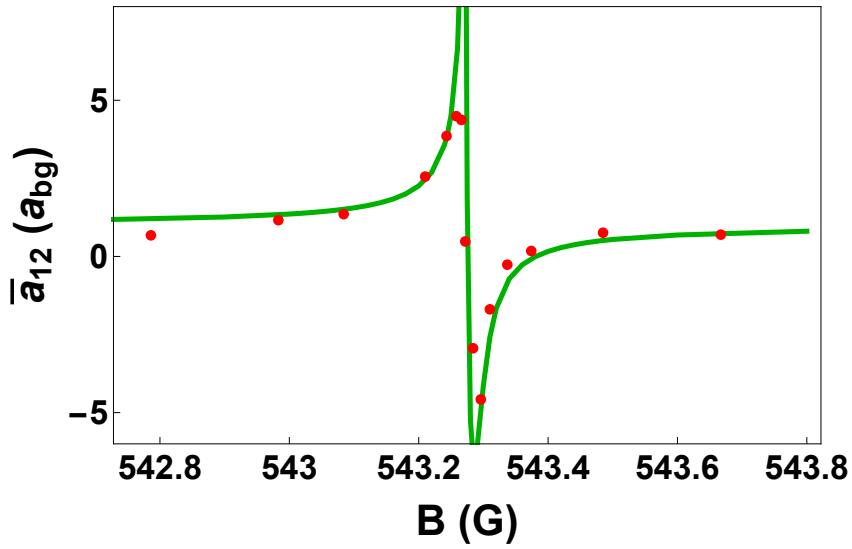

Figure 4.7 Momentum averaged scattering length $\bar{a}_{12}$ as a function of magnetic field. The red dots is determined by using $\bar{n}_1 = 3.6 \times 10^{11}$ cm^{-3} and the measured mean-field shifts (Fig. 4.6) in Eq. 4.23. Solid green curve is the prediction of the continuum-dressed state model (Eq. 4.22).

From the measured frequency shifts, an average two-body scattering length $\bar{a}_{12}$ for the narrow Feshbach resonance can be determined. The average mean-field frequency shift is defined by

$$\Delta \nu_{meas} = \frac{2\hbar}{m} \bar{n}_1 (a_{13} - \bar{a}_{12}), \tag{4.23}$$

where $\bar{n}_1$ is the average three-dimensional density of atoms in state $|1\rangle$. For the data shown

in Fig. 4.6, the *background* two-body scattering length far from the resonance is

$$a_{13} \approx -267\,a_0 \tag{4.24}$$

$$a_{12} = a_{bg} = 62\,a_0 \tag{4.25}$$

and the *background* mean-field frequency shift is,

$$\Delta\nu_{meas} = -120 \text{ Hz} \tag{4.26}$$

Using Eq. 4.26 - Eq. 4.25 in Eq. 4.23, yields $\bar{n}_1 = 3.6 \times 10^{11}$ cm^{-3}. Applying $\bar{n}_1$ as the fixed fit parameter in Eq. 4.23 for all the mean-field shifts in Fig. 4.6, the momentum averaged two-body scattering length $\bar{a}_{12}$ (red dots) is determined and shown in Fig. 4.7. The solid green curve in Fig. 4.7 is the momentum averaged scattering length calculated from Eq. 4.22. The predicted mean-field shifts shown in Fig. 4.6 (solid blue curve) and the momentum averaged scattering length shown in Fig. 4.7 (solid green curve) are generated using same parameters given in Table 4.1.

Fig. 4.7 shows that the tuning range of the two-body scattering length is between $+5\,a_{bg}$ (BEC side of resonance) and $-5\,a_{bg}$ (BCS side). The tunability is primarily limited by the energy-dependence of the scattering length near the narrow Feshbach resonance, i.e., the large effective range. The scattering length plot shown in Fig. 4.7 is comparable to the results reported previously [Haz12]. Hence extracting scattering lengths from the mean-field shifted RF spectra provides a reliable technique to measure two-body scattering lengths near a narrow Feshbach resonance in ultra-cold Fermi gases.

4.5 EIT Optical Control of Interactions near the Narrow Feshbach Resonance

In the previous section, I discussed the use of RF spectroscopy to measure mean-field shifts and to determine the scattering length from the measured mean-field shifts near the narrow Feshbach resonance. Now that we have a reliable method to determine the scattering length, optical control of scattering interactions can be demonstrated in an ultra-cold Fermi gas by exploiting this method. In this section, the experimental results demonstrating optical control of scattering interactions by measuring mean-field induced

frequency shifts in RF spectra will be presented.

A 50-50 mixture of atoms in the states $|1\rangle$ and $|2\rangle$ are evaporatively cooled in a CO_2 laser trap at 300 G. The magnetic field is then ramped to 528 G, where the $|1\rangle - |2\rangle$ mixture is non-interacting. At 2% of the maximum trap depth, an RF sweep transfers atoms from state $|2\rangle$ to state $|3\rangle$, resulting in a $|1\rangle - |3\rangle$ mixture. The trap depth is raised to 5% of the maximum and the magnetic field is ramped to the field of interest.

To measure frequency shifts in the RF spectra arising from mean-field interactions, a ν_2 beam with Rabi frequency $\Omega_2 = 2.1\,\gamma_e$ is applied initially. The ν_2 beam creates a non-negligible confinement in the axial z direction of the cloud. The atoms reach equilibrium in the combined potential created by the ν_2 beam and the CO_2 laser trap in 50 ms. The ν_1 beam with Rabi frequency $\Omega_1 = 0.5\,\gamma_e$ and detuning $\Delta_1 = \nu_1 - \nu_{eg_1} = 19$ MHz (Refer Fig. 4.2) is then applied. Concurrently, an RF π pulse is applied for 1.2 ms, which transfers the atoms from state $|3\rangle$ to state $|2\rangle$. The atoms in state $|3\rangle$ are then imaged after a time of flight of 200 μs, yielding the frequency shifted RF spectra. The unshifted RF spectra is obtained by removing the atoms in state $|1\rangle$ by a resonant imaging pulse and then performing the RF spectroscopy for the bare $|3\rangle$ - $|2\rangle$ transition in the presence of optical beams ν_1 and ν_2.

Fig. 4.8 shows the measured RF spectra for different two-photon detuning δ (by varying ν_2 and holding ν_1 constant), at $B = B_{res} + 0.010$ G. The RF spectra with and without atoms in state $|1\rangle$ are shown as magenta dots and purple dots, respectively. The unshifted RF spectra without the atoms in state $|1\rangle$ are fitted with Eq. 4.4 (purple curve). Solid magenta lines are the fit of shifted RF spectra with Eq. 4.20 using measured parameters.

The experimental parameters used to calculate the RF spectra in Fig. 4.8 are summarized in the Table 4.1. The temperature $T \approx 1\,\mu$K is used to fit all shifted RF spectra in Fig. 4.8 with Eq. 4.20. But the measured temperature from the cloud size and trap parameters is $T \approx 1.4\,\mu$K. This discrepancy might be due to the additional potential created by the ν_2 beam thereby making the measurement of the combined CO_2- ν_2 optical trap parameters particularly challenging.

Fig. 4.8a and Fig. 4.8e represent the mean-field interaction induced frequency shifts in the RF spectra, where the $|1\rangle - |2\rangle$ scattering length a_{12} is minimum and is approximately equivalent to the background scattering length a_{bg}, i.e. $a_{12} \approx a_{bg} = 62\,a_0$. For the experimental conditions, the shift is -95 Hz at the background.

The maximum negative shift of -199 Hz, is observed at δ = - 0.525 MHz and is shown in Fig. 4.8b. The scattering length a_{12} is maximum and positive at this frequency. Here, the

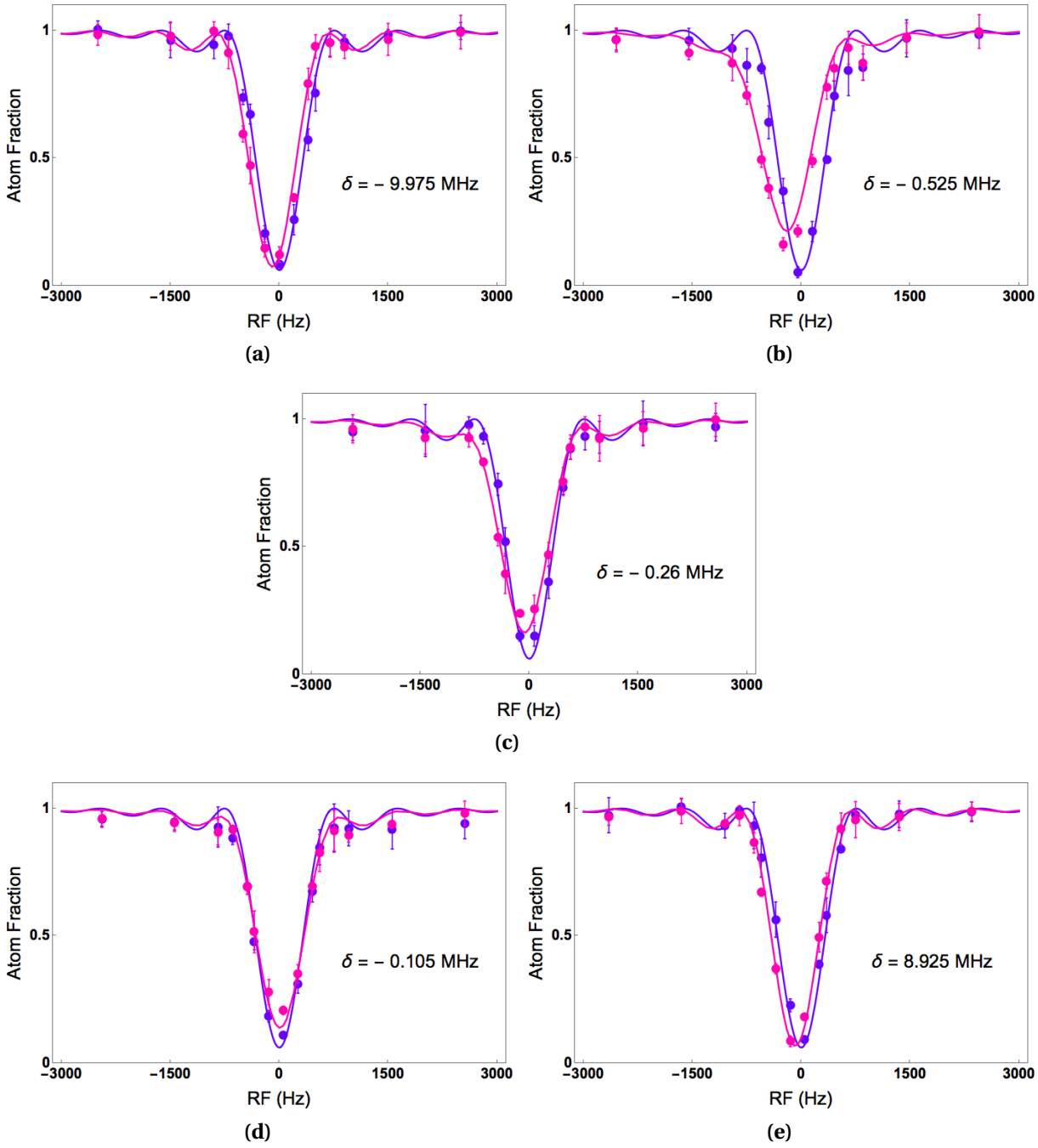

Figure 4.8 Mean-field shift measurement for different two-photon detuning, δ, near a magnetic Feshbach resonance. The RF spectra with and without the atoms in state $|1\rangle$ are shown in magenta dots and purple dots respectively. Solid purple lines are the fit of unshifted RF spectra with Eq. 4.4. Solid magenta lines are the fit of the shifted RF spectra with Eq. 4.20 using the experimental parameters listed in the Table 4.1.

Table 4.1 Experimental parameters used to calculate mean-field shifted RF spectra in Fig. 4.8

Experimental Parameter	Symbol	Value
Rabi frequency of ν_1 beam	Ω_1	$0.5 \pm 0.01\ \gamma_e$
Rabi frequency of ν_2 beam	Ω_2	$2.1 \pm 0.1\ \gamma_e$
Detuning of ν_1 beam	Δ_1	19 MHz
Temperature of the atomic cloud	T	$\approx 1\ \mu k$
Axial frequency of the total (CO_2 + ν_2 beam) trap	ω_z	$2\pi \times (56 \pm 0.5)$ Hz
Radial frequency of the CO_2 trap	ω_x	$2\pi \times (777 \pm 9.5)$ Hz
Radial frequency of the CO_2 trap	ω_y	$2\pi \times (960 \pm 4.32)$ Hz
Rabi frequency of RF pulse	Ω_{RF}	350 ± 2 Hz
$\|1\rangle$-$\|3\rangle$ scattering length near 543 G	a_{13}	- 267 a_0

singlet ground state $|g_1\rangle$ is below the triplet continuum $|T,k\rangle$, BEC side (See Chapter 2 for an explanation of the BEC-BCS crossover) and the interactions are repulsive. When δ is increased further, the mean-field shift decreases. At δ = - 0.26 MHz, the singlet state $|g_1\rangle$ is almost tuned to be degenerate with the triplet state $|T,k\rangle$ leading to resonant interactions and the measured shift in the RF spectra is - 66 Hz, Fig. 4.8c.

As δ is increased further, the RF spectra shifts to the right. At δ = -0.105 MHz, Fig. 4.8d, the observed mean-field shift is +7 Hz, where the scattering length is maximum and negative. Here, the singlet ground state $|g_1\rangle$ is optically tuned to lie above the triplet continuum $|T,k\rangle$, BCS side and the interactions are attractive. When δ is increased further, the shifted RF spectra moves back to the left and reaches the background shift of -95 Hz as shown in Fig. 4.8e.

Fig. 4.9 (red dots) shows the measured frequency shifts of the RF spectra, as a function of two-photon detuning δ, by varying frequency ν_2 and holding the frequency ν_1 constant. The solid blue line is the predicted mean-field shift, which is obtained from Eq. 4.20 by extracting the ν_{RF} corresponding to the maximum atom transfer from state $|3\rangle$ to $|2\rangle$. The measured and the calculated mean-field shift are in excellent agreement.

The next step is to estimate the optically controlled momentum averaged scattering length $\bar{a}_{12}^{opt}$ from the measured mean-field shift in Fig. 4.9. As in Eq. 4.23 the measured frequency shifts $\Delta\nu_{meas}$ can be expressed as

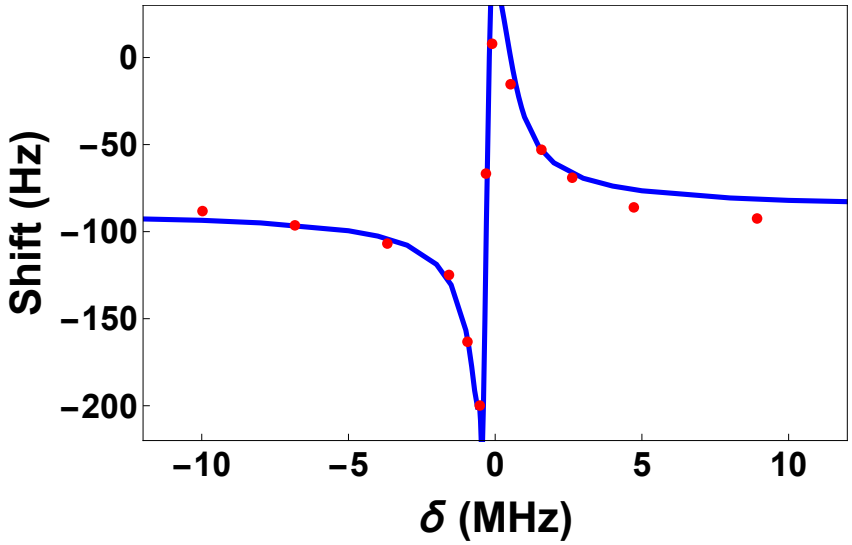

Figure 4.9 Measured mean-field shifts (red dots) as a function of two-photon detuning δ, by varying ν_2 and holding ν_1 constant. Blue curve: Predicted mean-field shift from Eq. 4.20.

$$\Delta\nu_{meas} = \frac{2\hbar}{m}\bar{n}_1(a_{13} - \bar{a}_{12}^{opt}), \tag{4.27}$$

where $\bar{n}_1$ is the average three dimensional density and is used as a fixed fit parameter for all of the data. Substituting the *background* two-body scattering length (62 a_0) and the corresponding mean-field shift (- 95 MHz from Fig. 4.9) in Eq. 4.27, yields $\bar{n}_1 = 1.5\times10^{11}$ cm^{-3}. The momentum averaged scattering length $\bar{a}_{12}^{opt}$ (red dots) in Fig. 4.10 are then determined from the measured mean-field shifts in Fig. 4.9 (red dots) by using $\bar{n}_1 = 1.5\times10^{11}$ cm^{-3} in Eq. 4.27 for all data points.

To generate the green curve in Fig. 4.10, the optically controlled spatially dependent two-body scattering length $a_{12}^{opt}(z)$ is first calculated as a function of axial position z from Eq. 4.21. Note that a_{12}^{opt} generally depends on Ω_1, Ω_2, ν_1, ν_2, and the magnetic field B. The size of the ν_2 beam is comparable to the axial size of the atom cloud (z - axis) and hence the Rabi frequency $\Omega_2(z)$ is z-dependent. This makes the scattering length a_{12}^{opt} spatially dependent. The optically controlled scattering length at the center of the cloud $a_{12}^{opt}(0)$ (Eq. 4.21) is evaluated at $z = 0$ and is shown in Fig. 4.10 (green curve). The calculated optically controlled two-body scattering length $a_{12}^{opt}(0)$ (green curve) is in excellent agreement with the momentum averaged scattering length $\bar{a}_{12}^{opt}$ (red dots) determined from the measured mean-field induced frequency shifts in RF spectra. The green curve in Fig. 4.10 and the

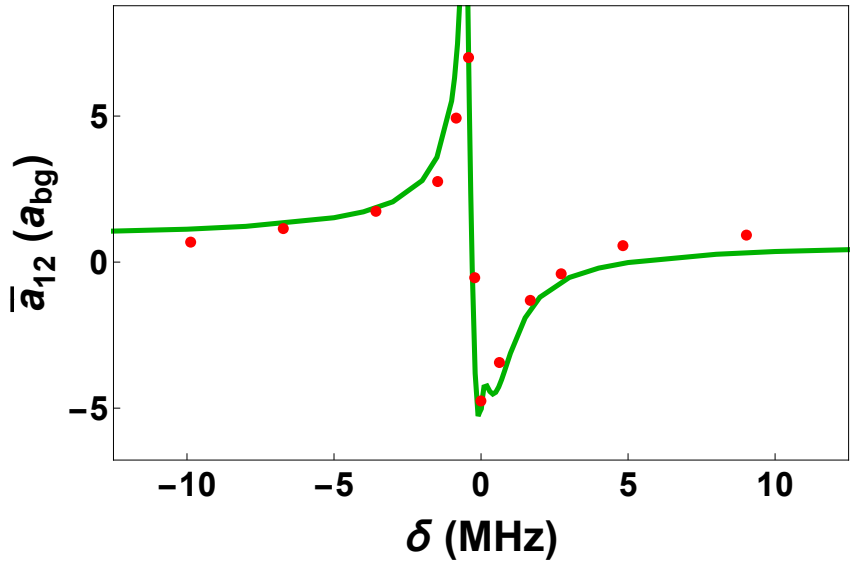

Figure 4.10 Momentum averaged scattering length $\bar{a}_{12}^{opt}$ as a function of two-photon detuning δ, by varying ν_2 and holding ν_1 constant. The momentum averaged scattering length $\bar{a}_{12}^{opt}$ (red dots) are determined by using $\bar{n}_1 = 1.5 \times 10^{11}$ cm^{-3} in Eq. 4.27 for the measured mean-field shifts from Fig. 4.9. Solid green curve is optically controlled scattering length at the center of the cloud $a_{12}^{opt}(0)$ (Eq. 4.21) predicted from the theoretical model.

predicted mean-field shift (blue curve) in Fig. 4.9 are evaluated using the same set of parameters summarized in Table 4.1.

Fig. 4.10 illustrates that the EIT method of controlling interactions tunes the two-body scattering length between $+7\,a_{bg}$ (BEC side of resonance) and $-5\,a_{bg}$ (BCS side) by changing the two-photon detuning δ by just a few MHz, the same range as obtained by magnetic tuning, Fig. 4.7. In both cases, the tunability is primarily limited by the energy-dependence of the scattering length near the narrow Feshbach resonance, i.e., the large effective range. For the time scale (1.2 ms) used in the optical control experiments, the atom loss due to spontaneous scattering is negligible.

4.6 Spatial Control of Interactions

In the last section, I will discuss experiments demonstrating spatial control of the interactions using the ν_1 and ν_2 optical fields. As discussed previously in this chapter, optical fields ν_1 and ν_2 achieved the same range of tunability in scattering length as magnetic field

tuning. This unprecedented level of optical tunability enables experiments that demonstrate designer spatial control of interactions, where different interaction spatial profiles can be imprinted on the atomic cloud by changing the frequency of the optical fields by just a few MHz. Using this method, an interaction “sandwich" is created where the central region of the atomic cloud is resonantly interacting and the wings of the cloud are weakly interacting, Fig. 4.11.

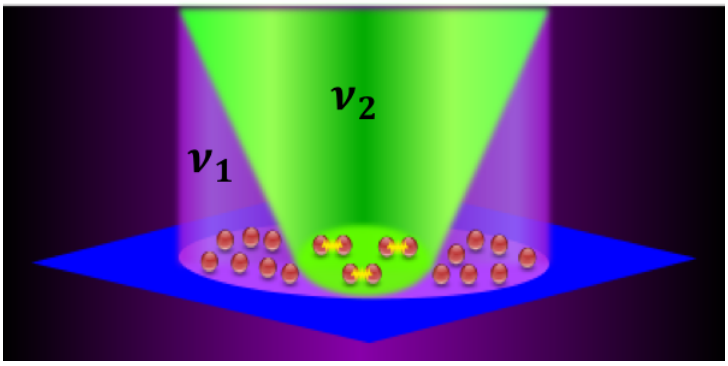

Figure 4.11 The optical field arrangement for creating an interaction “sandwich." Both ν_1 and ν_2 beams illuminate the central region of the atomic cloud. The ν_1 and ν_2 beams make the central region of the atomic cloud resonantly interacting with suppressed spontaneous scattering. The outer regions of the atomic cloud illuminated *only* by the ν_1 beam are weakly interacting.

Fig. 4.11 illustrates the optical field configuration for the spatial control of interaction in an atomic cloud. The 1/e cloud radii are $\sigma_z = 135\,\mu$m (axial) and $\sigma_r = 7\,\mu$m (radial). The 1/e intensity radius of the ν_1 beam is $w_1 = 530\,\mu$m. Hence the intensity of ν_1 beam is nearly uniform across the cloud. The 1/e intensity radius of the ν_2 beam is $w_2 = 175\,\mu$m. Although the size of the ν_2 beam is comparable to the axial size σ_z of the atom cloud, due to the Gaussian shape of the optical beam, the Rabi frequency $\Omega_2(z)$ is z-dependent. Hence the spatial dependence of $\Omega_2(z)$ enables spatial control of the two body scattering length $a_{12}^{opt}(z)$ and creates a sandwich of resonantly and weakly interacting regions.

As before the $|1\rangle - |2\rangle$ mixture is evaporatively cooled at 300 G and the CO_2 laser trap is re raised to 2% of total trap depth. The magnetic field is adiabatically changed to 528 G, where $|1\rangle - |2\rangle$ mixture is non-interacting. At 528 G, atoms in state $|2\rangle$ is transferred to state $|3\rangle$ by applying an RF sweep for 20 ms. The trap depth is raised to 5% of the maximum and the magnetic field is ramped to the field of interest, $B = B_{res} + 0.010$ G. With the $|1\rangle - |3\rangle$

mixture, the magnetic field is allowed to stabilize for 3 seconds. After the magnetic field is stabilized, the ν_2 beam with Rabi frequency $\Omega_2 = 2.1\,\gamma_e$ is applied. The ν_2 beam creates a confinement in the axial z direction of the cloud. The atoms reach equilibrium in the combined potential created by the ν_2 beam and the CO_2 laser trap for 50 ms. The ν_1 beam with Rabi frequency $\Omega_1 = 0.5\,\gamma_e$ and detuning $\Delta_1 = 19$ MHz (Refer Fig. 4.2) is then applied.

After illuminating the atoms with the ν_1 and ν_2 beams, an RF π pulse (1.2 ms) that transfers atoms from state $|3\rangle$ to $|2\rangle$ in the presence of atoms in state $|1\rangle$ is applied. The atoms arriving in state $|2\rangle$ are imaged as a function of δ, by varying ν_2 and holding ν_1 constant. In this experiment, ν_{RF} is also held constant and chosen to be resonant when the scattering length is small. From Fig. 4.9 and Fig. 4.10, we can see that the mean-field shift is - 95 MHz at the background scattering length. Hence ν_{RF} is chosen to be - 95 MHz.

Fig. 4.12 illustrates spatial control of interactions, using the two-photon detuning δ as a control parameter. The measured 2D absorption images are shown in Fig. 4.12a. The corresponding 1D axial profiles are shown in Fig. 4.12c (blue). The transferred fraction of atoms in state $|2\rangle$ depends on the spatially varying, optically controlled $|1\rangle - |2\rangle$ scattering amplitude. Fig. 4.12d shows the two-body scattering length $a_{12}^{opt}(z)$ used to generate the predicted 1D spatial profiles (red curves in Fig. 4.12c) and the predicted 2D absorption images in Fig. 4.12b.

Excellent quantitative agreement is obtained between the measured (blue) and the calculated (red) 1D axial profiles, Fig. 4.12c. The asymmetry in the 1D profiles for $\delta = -0.64$ MHz and $\delta = -0.54$ MHz is due to the off-center position of the ν_2 beam, which is taken into account in generating the calculated 1D profiles.

A two-photon detuning $\delta = -0.64$ MHz, creates an interaction “sandwich," where the central region of the atomic cloud is resonantly interacting with $a_{12} \approx 12\,a_{bg}$ and is enclosed by two weakly interacting regions with $a_{12} \approx 1\,a_{bg}$ (Fig. 4.12d). This is evident from the measured 2D profile in (Fig. 4.12a), where the transferred fraction of atoms in the central region of the cloud is heavily suppressed due to the large frequency shift arising from resonant interactions.

A small frequency change from $\delta = -0.64$ MHz to $\delta = -0.43$ MHz, inverts the interaction “sandwich" by making the central region more weakly interacting than the wings of the atomic cloud as shown by the predicted spatially varying scattering length in (Fig. 4.12d). This demonstrates that the sign of the interactions between the central and the outer regions of the cloud can be inverted. For $\delta = -0.11$ MHz, the interactions in the central region

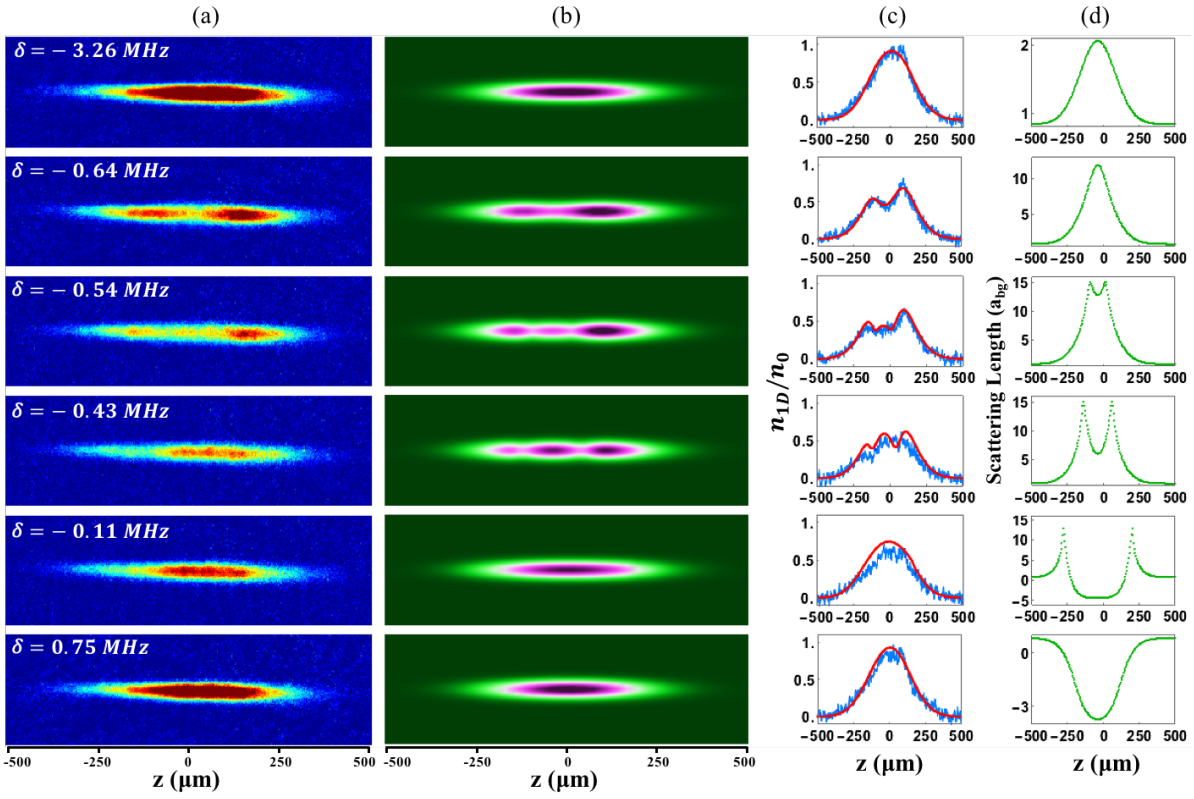

Figure 4.12 Designer spatial interaction patterns in an ultra-cold gas of ^{6}Li atoms versus two-photon detuning δ, by varying ν_2 and holding ν_1 constant. (a) Measured false color 2D absorption images of atoms arriving in state $|2\rangle$ from state $|3\rangle$ in the presence of atoms in state $|1\rangle$; (b) Predicted 2D images using measured parameters in Eq. 4.18; (c) Normalized 1D axial profiles n_{1D}/n_0, where n_0 is the peak density with no atoms in state $|1\rangle$. Measured (blue) and calculated (red) from Eq. 4.18; (d) Momentum averaged two-body scattering length a_{12}^{opt} (Eq. 4.21) used to generate the predicted 2D and 1D spatial profiles in (b) and (c), respectively.

become attractive with $a_{12} \approx -5\, a_{bg}$ and the interactions in the wings become repulsive with $a_{12} \approx 10\, a_{bg}$. As δ is tuned from below the two-photon resonance, $\delta = -3.26$ MHz, to above the two-photon resonance, $\delta = +0.75$ MHz, the interactions in the central region of the cloud change sign from repulsive to attractive. Hence, a tuning range of just 4 MHz imprints widely diverse interaction “designs" on the atomic cloud.

In conclusion, the results shown in this chapter demonstrate optical tunability of scattering interactions in an ultra-cold gas of ^{6}Li atoms near an energy-dependent narrow Feshbach resonance. EIT optical control of interactions achieves the same level of tunability as magnetic control, which has never been demonstrated before. Further, EIT optical control is also shown to achieve designer spatial control of interactions, where spatially dependent interaction profiles were imprinted by small MHz frequency changes in the optical fields. Although spatially varying interactions based on optical techniques have been reported before, previous experiments either suffered from extremely short (10 μs) lifetimes [Yam10] or limited optical tunability, 0.2 abg [Cla15]. Further, all-optical manipulation of spatial interaction profiles has not been previously demonstrated. Of particular significance is the first realization of an interaction “sandwich" with resonantly and weakly interaction regions in an atomic cloud, demonstrating the versatility of the EIT method.

CHAPTER

5

OPTICAL PROBING OF AN ENERGY DEPENDANT NARROW FESHBACH RESONANCE

In a magnetic Feshbach resonance, external magnetic fields are used to tune the total energy of two colliding atoms in an energetically open channel into resonance with a bound dimer state in a closed channel. However, for the case of a narrow Feshbach resonance, where the width of the resonance ΔB is comparable to the relative energy of the incoming atom pair, the interactions are momentum-dependent [Ho12; Haz12] and the resonance can be tuned energetically. This offers tremendous possibilities in realizing novel quantum phases in ultracold gases such as stable transitionally invariant gapless superfluid states, breached-pair superfluidity [For05] and synthetic FFLO (Fulde-Ferrell-Larkin-Ovchinnikov) states [He18].

Further, the effective range r_e is inversely proportional to the width of the resonance ΔB. The narrow Feshbach resonance in ^{6}Li near 543.27 G (width $\Delta B = 0.1G$) is particularly

interesting due the anomalously large effective range $r_e \approx -7 \times 10^4\, a_0$, where a_0 is the Bohr radius. In contrast, for the broad Feshbach resonance in ^{6}Li at 832 G (width $\Delta B = 300G$), the effective range $r_e \approx 1\, a_0$. The large effective range of the narrow Feshbach resonance in ^{6}Li, coupled with resonant interactions, can be exploited to study neutron matter at sub nuclear densities in the regime $k_f\, r_e \gtrsim 1$ (k_f is the Fermi momentum), which is critical for understanding the physics of neutron stars and supernova.

Although energy-dependent narrow Feshbach resonances with momentum dependent interactions offer wide possibilities to explore new domains in atomic gases, there have been only limited number of experimental studies. Further, in all previous studies, external magnetic fields were used to tune the energy of the colliding atom pair (continuum) across the bound molecular state to create narrow Feshbach molecules [Str03], measure two-body interactions [Haz12], and to study three-body recombination loss [Li18]. Optical control of interactions [Fed96; BJ97; Fat00; Eno08; The04; Yam10; Bau09a; Jag14; Cla15] provides a new way of investigating a Feshbach resonance by tuning the closed channel molecular bound state across the open channel continuum, but has been extremely limited in applicability due to atom loss from spontaneous scattering.

In Chapter 4, optical control of interactions near the narrow Feshbach resonance in ^{6}Li was demonstrated using closed-channel electromagnetically induced transparency. In this scheme, two optical fields are used to tune the closed channel molecular bound state near a magnetic Feshbach resonance by changing the frequency of the optical fields [WT12a; WT12b], with suppressed atom loss through destructive quantum interference. The closed-channel EIT method also offers the possibility of creating synthetic FFLO states using momentum-selective control of interactions [He18] and emulating the physics of neutron matter by controlling the effective range, which requires a thorough understanding of optically controlled momentum-dependent interactions near a narrow Feshbach resonance.

In this chapter, I will discuss experiments to investigate momentum-dependent interactions near the narrow Feshbach resonance in ^{6}Li by using the closed-channel EIT method as an optical vernier. The closed-channel EIT methods convert mG changes in magnetic fields into MHz changes in frequency, thereby allowing high precision studies of collisional interactions near a Feshbach resonance. I would like to emphasize that these types of studies cannot be pursued by using single field optical techniques [Bau09a; Cla15] and are only possible because of the closed-channel EIT method, as it compensates a a single field momentum-dependent light shift with a two-field light shift.

As explained in Chapter 4, the molecular bound state is tuned by changing the frequency of one laser. Two-photon atom loss spectra are measured at different magnetic fields both on the atomic side (BCS) above and the molecular side (BEC) below the resonance. An asymmetric spectral shift of the loss spectra is observed only on the BCS side of the resonance, similar to the previously reported asymmetry in the three-body loss and two-body scattering length near the narrow Feshbach resonance. The atom loss spectra exhibit a rich structure, reflecting the presence of momentum-dependent interactions and are in excellent agreement with our continuum-dressed state model (Chapter 2) in both shape and magnitude. However a new shift in the two-field spectra is observed, which cannot be explained by our theoretical model.

I will begin this chapter by presenting the calculation of optically induced atom loss from the two-body loss constant K_2 (derived in Chapter 2). In Section 5.2, measurement of atom loss spectra at different magnetic fields both on the atomic side (BCS) and the molecular side (BEC) of the resonance will be presented. The atom loss spectra are compared to the theoretical prediction from Section 5.1. The asymmetric spectral shift of the loss spectra observed on the atomic side of the resonance will be discussed in Section 5.3.

5.1 Calculation of Optically Induced Atom Loss from K_2

In Chapter 2, I derived the two-body loss rate constant K_2 using the continuum-dressed state model. In this section, I will calculate the optically induced atom loss from the two-body loss rate constant K_2.

Let $n_\uparrow$ and $n_\downarrow$ be the density of spin up and spin down atoms in the two hyperfine levels, respectively. The total loss rate $\dot{N}$ is

$$\dot{N} = \int d^3\vec{r}\,(\dot{n}_\uparrow + \dot{n}_\downarrow) \tag{5.1}$$

The loss rate per unit volume can be expressed as

$$\dot{n}_\uparrow = \dot{n}_\downarrow = -n_\downarrow\, v_{rel}\, \sigma_{inelastic}\, n_\uparrow \tag{5.2}$$

where $n_\downarrow\, v_{rel}\, \sigma_{inelastic}$ is the collision rate. The two-body loss rate constant $K_2(k)$ from

Eq. 2.65 is given by,

$$K_2(k) = v_{rel}\,\sigma_{inelastic}. \tag{5.3}$$

Substituting Eq. 5.2 and Eq. 5.3 in Eq. 5.1, yields

$$\dot{N} = -2\int d^3\vec{r}\,K_2(k)\,n_\uparrow n_\downarrow \tag{5.4}$$

Assuming a classical Boltzmann distribution of relative momentum k between atoms, the relative momentum averaged two-body loss rate constant $\overline{K_2}$ is given by,

$$\overline{K_2} = \int_0^\infty \frac{4\pi k^2 dk}{(k_0\sqrt{\pi})^3}\, e^{-\frac{k^2}{k_0^2}}\, K_2(k) \tag{5.5}$$

Substituting Eq. 5.5 in Eq. 5.4, gives

$$\begin{aligned}\dot{N} &= -2\int d^3\vec{r}\,n_\uparrow n_\downarrow \int_0^\infty \frac{4\pi k^2 dk}{(k_0\sqrt{\pi})^3}\, e^{-\frac{k^2}{k_0^2}}\, K_2(k) \\ &= -\frac{1}{2}\int d^3\vec{r}\,[n(\vec{r})]^2 \int_0^\infty \frac{4\pi k^2 dk}{(k_0\sqrt{\pi})^3}\, e^{-\frac{k^2}{k_0^2}}\, K_2(k)\end{aligned} \tag{5.6}$$

Rewriting Eq. 5.6 in terms of the average density $\bar{n}$ gives,

$$\dot{N} = \frac{N}{2}\,\bar{n}\int_0^\infty \frac{4\pi k^2 dk}{(k_0\sqrt{\pi})^3}\, e^{-\frac{k^2}{k_0^2}}\, K_2(k) \tag{5.7}$$

where the average density $\bar{n}$ is given by

$$\bar{n} \equiv \frac{1}{N}\int d^3\vec{r}\,[n(\vec{r})]^2. \tag{5.8}$$

Assuming

$$\Gamma \equiv \frac{1}{2}\,\frac{\bar{n}}{N}\int_0^\infty \frac{4\pi k^2 dk}{(k_0\sqrt{\pi})^3}\, e^{-\frac{k^2}{k_0^2}}\, K_2(k) \tag{5.9}$$

Substituting Eq. 5.9 in Eq. 5.7 yields,

$$\frac{\dot{N}}{N^2} = -\Gamma$$

Integrating both sides and solving for $N(t)$ gives,

$$\int_{N_0}^{N} \frac{dN}{N^2} = -\Gamma \int_0^t dt$$

$$\frac{N(t)}{N_0} = \frac{1}{1+N_0\Gamma t}, \tag{5.10}$$

where N_0 is the initial total atom number per spin state. Eq. 5.10 is used to predict the atom loss when there is no spatial dependence in the optical parameters. In all experiments reported here, the size of the ν_2 beam is comparable to the axial size of the atom cloud, resulting in a spatially dependent Rabi frequency $\Omega_2(z)$ of the ν_2 beam. Therefore, Eq. 5.10 cannot be used to compare our experimental results and warrants a different method to calculate the atom number, which I present here.

The 1D density of a thermal gas in an optical trap with axial frequency ω_z, temperature T, and atomic mass m is written as

$$n_{1D}(z) = \frac{N_0}{\sqrt{2\pi}} \sqrt{\frac{m\omega_z^2}{k_B T}} \exp\left(-\frac{m\omega_z^2 z^2}{k_B T}\right) \tag{5.11}$$

The modified 1D density in the presence of optical fields after time t is written using Eq. 5.10 as

$$n_{1D}(z,t) = \frac{n_{1D}(z)}{1+\frac{1}{2}N_0 \frac{n_{1D}(z)}{n_{1D}(0)} \sqrt{2}\, \bar{n}_{3D}\, \overline{K}_2(z)\, t}, \tag{5.12}$$

where $\bar{n}_{3D}$ is the 3D density and $\overline{K}_2(z)$ is the momentum averaged z-dependent two-body loss rate constant and is given by

$$\overline{K_2}(z) = \int_0^\infty \frac{4\pi k^2 dk}{(k_0\sqrt{\pi})^3}\, e^{-\frac{k^2}{k_0^2}}\, K_2(k,z) \tag{5.13}$$

The total atom number $N(t)$ is calculated by integrating the 1D density $n_{1D}(z,t)$ in Eq. 5.12

over z,

$$N(t) = \int_{-\infty}^{\infty} n_{1D}(z,t)\,dz \tag{5.14}$$

Eq. 5.14 is used to compare our experimental results presented in the next section.

5.2 Optically Induced Atom Loss near a Narrow Feshbach Resonance

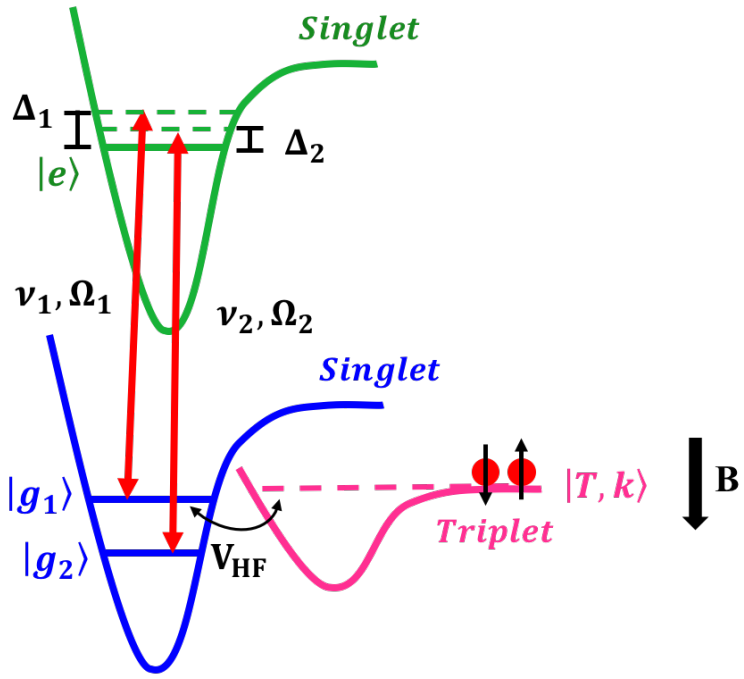

Figure 5.1 Energy level scheme for closed-channel electromagnetically induced transparency (EIT). Optical fields ν_1 (with Rabi frequency Ω_1, detuning Δ_1) and ν_2 (with Rabi frequency Ω_2, detuning Δ_2) couple the ground molecular singlet states $|g_1\rangle$ and $|g_2\rangle$ with the excited singlet state $|e\rangle$ of the closed channel. Atoms reside in the open channel triplet continuum $|T,k\rangle$, which is hyperfine coupled to $|g_1\rangle$ resulting in the narrow Feshbach resonance.

In this section, I will show the experimental measurements of optically induced atom

loss and compare with the continuum-dressed state model derived in the last section.

The basic level scheme for the closed-channel EIT method is shown in Fig. 5.1. Optical fields ν_1 (Rabi frequency Ω_1, detuning Δ_1) and ν_2 (Rabi frequency Ω_2, detuning Δ_2), couple the ground molecular states of the singlet potential, $|g_1\rangle$ and $|g_2\rangle$, to the excited state $|e\rangle$. The state $|g_1\rangle$ can be energetically tuned by varying the optical parameters such as the laser frequencies, ν_1 and ν_2 and Rabi frequencies, Ω_1 and Ω_2. The bound state $|g_1\rangle$ is coupled to the triplet state $|T,k\rangle$ through a second order hyperfine coupling V_{HF}, which causes the narrow Feshbach resonance. Atoms reside in the triplet continuum $|T,k\rangle$ which tunes downward with magnetic field B, proportional to $2\mu_B B$, where μ_B is the Bohr magneton. The initial magnetic field is chosen such that the triplet continuum is tuned near the resonance magnetic field B_{res}, where $B_{res} = 543.27$ G for the narrow Feshbach resonance. Near resonance, the optical detunings Δ_1 and Δ_2 are large compared to the magnetic detunings $\frac{2\mu_B}{\hbar}(B - B_{res})$, so that the two-photon detuning $\delta \simeq \Delta_2 - \Delta_1$. The frequency of ν_2 optical field is then varied to tune state $|g_1\rangle$ close to $|T,k\rangle$.

Fig. 5.2a shows the energy of the ground state $|g_1\rangle$ as a function of δ, by varying ν_2 and holding ν_1 constant, plotted in units of magnetic field $B - B_{res}$. As δ is varied from negative to positive, the ground molecular state $|g_1\rangle$ tunes from below to above its original unshifted position by $\simeq \frac{|\Omega_1|^2}{|\Omega_2|^2}\,\delta$. The horizontal dashed line is the unshifted position of $|g_1\rangle$, when the two-photon resonance condition is satisfied. Fig. 5.2b shows a magnified view of the tuning plot and a linear fit (blue dotted lines), illustrating that very close to the unshifted position, the tuning of $|g_1\rangle$ is linear. For $\Omega_1 = 0.5\,\gamma_e$ and $\Omega_2 = 2.2\,\gamma_e$, the tuning rate is $\simeq 18$ mG/MHz. Hence the two-photon detuning δ acts as an optical vernier to investigate fine momentum-dependent features of the narrow Feshbach resonance.

The experimental procedure is as follows. A 50-50 mixture of the two lowest hyperfine states of ^{6}Li atoms $|1\rangle$ and $|2\rangle$ is confined in a CO_2 laser trap. After evaporatively cooling the atoms at 300 G, the magnetic field is ramped to 528 G. An RF sweep of 30 ms then transfers the atoms from state $|2\rangle$ to $|3\rangle$. The magnetic field is then ramped to the field of interest, where it is allowed to stabilize for 3 s. At the field of interest, the ν_2 beam with Rabi frequency $\Omega_2 = 2.2\,\gamma_e$ is applied. The ν_2 beam creates an additional trapping potential on the atoms and requires a wait time of 30 ms for the atoms to reach equilibrium in the combined CO_2 and ν_2 trapping potential. After the atoms reached equilibrium, an RF π pulse (1.2 ms) transfers the atoms from $|3\rangle$ to $|2\rangle$. The ν_1 beam with Rabi frequency $\Omega_1 = 0.5\,\gamma_e$ and detuning $\Delta_1 = 19$ MHz is then applied for 5 ms. The atoms are imaged after a time of flight of

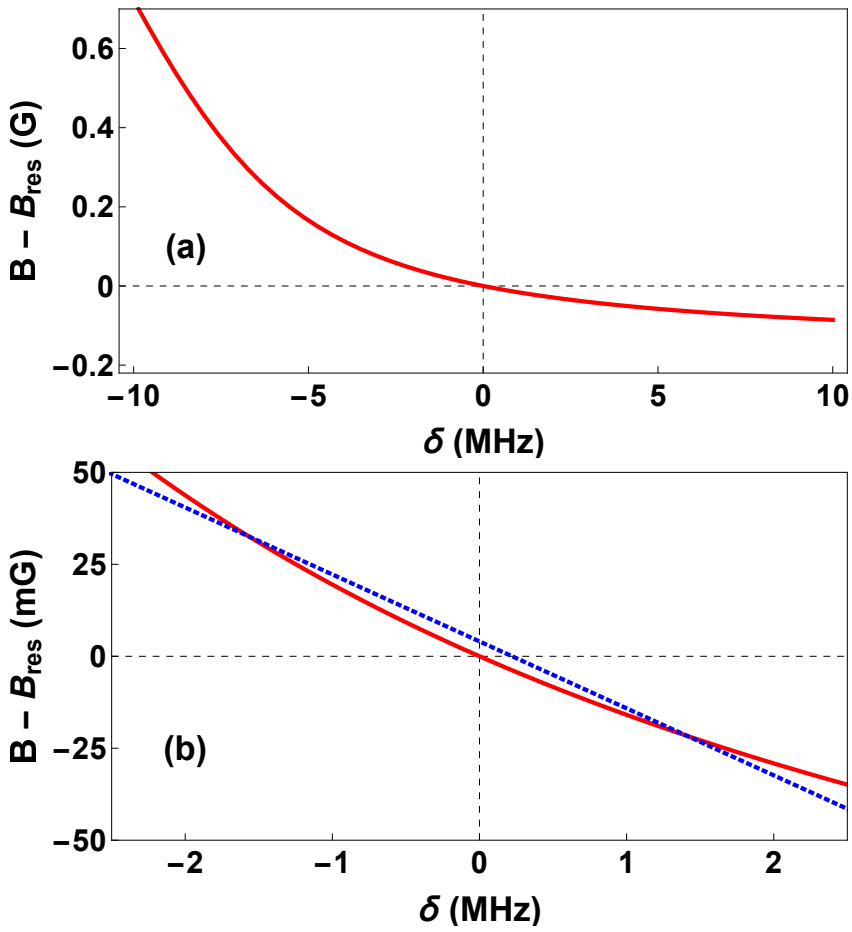

Figure 5.2 (a) Energy of the ground state $|g_1\rangle$ as a function of δ plotted in units of magnetic field $B - B_{res}$, where $B_{res} = 543.27$G for the narrow Feshbach resonance. Horizontal dashed line is the unshifted position of $|g_1\rangle$, when the two-photon resonance condition $\delta = \Delta_2 - \Delta_1 = 0$ is satisfied. (b) Expanded view of the tuning plot and a linear fit (blue dotted lines), illustrating that very close to the unshifted position, the tuning of $|g_1\rangle$ is linear. The energy of $|g_1\rangle$ tunes linearly with δ near the unshifted position, $\simeq 18$ mG/MHz for $\Omega_1 = 0.5\,\gamma_e$ and $\Omega_2 = 2.2\,\gamma_e$.

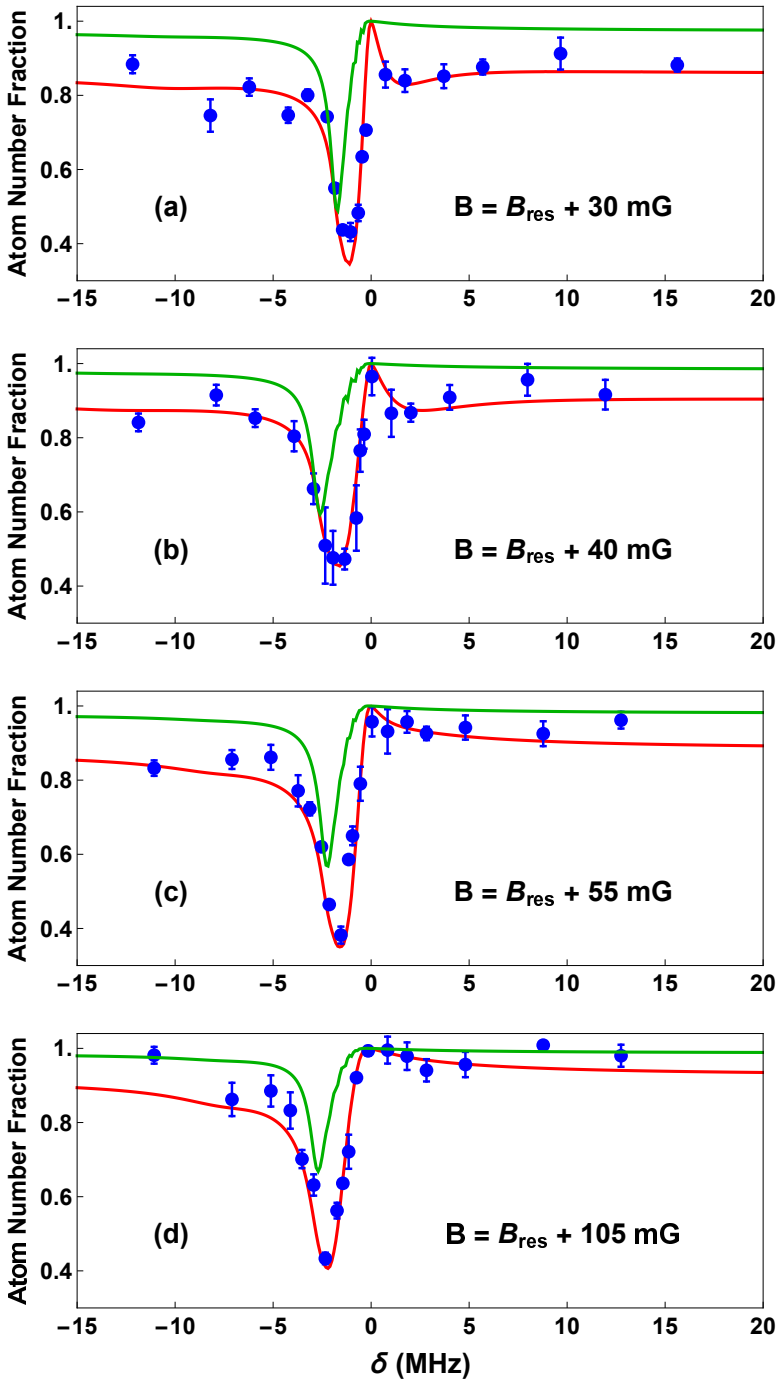

Figure 5.3 Two-photon atom loss spectra for $B > B_{res}$. Atom number fraction (blue dots) as a function of two-photon detuning δ, by varying ν_2 and holding ν_1 constant. Solid curves: Predictions from k-averaged (red) and $k = 0$ (green) theoretical model [Eq. 5.14].The experimental parameters used are given in Table 5.1.

Table 5.1 Experimental parameters used to measure two-photon atom loss spectra in Fig. 5.3 and Fig. 5.4

Experimental Parameter	Symbol	Value
Rabi frequency of ν_1 beam	Ω_1	$0.5 \pm 0.05\ \gamma_e$
Rabi frequency of ν_2 beam	Ω_2	$2.2 \pm 0.2\ \gamma_e$
Detuning of ν_1 beam	Δ_1	19 MHz
Temperature of the atomic cloud	T	$1.5 \pm 0.2\ \mu k$
Axial frequency of the total (CO_2 + ν_2 beam) trap	ω_z	$2\pi \times (56 \pm 0.5)$ Hz
Radial frequency of the CO_2 trap	ω_x	$2\pi \times (777 \pm 9.5)$ Hz
Radial frequency of the CO_2 trap	ω_y	$2\pi \times (960 \pm 4.32)$ Hz

250 μs, from which the remaining atom number is calculated. The experimental parameters used are listed in Table 5.1.

Fig. 5.3 and Fig. 5.4 show the atom loss as a function of two-photon detuning δ (by varying ν_2 frequency and holding ν_1 frequency constant), for different initial magnetic fields $B > B_{res}$ (BCS side) and $B < B_{res}$ (BEC side), respectively. Atom loss occurs as atoms in the triplet state $|T,k\rangle$ are optically coupled to the singlet excited state $|e\rangle$, through the hyperfine coupling between $|g_1\rangle$ and $|T,k\rangle$. As the two-photon detuning δ is varied from negative to positive, by changing ν_2 and holding ν_1 constant, the ground molecular state $|g_1\rangle$ is tuned from below to above its original unshifted position (see Fig. 5.2). When $\delta = 0$, the two-photon resonance condition is satisfied and state $|g_1\rangle$ is tuned to its original unshifted position (horizontal dotted line in Fig. 5.2), where atom loss is suppressed, resulting in minimum loss in the spectra.

The maximum loss in the spectra occurs when state $|g_1\rangle$ is tuned into resonance with the triplet continuum $|T,k\rangle$. When $B > B_{res}$, $|T,k\rangle$ is below the unshifted position of $|g_1\rangle$, hence maximum loss occurs for negative values of two-photon detuning δ. Similarly, when $B < B_{res}$, $|T,k\rangle$ is above the unshifted position of $|g_1\rangle$, hence maximum loss occurs for positive values of two-photon detuning δ. Prior to applying the optical fields, the magnetic field is tuned towards either the BCS side or BEC side of the Feshbach resonance. However, the optical tuning (by changing the ν_2 frequency) is always from the BEC side (left side of maximum loss) to the BCS side (right side of maximum loss) for each chosen B field.

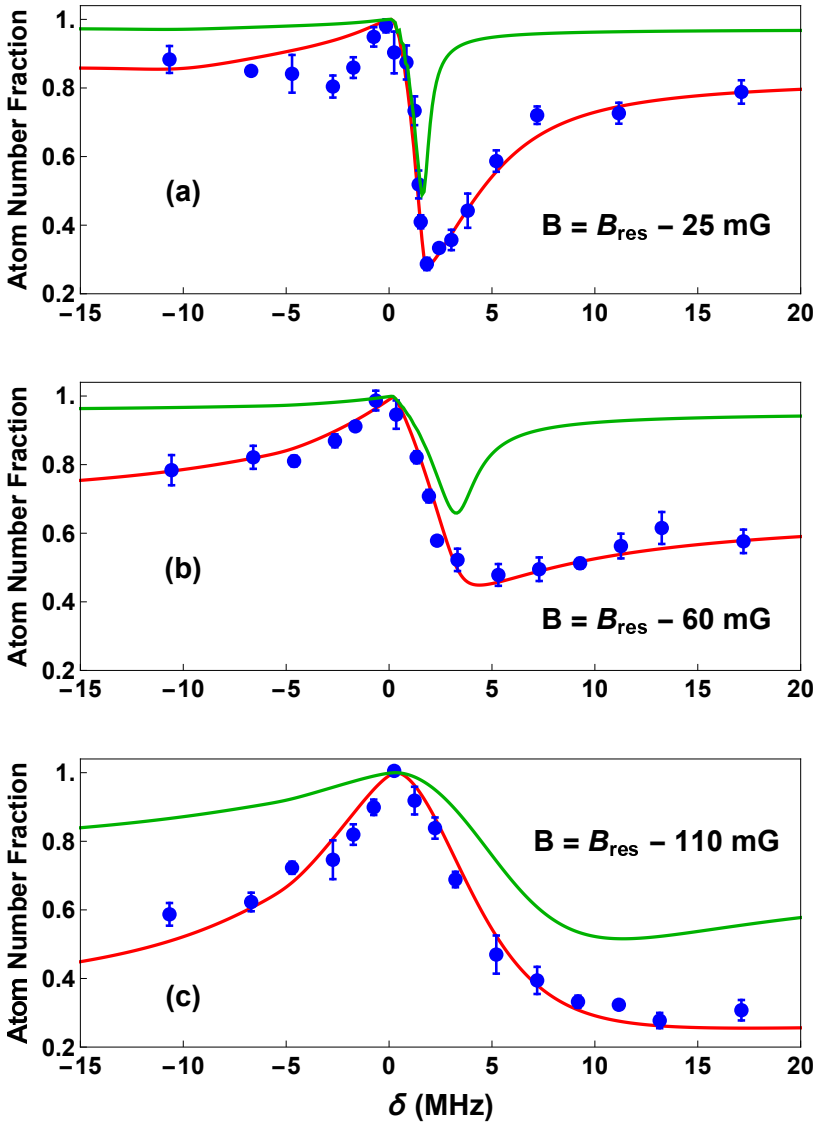

Figure 5.4 Two-photon atom loss spectra for $B < B_{res}$. Atom number fraction (blue dots) as a function of two-photon detuning δ, by varying ν_2 and holding ν_1 constant. Solid curves: Predictions from k-averaged (red) and $k = 0$ (green) theoretical model [Eq. 5.14]. The experimental parameters used are given in Table 5.1.

In order to understand the effects of momentum-dependent interactions on the spectra, the atom loss spectra is compared with the predictions of the continuum-dressed state theoretical model (Eq. 5.14) for both k-averaged (red solid line) and zero momentum $k = 0$ case (green solid line), Fig. 5.3 and Fig. 5.4. The momentum averaged model captures all the fine features of the measured spectra and is in good agreement. For both $B > B_{res}$ (Fig. 5.3) and $B < B_{res}$ (Fig. 5.4), maximum loss in the spectra occurs for two-photon detuning δ greater than the prediction from the zero momentum $k = 0$ model (green curves in Fig. 5.3 and Fig. 5.4). This illustrates that maximum coupling between state $|g_1\rangle$ and $|T, k\rangle$ occurs when state $|g_1\rangle$ is optically tuned to be degenerate with the state $|T, k_0\rangle$ and not with $|T, 0\rangle$, such that all atoms with $k > k_0$ and $k < k_0$ can optimally couple to the molecular bound state (See Fig. 5.5 for a simple illustration).

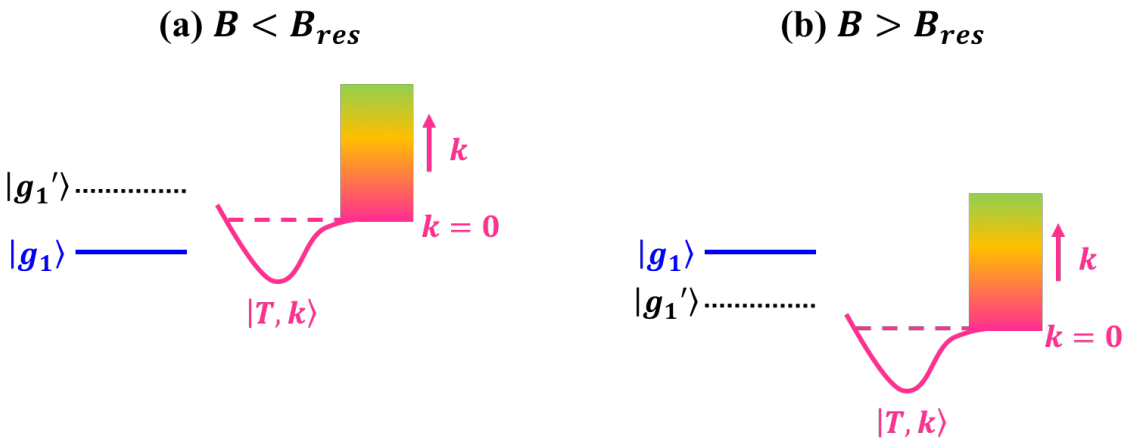

Figure 5.5 A simple illustration of momentum dependence in two-photon atom loss spectra. (a) When $B < B_{res}$, the threshold of the triplet continuum $|T, k\rangle$ is above the unshifted position of $|g_1\rangle$. Hence, higher lying momentum states with $k > 0$ are not degenerate with the unshifted state $|g_1\rangle$. However, the light shifted state $|g_1'\rangle$ can be tuned to be degenerate with $k > 0$ states. (b) When $B > B_{res}$, the $k > 0$ states of the continuum are degenerate with the unshifted state $|g_1\rangle$, for small magnetic detunings $B - B_{res}$.

In the absence of momentum-dependent interactions (broad Feshbach resonances), maximum loss occurs when $|g_1\rangle$ is tuned to be degenerate with the zero momentum state, $|T, 0\rangle$. This phenomenon is observed in previously reported measurements of two-body interactions, where for broad Feshbach resonances, the measured two-body scattering

length agrees with the predicted zero momentum scattering length and diverges near the resonance [RJ03]. However, for the narrow Feshbach resonance, the measured scattering length goes to zero near the resonance, since interactions of opposite sign between atoms of different momentum k states are thermally averaged over a Boltzmann distribution.

When $B > B_{res}$ (BCS), the effect of momentum-dependent interactions is clearly seen on the additional loss peak observed to the right of the minimum loss point (two-photon resonance), in agreement with the k-averaged theoretical model, Fig. 5.3a and Fig. 5.3b. The additional loss peak is due to resonant coupling of the bound state near its unshifted position with higher momentum k states. The spectral shapes are understood by considering the energy of molecular bound state $|g_1\rangle$ as a function of ν_2. From the momentum-dependent continuum-dressed state model [Eq. 2.40], maximum loss occurs when

$$\Delta_1 + \frac{|\Omega_1|^2}{4\left[\frac{2\mu_B}{\hbar}(B-B_{res}) - \frac{\hbar k^2}{m}\right]} + \frac{|\Omega_2|^2}{4\delta} = 0. \tag{5.15}$$

Note that Eq. 5.15 assumes for brevity that the frequencies corresponding to the magnetic detuning $\frac{2\mu_B}{\hbar}(B-B_{res})$ and kinetic energy $\hbar k^2/m$, are small compared to the optical detunings Δ_1 and Δ_2. The second term is a one-photon optical shift arising from the momentum dependence of the triplet continuum. For the experimental conditions, where $\Delta_1 \approx 19$ MHz, $\Omega_1 \approx 6$ MHz, and $|B-B_{res}| < 0.1$, the $|\Omega_1|^2$ term always dominates the first term. Maximum loss therefore occurs when the one-photon optical shift is canceled by the two-photon light shift given by the third term, where $\Omega_2 \simeq 24$ MHz in our experiments. When $B < B_{res}$ (BEC side), the $|\Omega_1|^2$ term in Eq. 5.15 is negative for all k. Hence, the condition for maximum loss given by Eq. 5.15 is satisfied *only* when the two-photon detuning δ is positive, Fig. 5.4.

However, when $B > B_{res}$ (BCS side), the $|\Omega_1|^2$ term in Eq. 5.15 is positive for $k < k_r$ and negative for $k > k_r$, where k_r is the momentum of the triplet continuum state $|T, k_r\rangle$ that is degenerate with $|g_1\rangle$ and satisfies the condition,

$$\frac{2\mu_B}{\hbar}(B-B_{res}) - \frac{\hbar k_r^2}{m} = 0. \tag{5.16}$$

This leads to two loss peaks, a primary maximum loss peak for $\delta < 0$ ($k < k_r$), due to the large atom population at lower k (Maxwell-Boltzmann distribution) and an additional loss peak for $\delta > 0$ ($k > k_r$), which is less populated, most apparent in Fig. 5.3a and Fig. 5.3b. The momentum-dependent model captures the observed loss peak for $\delta > 0$, while the $k = 0$

model is completely flat. As the magnetic detuning $B - B_{res}$ is increased, Eq. 5.16 can no longer be satisfied as the momentum k_r is limited by the Maxwell-Boltzmann distribution for finite temperature T. i.e., $k < k_r$ for all k. Therefore, the additional loss peak for $\delta > 0$ disappears, as seen in Fig. 5.3c and Fig. 5.3d. Fig. 5.5b shows a simple illustration of this effect for $B > B_{res}$. The black dotted line is the light shifted ground state $|g_1'\rangle$ due the AC stark effect.

When $B < B_{res}$ (BEC), Fig. 5.4, the unshifted molecular bound state $|g_1\rangle$ cannot resonantly couple with non-zero k states, i.e., Eq. 5.16 is never satisfied as the magnetic detuning term $B - B_{res}$ is negative and k is always positive (Fig. 5.5a). Hence, there is no additional loss peak near the two-photon resonance. However, the molecular bound state can be optically tuned to be resonant with non-zero k states. This can be observed to the right of the maximum loss peak in the spectra, where the atom loss occurs for the larger range of ν_2 frequencies, due to the coupling of the bound state $|g_1\rangle$ with higher momentum non-zero k states.

5.3 Observation of Spectral Shift in Two-photon Atom Loss Spectra

Optical coupling of a continuum to the excited bound state results in an anomalous redshift of the excited state. When the open channel continuum $|T, k\rangle$ is optically coupled to the closed channel excited state $|e\rangle$ through a Feshbach resonance, the spectral shift depends on the amount of mixing between the ground molecular state $|g_1\rangle$ and the open channel continuum $|T, k\rangle$.

For experiments near the narrow Feshbach resonance reported in this chapter, when the atom loss spectra are compared with the predictions of the theoretical model (Eq. 5.14), a frequency shift of the two-photon atoms loss spectrum is observed, Fig. 5.6a. Hence an overall frequency shift has to be introduced in the measured data to make it agree with the theoretical model,Fig. 5.6b. Fig. 5.7 shows the magnetic field dependent frequency shift of the atoms loss spectra for both $B < B_{res}$ and $B > B_{res}$ regimes. The observed spectral shifts are magnetic field dependent and asymmetric in structure, with large variation of the shifts for $B > B_{res}$ (BCS) compared to $B < B_{res}$ (BEC), where the shift is constant as illustrated in Fig. 5.7.

The magnetic field independent shift may arise in part from a systematic error or from

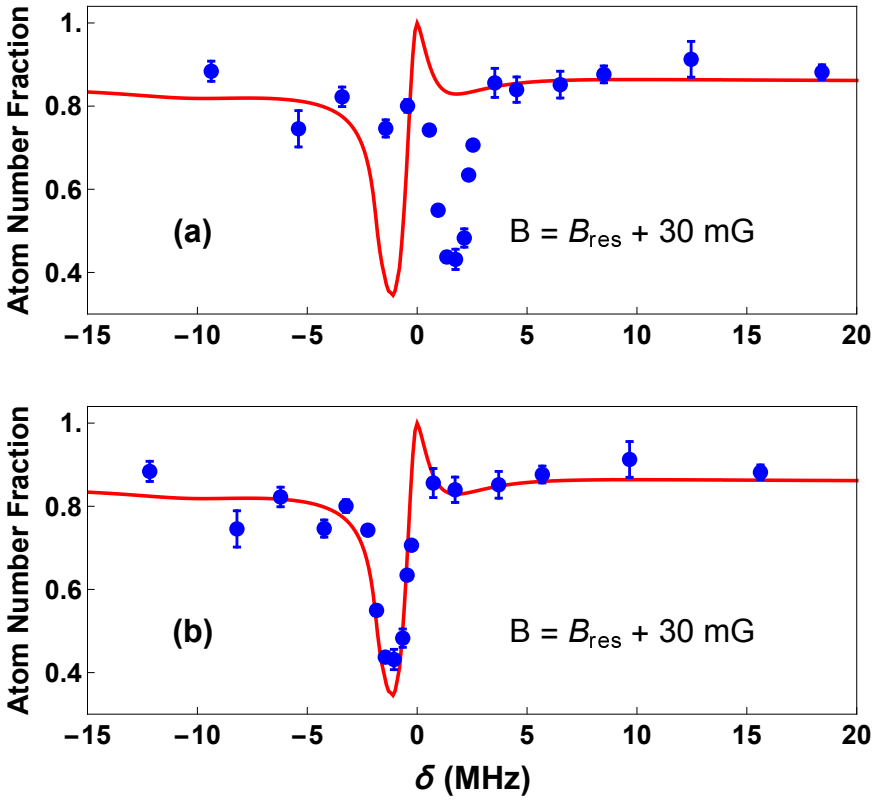

Figure 5.6 Atom number fraction (blue dots) as a function of two-photon detuning δ, by varying ν_2 and holding ν_1 constant. (a) Spectral shift in the measured (blue dots) two-photon atom loss spectra, resulting in a disagreement with the predictions from Eq. 5.14 (red solid line) (b) Atom loss spectra after shifting the measured data (blue dots) to agree with the Eq. 5.14 (red solid line). The shift introduced in the measured spectra to make it agree with the predictions is plotted in Fig. 5.7 for various magnetic fields. The experimental parameters used are given in Table 5.1.

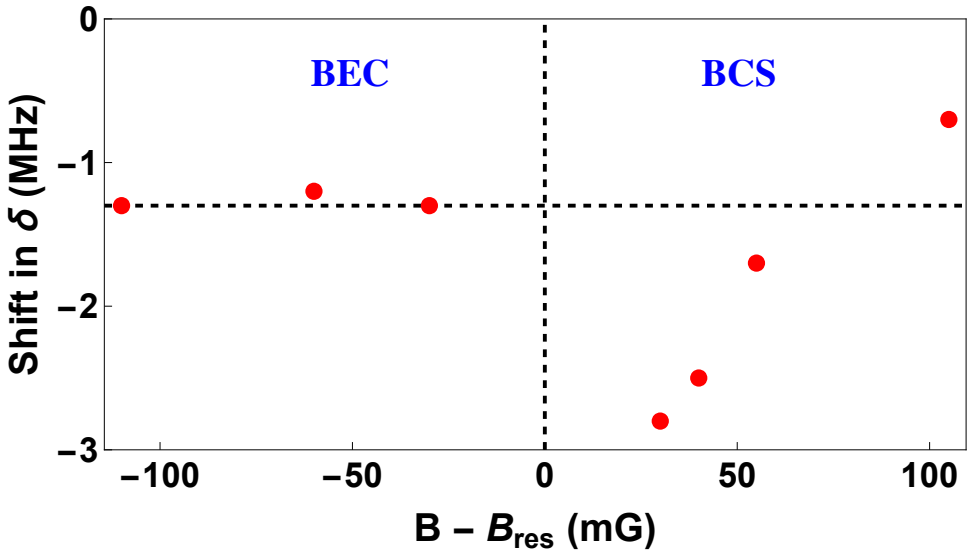

Figure 5.7 Spectral shift of two-photon loss spectra (shown in Fig. 5.3 and Fig. 5.4) as a function of magnetic field B near the narrow Feshbach resonance at $B_{res} = 543.27$ G in ^{6}Li. Horizontal dashed line - background anomalous shift of 1.3 MHz due to the coupling of continuum to an bound state. Vertical dashed line; $B = B_{res}$.

an anomalous background redshift of the excited state [BJ99; Fed96], which would affect our Δ_1 frequency calibration and hence the absolute value of the two-photon detuning δ. Such an anomalous shift was observed in the photoassociation experiments in ^{7}Li [Pro03; Ger01], resulting in an overall spectral shift of the single-field atom loss spectra. An additional intensity-dependent asymmetric shift also was observed near a Feshbach resonance in ^{7}Li [Jun08; Mac08]. As noted above, the one-photon optical shift term $\propto |\Omega_1|^2$ in Eq. 5.15 arises from the Feshbach resonance induced optical coupling of the triplet continuum to the excited state, and appears to explain the asymmetric shift observed in Ref. [Jun08], Fig. 5.8. However, the frequency shifts observed in this experiment for the two-photon detuning cannot be explained with our current theoretical model.

In summary, momentum-dependent interactions near a narrow Feshbach resonance have been studied by optically tuning the closed channel molecular bound state near the open channel continuum threshold using the two-field method as an optical vernier. The momentum dependence of the two-body interactions strongly modifies the measured two-photon atom-loss spectra, providing new insights on the dynamics of Feshbach coupling in an energy-dependent Feshbach resonance. Further, the momentum-dependent continuum-dressed state model is in good agreement with the measured spectra in shape

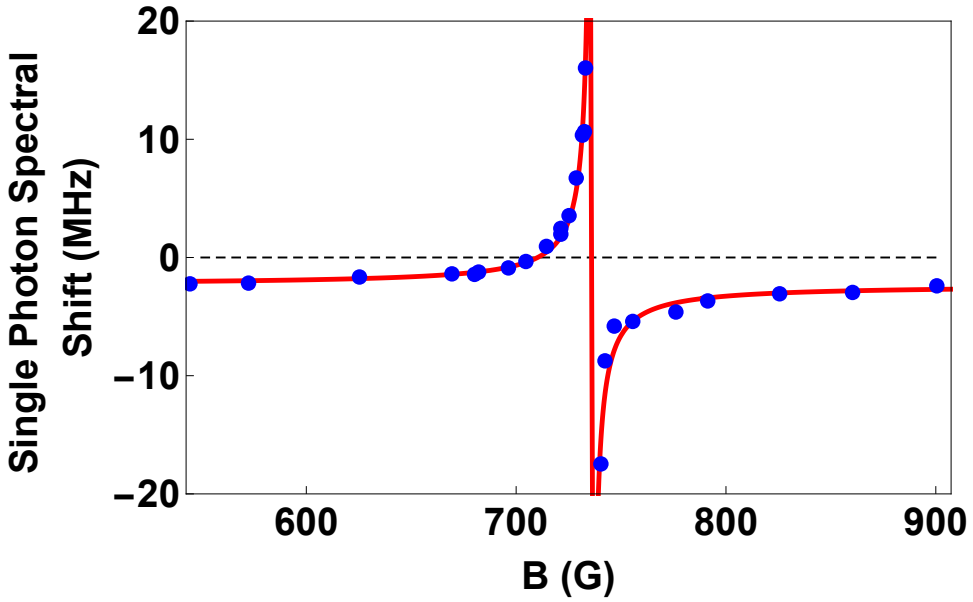

Figure 5.8 Spectral shift of single-photon loss spectra as a function of magnetic field B near the broad Feshbach resonance in ^{7}Li from Ref. [Jun08]. Solid red curve is the fit of the data [Jun08] with the $|\Omega_1|^2$ term in Eq. 5.15 for T = 1 μk and $\Omega_1 = 2.2\,\gamma_e$.

and magnitude. The observed asymmetric spectral shifts are the atom loss spectra near the narrow Feshbach resonance is in disagreement with previously measured symmetric spectral shifts near the broad Feshbach resonance in ^{7}Li [Jun08]. Although our theoretical model might account for the single photon spectral shifts observed near the broad Feshbach resonance in [Jun08], it fails to address the two-photon spectral shifts observed near the narrow resonance. A thorough understanding of this issue would require further theoretical and experimental investigation and can potentially offer new insights in two-body scattering near an energy-dependent resonance.

CHAPTER

6

CONCLUSION

In this chapter, I will briefly summarize the results presented in this thesis and further provide an overview of future experiments that can be pursued using the closed-channel EIT method.

This thesis presents the first work on using the two-field optical method, also referred to as closed-channel EIT, to control and measure two-body scattering interactions in an ultracold gas. All the experiments were done near the narrow Feshbach resonance in ^{6}Li. The two-body scattering length was controlled by changing the frequency of one laser by just a few MHz, and the optical tunability was demonstrated by measuring mean-field induced spectral shifts in radio-frequency spectra. The optical tunability of scattering length was compared with magnetic tuning to illustrate that the two-field method achieves the same level of tuning as magnetic tuning. This is a tremendous improvement over other optical techniques, where the optical tuning is limited due to spontaneous scattering and is only a small fraction of magnetic tuning. The two-field method overcomes this long-standing issue by exploiting quantum interference to suppress spontaneous scattering and achieved a tunability of 12 a_{bg}, where a_{bg} is the background scattering length. The tunability was

only limited by the nature of the narrow Feshbach resonance, which was energy-dependent (limited by temperature) and does not reflect a fundamental limitation of the two-field optical method. Future experiments using the two-field optical method can be pursued near medium width Feshbach resonances such as ^{40}K or ^{87}Rb, and the tunability can be significantly increased, allowing for the realization of novel quantum phases and studies of exotic quantum dynamics.

This thesis further demonstrated spatial “designer" control of interactions in an ultracold gas by exploiting the unprecedented optical tunability achieved using the two-field method. Although spatially varying interactions in an ultracold gas were demonstrated before, either the experiments suffered from a limited lifetime of a few microseconds or magnetic fields were used to change the spatial interaction profile of the atoms. The experiments reported here are the first all-optical manipulation of spatial interaction profiles in an ultracold gas. Spatial “designer" interactions was demonstrated by creating an interaction “sandwich" of resonantly and weakly interacting regions. A few MHz change in the frequency of the laser beams destroys the interaction “sandwich" by creating uniformly attractive or repulsive interactions. This has far-reaching applications in the field of condensed matter physics by creating “collisionally inhomogeneous" systems. Future experiments can be done by constructing an interaction lattice with one of the optical beams, where alternative regions of strong and weak interactions, or attractive and repulsive interactions can be achieved. This method can also be used to create a “supersolid", an idea proposed by Rempe [Bau09a], where the interactions of atoms on each lattice site can be engineered with high precision.

Our two-field method can also be used to create momentum selective control of interactions. Recently, theorists from Swinburne University proposed that the two-field method can be used to create synthetic Fulde-Ferrel superfluids, by using two-counter propagating optical beams that interact differently with different velocity class of atoms due to two-photon Doppler shift and therefore create momentum-dependent interactions [He18]. Momentum selective interactions can also be used to create other exotic quantum phases such as breached pair superfluidity. As a first step, I used the two-field optical method to study and investigate momentum-dependent interactions near the energy-dependent narrow Feshbach resonance. Comparison of the measured data with our theory offered new insights on the fundamental dynamics of the momentum-dependent two-body interactions. I also observed asymmetrical spectral shifts in the data that cannot be explained

by our existing theoretical model. Future experiments can be pursued to understand the spectral shifts arising from momentum dependence, not only near the narrow Feshbach resonance but also near the broad Feshbach resonance, which can offer additional insights on two-body scattering.

Controlling the effective range in an ultracold gas has garnered significant interest in both the atomic and nuclear physics community, as it provides a way to emulate the physics of neutron matter [ASP05]. Our two-field method is predicted to manipulate the effective range around the minimum loss region, providing a distinct advantage over other single-field methods, which induces huge atom loss when employed to manipulate the effective range. Future experiments can be pursued to control the effective range of either the narrow Feshbach resonance, which has a large effective range, or the broad Feshbach resonance, which has a small effective range, thereby taking us a step closer to improved models of neutron matter.

Finally, the two-field optical method can provide fast temporal control of interactions, which can be either used to modulate the scattering length or change it abruptly. For example, the interactions can be abruptly switched off or on by changing the frequency of the laser, and interesting quantum dynamics such as collective modes can be observed. This can also be used to study non-equilibrium thermodynamics in ultracold gases, which is a standalone field that has not been sufficiently explored. Using the two-field optical method, interactions can be modulated by modulating the frequency of the laser beams to investigate exotic phenomenon such as “Bosenova", a fireworks of atoms exploding from an ultracold atomic cloud [Cla17], providing insights on the dynamics of core collapse in a supernova.

BIBLIOGRAPHY

[ASP05] A. Schwenk, A. & Pethick, C. J. "Resonant Fermi Gases with a Large Effective Range". *Phys. Rev. Lett.* **95** (2005), p. 160401.

[Bal08] Balbinot, R. et al. "Nonlocal density correlations as a signature of Hawking radiation from acoustic black holes". *Phys. Rev. A* **78** (2 2008), p. 021603.

[Bar05] Bartenstein, M. et al. "Precise determination of ^{6}Li cold collision parameters by radio-frequency spectroscopy on weakly bound molecules". *Phys. Rev. Lett.* **94** (2005), p. 103201.

[Bau09a] Bauer, D. M. et al. "Control of a magnetic Feshbach resonance with laser light". *Nat. Phys.* **5** (2009), p. 339.

[Bau09b] Bauer, D. M. et al. "Combination of a magnetic Feshbach resonance and an optical bound-to-bound transition". *Phys. Rev. A* **79** (6 2009), p. 062713.

[Blo08] Bloch, I. et al. "Many-body physics with ultracold gases". *Rev. Mod. Phys.* **80** (2008), p. 885.

[BJ97] Bohn, J. & Julienne, P. "Prospects for influencing scattering lengths with far-off-resonant light". *Phys. Rev. A* **56** (1997), p. 1486.

[BJ99] Bohn, J. L. & Julienne, P. S. "Semianalytic theory of laser-assisted resonant cold collisions". *Phys. Rev. A* **60** (1 1999), pp. 414–425.

[Cao11] Cao, C. et al. "Universal quantum viscosity in a unitary Fermi gas". *Science* **331** (2011), p. 58.

[Chi10] Chin, C. et al. "Feshbach Resonances in Ultracold Gases". *Rev. Mod. Phys* **82** (2010), p. 1225.

[Cla15] Clark, L. W. et al. "Quantum Dynamics with Spatiotemporal Control of Interactions in a Stable Bose-Einstein Condensate". *Phys. Rev. Lett.* **115** (2015), p. 155301.

[Cla17] Clark, L. W. et al. "Collective emission of matter-wave jets from driven Bose-Einstein condensates". *Nature* **551** (2017), p. 356.

[Den08] Deng, X.-L. et al. "Quantum phases of interacting phonons in ion traps". *Phys. Rev. A* **77** (3 2008), p. 033403.

[Ell14] Elliott, E. “Quantum Transport and Scale Invariance in Expanding Fermi Gases”. PhD thesis. Duke University, 2014.

[Eno08] Enomoto, K. et al. “Optical Feshbach resonance using the intercombination transition”. *Phys. Rev. Lett.* **101** (2008), p. 203201.

[Fat00] Fatemi, F. et al. “Observation of optically induced Feshbach resonances in collisions of cold atoms”. *Phys. Rev. Lett.* **85** (2000), p. 4462.

[Fed96] Fedichev, P. O. et al. “Influence of nearly resonant light on the scattering length in low-temperature atomic gases”. *Phys. Rev. Lett.* **77** (1996), p. 2913.

[Fle05] Fleischhauer, M. et al. “Electromagnetically induced transparency: Optics in coherent media”. *Rev. Mod. Phys.* **77** (2 2005), pp. 633–673.

[For05] Forbes, M. M. et al. “Stability Criteria for Breached-Pair Superfluidity”. *Phys. Rev. Lett.* **94** (1 2005), p. 017001.

[Fu13] Fu, Z. et al. “Optical control of a magnetic Feshbach resonance in an ultracold Fermi gas”. *Phys. Rev. A* **88** (4 2013), p. 041601.

[Geh03] Gehm, M. “Preparation of an Optically-Trapped Degenerate Fermi Gas of 6Li: Finding the Route to Degeneracy”. PhD thesis. Duke University, 2003.

[Ger01] Gerton, J. M. et al. “Photoassociative frequency shift in a quantum degenerate gas”. *Phys. Rev. A* **64** (5 2001), p. 053410.

[Har97] Harris, S. E. “Electromagnetically Induced Transparency”. *Physics Today* **50** (1997), p. 36.

[Hau99] Hau, L. V. et al. “Light speed reduction to 17 metres per second in an ultracold atomic gas”. *Nature* **397** (1999), p. 594.

[Haz12] Hazlett, E. L. et al. “Realization of a Resonant Fermi Gas with a Large Effective Range”. *Phys. Rev. Lett.* **108** (2012), p. 045304.

[He18] He, L. et al. “Realizing Fulde-Ferrell Superfluids via a Dark-State Control of Feshbach Resonances”. *Phys. Rev. Lett.* **120** (4 2018), p. 045302.

[Ho12] Ho, T.-L. et al. “Alternative Route to Strong Interaction: Narrow Feshbach Resonance”. *Phys. Rev. Lett.* **108** (2012), p. 250401.

[Hu14] Hu, M.-G. et al. “Avalanche-mechanism loss at an atom-molecule Efimov resonance”. *Phys. Rev. A* **90** (1 2014), p. 013619.

[Jag14] Jag, M. et al. “Observation of a Strong Atom-Dimer Attraction in a Mass-Imbalanced Fermi-Fermi Mixture”. *Phys. Rev. Lett.* **112** (7 2014), p. 075302.

[Jag16a] Jagannathan, A. et al. “Optical Control of Magnetic Feshbach Resonances by Closed-Channel Electromagnetically Induced Transparency”. *Phys. Rev. Lett.* **116** (7 2016), p. 075301.

[Jag16b] Jagannathan, A. “Optical Control of Magnetic Feshbach Resonances by Closed-Channel Electromagnetically Induced Transparency”. PhD thesis. Duke University, 2016.

[Joc03] Jochim, S. et al. “Bose-Einstein Condensation of Molecules”. *Science* **302** (2003), p. 2101.

[Jun08] Junker, M. et al. “Photoassociation of a Bose-Einstein Condensate near a Feshbach Resonance”. *Phys. Rev. Lett.* **101** (6 2008), p. 060406.

[KZ08] Ketterle, W. & Zwierlein, M. W. “Making, probing and understanding ultracold Fermi gases”. Ed. by Inguscio, M. et al. Ultracold Fermi Gases, Proceedings of the International School of Physics Enrico Fermi, Course CLXIV, Varenna. IOS Press, Amsterdam, 2008.

[Kin04] Kinast, J. et al. “Evidence for Superfluidity in a Resonantly Interacting Fermi Gas”. *Phys. Rev. Lett.* **92** (2004), p. 150402.

[Kin05] Kinast, J. et al. “Heat capacity of a strongly interacting Fermi gas”. *Science* **307** (2005), p. 1296.

[Kin06] Kinast, J. M. “Thermodynamics and Superfluidity of a Strongly Interacting Fermi gas”. PhD thesis. Duke University, 2006.

[Kra06] Kraemer, T. et al. “Evidence for Efimov quantum states in an ultracold gas of caesium atoms”. *Nature* **440** (2006), pp. 315 –318.

[Li18] Li, J. et al. “Three-Body Recombination near a Narrow Feshbach Resonance in ^{6}Li”. *Phys. Rev. Lett.* **120** (19 2018), p. 193402.

[Mac08] Mackie, M. et al. “Cross-Molecular Coupling in Combined Photoassociation and Feshbach Resonances”. *Phys. Rev. Lett.* **101** (4 2008), p. 040401.

[O’H02] O’Hara, K. M. et al. “Observation of a Strongly Interacting Degenerate Fermi Gas of Atoms”. *Science* **298** (2002), p. 2179.

[O'H00] O'Hara, K. "Optical Trapping and Evaporative Cooling of Fermionic Atoms". PhD thesis. Duke University, 2000.

[Pro03] Prodan, I. D. et al. "Intensity Dependence of Photoassociation in a Quantum Degenerate Atomic Gas". *Phys. Rev. Lett.* **91** (8 2003), p. 080402.

[RJ03] Regal, C. A. & Jin, D. S. "Measurement of Positive and Negative Scattering Lengths in a Fermi Gas of Atoms". *Phys. Rev. Lett.* **90** (23 2003), p. 230404.

[Reg03] Regal, C. A. et al. "Creation of ultracold molecules from a Fermi gas of atoms". *Nature* **424** (2003), p. 47.

[Rob95] Robin Côté. "Ultra-Cold Collisions of Identical Atoms". PhD thesis. M.I.T., 1995, p. 418.

[RV05] Rodas-Verde, M. I. et al. "Controllable Soliton Emission from a Bose-Einstein Condensate". *Phys. Rev. Lett.* **95** (15 2005), p. 153903.

[Sal08] Salerno, M. et al. "Long-Living Bloch Oscillations of Matter Waves in Periodic Potentials". *Phys. Rev. Lett.* **101** (3 2008), p. 030405.

[Sch07] Schunck, C. H. et al. "Superfluid Expansion of a Rotating Fermi Gas". *Phys. Rev. Lett.* **98** (2007), p. 050404.

[Sch99] SchÃijnemann, U. et al. "Simple scheme for tunable frequency offset locking of two lasers". *Review of Scientific Instruments* **70**.1 (1999), pp. 242–243.

[Sho90] Shore, B. W. *The Theory of Coherent Atomic Excitation*. Wiley-VCH, 1990.

[Ste08] Stewart, J. T. et al. "Using photoemission spectroscopy to probe a strongly interacting Fermi gas". *Nature* **454** (2008), pp. 744–747.

[Str03] Strecker, K. E. et al. "Conversion of an Atomic Fermi Gas to a Long-Lived Molecular Bose Gas". *Phys. Rev. Lett.* **91** (8 2003), p. 080406.

[Tha05] Thalhammer, G. et al. "Inducing an optical Feshbach resonance via stimulated Raman coupling". *Phys. Rev. A* **71** (2005), p. 033403.

[The04] Theis, M. et al. "Tuning the scattering length with an optically induced Feshbach Resonance". *Phys. Rev. Lett.* **93** (2004), p. 123001.

[Tho05] Thompson, S. T. et al. "Ultracold Molecule Production via a Resonant Oscillating Magnetic Field". *Phys. Rev. Lett.* **95** (19 2005), p. 190404.

[Wu12] Wu, C.-H. et al. “Ultracold Fermionic Feshbach Molecules of ^{23}Na^{40}**K**”. *Phys. Rev. Lett.* **109** (8 2012), p. 085301.

[WT12a] Wu, H. & Thomas, J. E. “Optical Control of Feshbach Resonances in Fermi Gases Using Molecular Dark States”. *Phys. Rev. Lett.* **108** (1 2012), p. 010401.

[WT12b] Wu, H. & Thomas, J. E. “Optical control of the scattering length and effective range for magnetically tunable Feshbach resonances in ultracold gases”. *Phys. Rev. A* **86** (6 2012), p. 063625.

[Xu03] Xu, K. et al. “Formation of Quantum-Degenerate Sodium Molecules”. *Phys. Rev. Lett.* **91** (21 2003), p. 210402.

[Yam10] Yamazaki, R. et al. “Submicron spatial modulation of an interatomic interaction in a Bose-Einstein condensate”. *Phys. Rev. Lett.* **105** (2010), p. 050405.

[Zha13] Zhang, Y. “Radio Frequency Spectroscopy Of a Quasi-Two-Dimensional Fermi Gas”. PhD thesis. Duke University, 2013.

[ZÏ3] Zürn, G. et al. “Precise Characterization of ^{6}Li Feshbach Resonances Using Trap-Sideband-Resolved RF Spectroscopy of Weakly Bound Molecules”. *Phys. Rev. Lett.* **110** (13 2013), p. 135301.

[Zwi06] Zwierlein, M. W. et al. “Fermionic superfluidity with imbalanced spin populations”. *Science* **311** (2006), p. 492.

[Zwi05] Zwierlein, M. et al. “Vortices and Superfluidity in a Strongly Interacting Fermi Gas”. *Nature* **435** (2005), p. 1047.